Numerical study of gas turbine nozzle guide vane external heat transfer and showerhead film cooling effectiveness by means of hybrid RANS-LES CFD modelling

by

Edgars Daugulis

Student number: 4662350
Institution: Delft University of Technology
Place: Siemens Energy AB, Finspång
Project Duration: September, 2021 - June, 2022

TU Delft

Acknowledgements

I would like to express my gratitude to people who supported the thesis work. Starting with Mats Annerfeldt for providing me with the opportunity to perform this study at Siemens Energy and for support during the process. To Andreas Hägg for giving continuous guidance and sharing his vast knowledge and experience. To Daniel Enico for helping on a regular basis on different practical aspects and for promoting discussion. I am grateful for the support and different ideas provided by all my colleagues at Siemens Energy. Finally, an appreciation to my supervisor Dr. Arvind Gangoli Rao for providing important guidance during the thesis work.

Edgars Daugulis
Delft, June 2022

Abstract

An accurate estimation of gas turbine nozzle guide vane metal temperature locally on its surface is crucial for predicting vane lifetime. The stagnation region at the vane leading edge is, typically, exposed to the highest thermal load, thus, the showerhead configuration of film cooling is often applied on the leading edge. Widely used lean-burn combustors implement swirlers, leading to a complex flow field over the nozzle guide vane as the swirling profile is often preserved at the inlet of the guide vane. The nozzle guide vane external heat transfer coefficient in the industry is often computed either with boundary layer codes or RANS methods. However, higher accuracy hybrid RANS-LES models are of interest since such models are becoming more and more available due to improved capabilities to facilitate the increase of computational resource demands. This study aims at introducing hybrid RANS-LES modelling to investigate swirling inflow effects on showerhead film cooling performance.

The implemented methodology and various turbulence models are first validated by replicating an experimental case of a linear cascade of blades. The uncooled blade external heat transfer coefficient distribution is compared to the experimental data for cases with turbulence intensities of Tu =1% and Tu =8%. The SST $k-\omega$ and lag elliptic blending $k-\varepsilon$ turbulence models successfully replicated the HTC distribution but the $\gamma - Re_\theta$ transition model was required to capture transition on the suction side for cases with Tu =1%. The showerhead film cooling effectiveness is investigated with both RANS and hybrid RANS-LES models for a configuration of three rows of staggered cooling holes and blowing ratios of 1.4 and 1.9. Uniform inflow and two profiles of swirling inflow are analysed, with the strongest swirl being coupled with a radial temperature profile. Results indicate that the RANS-LES hybrid model is promising in capturing the unsteadiness of the horseshoe vortex. Mixing between mainstream and coolant jets, and the inherent unsteadiness of the mixing shear layers can only be captured with a scale resolving simulation. The swirling inflow lead to an altered stagnation line and imposed a radial pressure distribution close to the leading edge, which interfered with the coolant distribution on the leading edge. The coolant jet contact with the vane surface area is found to be the most important parameter affecting the cooling effectiveness since a coolant lift-off led to a significant reduction in cooling effectiveness. A lift-off was often observed in areas where the swirling velocity component misaligned to the mainstream flow direction. A positive contribution to cooling effectiveness was recorded in regions where the swirl component aligned to the mainstream flow direction. The increase in cooling effectiveness was observed due to locally increased momentum of the main flow that aids coolant staying attached to the surface. The benefits of hybrid RANS-LES modelling are established, and the results signify the importance of accounting for an unsteady stagnation line during the design of the showerhead film cooling.

Contents

Nomenclature

Abbreviations

Abbreviation	Definition
ALF	Anisotropic Linear Forcing
BR	Blowing Ratio
CAD	Computer-Aided Design
CFD	Computational Fluid Dynamics
CFL	Courant-Friedrich-Lewy
CHT	Conjugate Heat Transfer
DDES	Delayed Detached-Eddy Simulation
DES	Detached-Eddy Simulation
DNS	Direct Numerical Simulation
EB	Elliptic Blending
EVM	Eddy Viscosity Models
FACTOR	Full Aero-thermal Combustor-Turbine interac-tiOn Research
HS	Horseshoe [vortex]
HTC	Heat Transfer Coefficient
LE	Leading Edge
LES	Large Eddy Simulation
LKE	Laminar Kinetic Energy
NGV	Nozzle Guide Vane
NOx	Nitrogen Oxides
PANS	Partially Averaged Navier-Stokes
RANS	Reynolds Averaged Navier-Stokes
RKE	Realizable $k-\varepsilon$ [turbulence model]
RNG	Re-Normalisation Group
RSM	Reynolds Stress Models
SBES	Stress-Blended Eddy Simulation
SRH	Scale Resolving Hybrid
SST	Shear Stress Transport [$k-\omega$ turbulence model]
TE	Trailing Edge
T-S	Tollmien-Schlichting
URANS	Unsteady Reynolds Averaged Navier-Stokes

Symbols

Symbol	Definition	Unit
A	Area	$[m^2]$
c	Chord length	$[m]$
c_p	Specific heat at constant pressure	$[Jkg^{-1}K^{-1}]$
C_f	Skin friction coefficient	$[-]$
D	Diameter of cooling holes	$[m]$
f	Elliptic relaxation parameter	$[-]$
h	Specific enthalpy	$[Jkg^{-1}]$
HTC	Heat Transfer Coefficient	$[Wm^{-2}K^{-1}]$

Symbol	Definition	Unit
k	Turbulence kinetic energy	$[J]$
m	Mass	$[kg]$
Ma	Mach number	$[-]$
P	Pressure	$[Pa]$
Pr	Prandtl number	$[-]$
Q	Heat	$[J]$
q	Heat flux	$[Wm^{-2}]$
r_c	Recovery factor	$[-]$
Re	Reynolds number	$[-]$
Re_t	Turbulent Reynolds number	$[-]$
Re_v	Vorticity Reynolds number	$[-]$
Re_θ	Momentum thickness Reynolds number	$[-]$
$Re_{\theta,c}$	Critical momentum thickness Reynolds number	$[-]$
s	Streamwise curvilinear distance along airfoil surface	$[m]$
S	Rate-of-strain tensor	$[-]$
S_n	Swirl intensity	$[-]$
St	Stanton number	$[-]$
T	Temperature	$[K]$
t	Time	$[s]$
Tu	Turbulence intensity	$[-]$
U	Velocity	$[ms^{-1}]$
$\bar{v^2}$	Velocity fluctuation normal to wall	$[m^2s^{-2}]$
W	Work	$[J]$
x	Distance along streamline	$[m]$
y	Wall distance	$[m]$
y^+	Non-dimensional wall distance	$[-]$
α	Elliptic blending factor	$[-]$
β	Coolant injection angle	$[-]$
γ	Intermittency	$[-]$
δ	Boundary layer thickness	$[m]$
δ_{ij}	Kronecker delta	$[-]$
ε	Turbulent dissipation rate	$[m^2s^{-3}]$
η	Adiabatic cooling effectiveness	$[-]$
η_{row}	Aerodynamic row efficiency	$[-]$
θ	Momentum thickness	$[m]$
κ	Ratio of specific heats	$[-]$
Λ_t	Turbulent length scale	$[m]$
Λ_k	Energy scale	$[m]$
λ	Thermal conductivity	$[Wm^{-1}K^{-1}]$
μ	Dynamic viscosity	$[kgm^{-1}s^{-1}]$
μ_t	Eddy viscosity	$[kgm^{-1}s^{-1}]$
ν	Kinematic viscosity	$[m^2s^{-1}]$
ρ	Density	$[kgm^{-3}]$
ρ	RANS model coefficient	$[-]$
τ_{ij}	Reynolds stress tensor	$[-]$
ϕ	Reduced stress function	$[-]$
Ω	Vorticity magnitude	$[s^{-1}]$
ω	Specific dissipation rate	$[s^{-1}]$

Subscripts

Symbol	Meaning
avg	Average
aw	Adiabatic wall
ax	Axial
c	Coolant
cr	Critical
in	Inlet
is	Isentropic
lc	Liquid crystal
out	Outlet
p	Constant pressure
ref	Reference value
s	Surface
t	Total quantity
tr	Transition
tan	Tangential
∞	Freestream

List of Figures

List of Tables

1 Introduction

A higher turbine inlet temperature is desired to improve the efficiency of aeroengines, leading to gas turbine nozzle guide vane (NGV) being susceptible to high thermal loads. The turbine inlet temperature of modern gas turbines has surpassed the temperature resistance limit of the vane material. Therefore, the nozzle guide vane is often equipped with film cooling technology. Film cooling and thermal barrier coating are methods that have allowed to facilitate the increase of the turbine inlet temperature. The high thermal loads pose a threat of mechanical failure of which creep and thermal fatigue are two of the most prominent failure modes [1]. Hence, an estimation of temperature distribution locally around the vane is essential for vane lifetime prediction. The flow over an NGV is generally quite complex and highly turbulent with multiple secondary flow structures. A horseshoe vortex, which forms due to interaction between vane and endwalls, has been shown to considerably increase the heat transfer coefficient locally. The highest thermal load, however, is typically observed on the leading edge of the vane at the stagnation point. Thus, this region can be equipped with multiple staggered rows of film cooling holes and is often referred to as showerhead film cooling.

The outflow from the combustor can influence turbine performance and heat transfer on the nozzle guide vane. The combustor outflow typically is a highly turbulent flow field. Lean burn combustion is implemented in modern aeroengine combustors to reduce produced NOx emissions. Swirl generators are used to guide a fraction of air to take part in the combustion reaction to reduce peak temperatures and the production of thermal NOx [2]. Furthermore, a swirl can help to stabilise the flame in the combustion chamber. However, the swirling motion is often preserved at the inflow of the gas turbine nozzle guide vane, thus, potentially causing aerodynamic loss. Especially, if a vane is designed for an axial inflow. In addition, the highly swirled flow is likely to influence the showerhead film cooling performance.

A numerical study through Computational Fluid Dynamics (CFD) modelling is performed to analyse the showerhead film cooling performance and the effect of a swirling inflow. Reynolds Averaged Navier-Stokes (RANS) modelling is still the industry norm, and researchers have been trying to develop turbulence and laminar-turbulent flow transition models. The turbulence modelling error is one of the main limitations of CFD RANS methods. To reduce this limitation, scale-resolving hybrid RANS-LES or full-scale Large Eddy Simulation (LES) formulations are introduced in gas turbine flow problems, since the development of modern computers can gradually facilitate the increased demand for computational resources. The need for more reliable and higher fidelity results is a reason for performing more scale resolving simulations. The hybrid RANS-LES modelling is expected to become an industry norm by 2030 [3], and it could be implemented in design routines at a reasonable computational cost. Especially, heat transfer and temperature predictions of high pressure stage vanes and blades would benefit from the implementation of scale resolving simulations [4].

Showerhead film cooling has been extensively investigated using RANS methods, however, there are only few attempts [5] calculating cooling effectiveness with hybrid RANS-LES models. Turbine-vane interaction has been studied both with RANS and scale resolving models in the last couple of years [6]. The general flow field can be effectively simulated with RANS methods, however, a scale resolving

simulation is desired when airfoil heat transfer, radial temperature profile, or flow mixing is of importance [6]. The current study aims at implementing hybrid modelling for a flow around an NGV with showerhead film cooling, and to investigate the influence of swirl on film cooling performance. A study by Wu et al. [7] established a swirling inflow effect on showerhead cooling with RANS, showing the predicted shift of the stagnation line. The study by Ravelli et al. established the benefits of the hybrid DDES model. The unsteadiness of the mixing layer between coolant jets and the main flow, and anisotropic turbulence are two phenomena that the scale resolving model was able to capture [5], signifying deficiencies of RANS. The study implemented a relatively large blowing ratio of $BR = 3$ and a uniform inflow, resulting in a clear coolant lift-off from the vane surface. A lower blowing ratio can lead to increased cooling effectiveness downstream of a cooling hole, although at the leading edge region the coolant is susceptible to lift-off even at moderate blowing ratios [5]. Blowing ratios $BR < 2$ are investigated in the current study, and the Scale-Resolving hybrid (SRH) model is implemented from the $Star - CCM+$ software package. It is, of course, critical to avoid hot gas ingestion, hence, a higher blowing ratio can be desired in practical applications. Showerhead film cooling physics of gas turbine nozzle guide vane flow are difficult to model due to strong mixing between coolant jets and the mainstream flow, and due to highly turbulent inflow from the combustion chamber.

Giel et al.[8] performed heat transfer measurements on non-cooled linear cascade of blades, and this experiment is used to validate the CFD methodology. The experimental case is replicated and the convective heat transfer coefficient (HTC) is calculated on the blade surface. The attention is put towards capturing the effects of the secondary flows, such as the horseshoe vortex. A highly complex flow field is developing close to the endwalls that is a challenge for RANS CFD modelling. Thus, the report consists of two separate analyses. The HTC calculation for the validation case of a non-cooled vane at various flow conditions, and the showerhead film cooling analysis in terms of adiabatic cooling effectiveness.

1.1. Aims of the thesis

The following are the goals of the study:

1) To validate a CFD RANS methodology and the most applicable turbulence models. The CFD results are to be compared to the experimental data of HTC distribution on a blade that is subjected to a strong horseshoe vortex.
2) To investigate the effect of swirl on showerhead film cooling performance for a turbine NGV.
3) To establish the benefits of hybrid RANS-LES modelling for heat transfer and film cooling problems.

The following steps are taken in the research. First, an extensive literature study is performed primarily to study CFD modelling and various turbulence models, it is presented in Chapter 2. The implemented methodology for the validation case of an uncooled vane, and the implemented method for the showerhead film cooled vane analysis are described in Chapter 4. Notably, these are two separate analyses, the validation case is focused on the HTC data, and the film cooled vane on the adiabatic cooling effectiveness. Similarly, results in Chapter 5 are first presented for the uncooled vane together with a comparison to experimental data of the HTC. Then, the showerhead film cooling results are shown, following a discussion of results in Chapter 6.

2

Literature Review

This section provides an overview of the literature study. Flow physics in the nozzle guide vane and film cooling technology are reviewed. A brief history of heat transfer coefficient prediction methods on gas turbine nozzle guide vanes is presented, followed by a summary of the current state-of-the-art CFD methods. Subsequently, a review of the most successful turbulence models for CFD RANS methods is provided with a focus on capturing secondary flow phenomena on an uncooled vane, and cooling effectiveness on a film-cooled vane. Finally, the importance of representative turbulence boundary conditions is investigated.

2.1. Flow physics in the gas turbine nozzle guide vane

Flow physics of gas turbine nozzle guide vane and cooling technology are the basis of the current study. A high inlet temperature in gas turbine is desired to increase the thermal efficiency and performance of the engine. Hot gas coming from the exit of combustor is flowing over the nozzle guide vane (NGV). The flow typically has a high turbulence intensity with a non-uniform temperature profile, and a non-uniform velocity distribution. The calculation of external HTC is necessary to design a cooling scheme, and to estimate the lifetime of the vane. The material, which the NGV is made of, is required to withstand the high temperature of the gas coming from the combustor. Over the years new cooling designs have facilitated the increase of turbine inlet temperature to improve the efficiency of the engines. Film cooling has allowed to reach turbine inlet temperature higher than the allowable limit for the metal vanes (around 1200 K) [9]. The development of turbine inlet temperature increase up to year 2000 is shown in Figure 2.1.

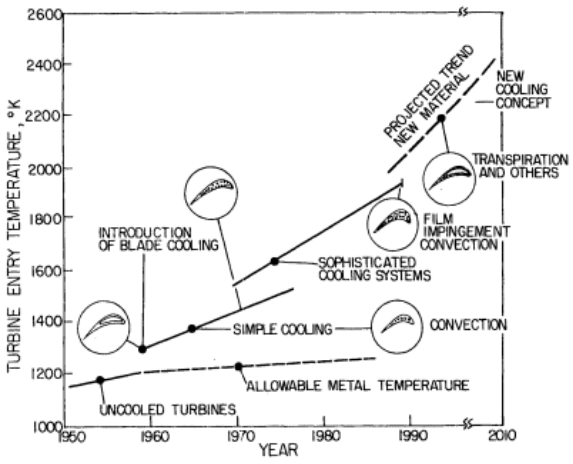

Figure 2.1: Development of turbine inlet temperature and evolution of cooling technologies. From Lakshminarayana [10].

First, the flow physics in an uncooled vane are discussed since the same phenomena are applicable to a cooled vane. In terms of aerodynamic losses, various loss sources can be identified for an uncooled vane. Profile losses and annulus losses arise due to the skin friction on the blade surface and endwalls, respectively [1]. The secondary flows in forms of vortices contribute to losses as some parts of the fluid are guided to move in directions other than the mainstream flow. The breakdown of various structures of the secondary flow in high pressure gas turbine nozzle guide vane is visualised in Figure 2.2 on a magnified scale. Furthermore, trailing vortices arise when the flow is separating at the trailing edge forming a wake. The other secondary flow structures including horseshoe vortex, passage vortex and corner vortices form within the cascade and are relevant to NGV heat transfer problems, since these vortices interact with the airfoil surface. These secondary flows in the gas turbine nozzle guide vane are evolving due to presence of an endwall boundary layer. Experimental research in the last century has enabled to understand the flow field around a gas turbine vane. The secondary flows can lead to up to 20% of total loss for a gas turbine nozzle guide vane [11]. In gas turbines, the secondary flows increase heat transfer on the vane by mixing the hot mainstream gas into the airfoil and endwall boundary layers. Not only the vane itself is susceptible to high metal temperatures, but the endwalls as well. Downstream of the trailing edge, heat transfer on the endwalls is mainly dominated by the secondary flow field. On the airfoil surface, the secondary flow effects can extend up to 1/3 of the span [12].

Horseshoe vortex system as visualized by Wang [13] in Figure 2.2, forms on the endwall in front of the leading edge of the vane and it is the strongest of secondary flows around an uncooled nozzle guide vane. The formation of it is associated with the endwall boundary layer, which ”rolls up” in front of the vane leading edge, forming a vortex. Then the horseshoe vortex bends over the airfoil as shown in Figure 2.2, separating in suction side leg and pressure side leg. The suction side leg of the horseshoe vortex is stretched due to flow accelerating over the airfoil suction surface, and eventually it dissipates. The suction side leg of the horseshoe vortex, typically, has a weaker influence on heat transfer. The pressure side leg of the horseshoe vortex system is guided towards the suction side of the adjacent vane due to the positive pressure gradient. As it enters the passage further downstream, the multivortex structure gradually forms into a part of the passage vortex [14]. Then, the vortex ”impinges” on the suction side surface, causing an increase in the HTC in that region as displayed in Figure 2.5a. Furthermore, both suction side and pressure side legs of the horseshoe vortex lift off the endwall and are guided towards the midspan as the flow progresses over the vane.

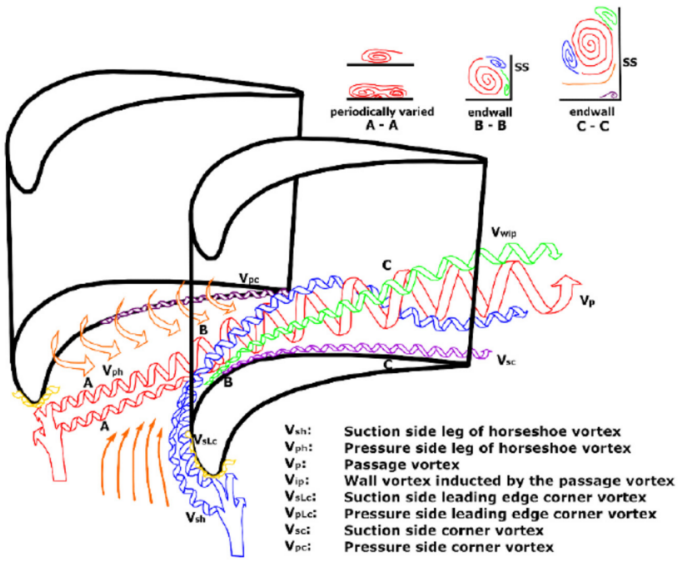

Figure 2.2: A visualisation of secondary flow field consisting of horseshoe vortex, passage vortex and corner vortices from Wang et al. [13]

The passage vortex grows in size but reduces its strength further downstream whilst staying close to the endwall. As the vortex attaches to the airfoil, the HTC on the vane is increased close to endwall

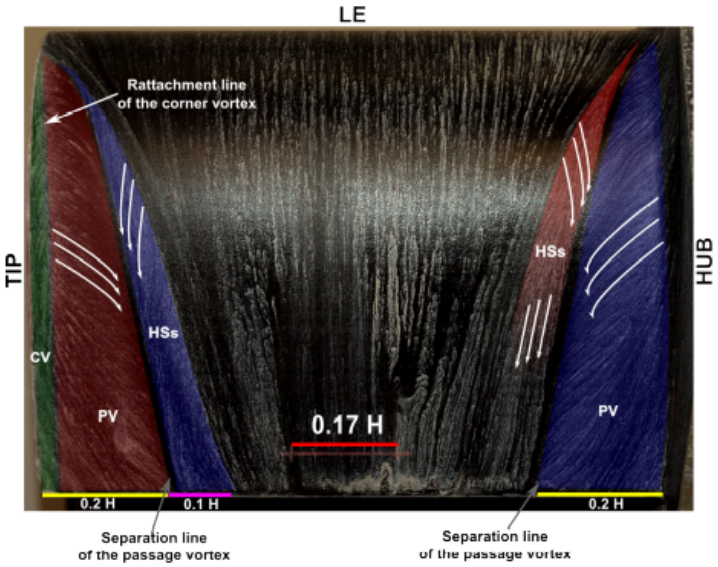

Figure 2.3: Passage vortex (PV), suction side leg of the horseshoe vortex (HSs), and corner vortex (CV) with oil visualisations, from Fontaneto [9].

on the suction side all the way downstream to the trailing edge. This is shown in Figure 2.5a where there is an enhanced HTC close to the endwalls. The region of low HTC right next to it, is where the passage vortex is separating from the vane surface. The interaction between the suction side leg of the horseshoe vortex and the passage vortex is a detail on which there has been some disagreement in the past [15]. As shown in the visualisation by Wang et al. [13], the suction side leg of the horseshoe vortex is demonstrated to wrap around the passage vortex, eventually merging with it. Goldstein and Spores [16], however, argued that the suction side leg of the horseshoe vortex travelled on top of the passage vortex without merging together. Notably, both of the vortices have an opposite rotation but passage vortex is, typically, stronger. Vortices are also forming at the corners where the vane is connected to the endwall. These are smaller vortices in strength, however, they are relatively easy to spot in experiments and are demonstrated by Wang et al. in Figure 2.2 and with oil flow visualisation in Figure 2.3.

Lean burn technology is widely used in modern aero-engines to reduce the NOx production. Efficient mixing process in the combustion chamber and stable flame anchoring are ensured through strong swirling flows that generate vortex breakdown [17]. However, the swirl motion is conserved to the entry section of high pressure turbine and influences the flow field over an NGV. Swirl motion modifies the radial distribution of aerodynamic load on the vane [17]. Swirl introduces a secondary flow structure contributing to aerodynamic loss [18], and it interferes with heat transfer on the vanes [19]. Furthermore, it can interfere with the coolant flows. The combustor-vane flow field interaction and swirling flows are typically unsteady, implying to implement transient simulations in numerical analyses. Cubeda et al. [6] investigated the effect of the inflow condition to aerothermal results prediction on the NGV. The authors suggest that implementing an inflow profile obtained from a scale resolving simulation of combustor considerably improves heat transfer predictions around the NGV. Furthermore, a complete effect of flow unsteadiness on turbulent mixing can only be captured by using a joint combustor-NGV model consisting of a computational domain integrating both the combustor and the NGV [6].

Nozzle guide vane is a stationary part and is directly connected to endwalls. Flow physics analysis for a rotor, however, is more complicated involving additional secondary flow structures. Tip leakage flows arise due to the gap between rotor tip and the endwall, introducing a tip clearance loss [1]. Furthermore, the centrifugal and Coriolis forces are influencing the flow field around a rotor blade.

Cooled vane

A nozzle guide vane is often cooled to accommodate the highest possible turbine inlet temperature in

the gas turbine. Internally cooled and film cooled vanes are considered in practice. Channels for a coolant inside the vane are designed for an internally cooled vane and the cooling is achieved by convection. Internal cooling does not interfere with the external flow over the NGV as long as the coolant is not released, for example, through the tip of the trailing edge. A higher cooling effectiveness, however, can be achieved by means of film cooling. The cooling channels inside the vane are carefully designed not only to benefit internal cooling but also rigidity of the blade [1]. There are multiple technologies to increase the heat transfer between the coolant and the inside surface of the blade. The internal channels can be designed consisting of ribs that reduce the boundary layer thickness and increase the turbulence in the internal channels. Pins are implemented with a similar purpose to increase the heat transfer. Jet impingement is another technique to cool a vane through convection by directing strong jets towards the inside surface of the vane. Jet impingement cooling is often applied to the leading edge of a vane or blade. In addition, a thermal barrier coating can be applied to a vane. The coating layer has a considerably lower thermal conductivity, hence, it helps to reduce the conductive heat transfer and metal blade temperature.

Film cooling implements the air which is used to cool the blade internally via convection, and discharges it in a carefully designed pattern of holes. The air forms a protective film of a relatively cooler air at the blade surface. Therefore, the external heat load to the blade is reduced due to reducing the driving temperature from the local gas temperature to the film temperature [1]. Film cooling effectiveness is expressed with the Equation 2.1. Theoretically, the maximum achievable effectiveness is 1.0 when the film temperature T_f is equal to the coolant temperature T_c. Typically, at the exact location of ejection point the effectiveness can be slightly above 0.50 [1]. Further downstream, the presence of hot freestream gas causes the film temperature to rise which reduces the effectiveness quite quickly, the effectiveness can be reduced below 0.10 around 20 hole diameters downstream [1]. A single row of film cooling holes is effective in reducing the heat load in the immediate vicinity downstream of the holes before the coolant mixes out with the mainstream flow. Multiple cooling rows on an NGV are implemented to reduce the heat load in a larger area of vane surface.

$$\eta_f = \frac{T_g - T_f}{T_g - T_c} \tag{2.1}$$

Implementation of film cooling comes with the expense of aerodynamic performance. Aerodynamic and enthalpy losses arise from mixing between the coolant and the main flow. The temperature difference drives the heat flux that reduces the enthalpy of the hot mainstream gas to the level of a cooler film flow, whilst the mixing process causes an irreversible conversion of the mainstream momentum to entropy [9]. Hence, an additional loss source is introduced as compared to an uncooled vane. In his publication of loss mechanisms in turbomachines, Denton [20] defined loss components in the flow with injected coolant by means of energy balance as reported in Equation 2.2.

$$W = W_{is} - Q - S = W_{is} - \int (T - T_{t,g}) dQ - T_{t,g} c_p (\kappa - 1) Ma^2 (1 - \frac{V_c}{V_g} cos\beta) \dot{m}_c \tag{2.2}$$

The term W_{is} is the isentropic work, the term Q is the heat subtracted from the mainstream gas. The last term S denotes the entropy production due to mixing process. The Equation 2.2 implements a definition by Shapiro [21] on the entropy increase for an irreversible process of mixing between a mainstream flow and a ”small amount” of injected flow. Notably, the entropy production largely depends on the angle α at which the coolant is injected with respect to the mainstream flow, according to Equation 2.2. Mass flow and velocity of the coolant flow are also of importance, hence, the size of the cooling holes should be designed with care. Furthermore, the coolant interferes with the main flow and influences the boundary layer. The coolant trips the flow close to the leading edge, causing a laminar-to-turbulent transition [8] which is an important parameter in heat transfer problems.

A typical setup of NGV cooling is visualised in Figure 2.4. It consists of film cooling at the leading edge, also called showerhead cooling. Further downstream, a single or multiple rows of film cooling holes are placed perpendicularly to the streamwise direction on the pressure and suction sides of the vane. The coolant is fed inside the vane through passages that, typically, are designed such that coolant flows in multiple parallel passages forming a heat exchanger. These passages are placed between the insert, referred as ’tube’ in Figure 2.4, and the blade surface. The passages are separated by ribs

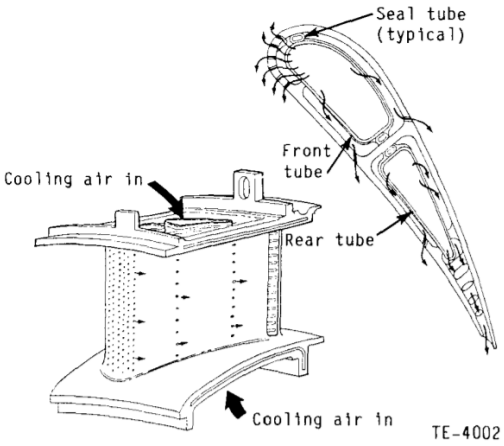

Figure 2.4: A typical setup of film cooling on turbine NGV, from Nirmalan [22]

whose function is to increase the surface contact area between the blade material and coolant. Furthermore, the rib design is important for structural integrity and durability of a vane [1]. Cooling design largely depends on the performance and manufacturing cost requirements of NGV, and the overall performance parameters of a gas turbine. Hence, heat load on the external surface is not the only parameter to consider in design, aerodynamic loss, coolant thermodynamic properties, and mechanical integrity are as important. Even though cooling configurations similar to the one displayed in Figure 2.4 are implemented often, a cooling hole placement in such rows is not a universal design, and the hole arrangement can be optimised.

Film cooling technology is also applied to endwalls. Lean combustion technique has been implemented to reduce the peak combustion temperature to limit NOx production. However, a flatter turbine inlet temperature distribution can often be a consequence of this technique, increasing the thermal load on endwalls [23, 24]. These considerations imply to develop thermal management methods for the endwall, such as endwall contouring and film cooling. Endwall contouring can allow to reduce the strength of horseshoe vortex and diminish turbulent mixing between coolant and mainstream [25]. The endwall coolant flow is dominated by the secondary flows [26]. Various different cooling patterns can be applied to the endwall. Zhang [24] performed a numerical study of a cooled endwall with coolant injection through holes placed in the channel between adjacent vanes. Thomas et al. [27] performed both experimental and numerical studies, placing cooling holes in two rows upstream of the vane leading edge. Furthermore, a purge flow cooling can be applied when the coolant is injected through a slot leakage from the combustor-turbine interfacial cavity [28].

2.2. Development of gas turbine vane HTC calculations

Estimating the HTC around turbine vanes has been of importance in turbomachinery ever since the invention of a gas turbine. Some of the early attempts capturing and calculating the HTC distribution were made using flat plate Nusselt number correlations based on experimental data. Simoneau [29] reviewed the methods in 1993 stating that some of the recent experiments on cascades had enabled the beginning of three-dimensional code development whilst the efforts of predicting laminar-turbulent flow transition were still mainly based on flat plate correlations. The experiments investigating gas flow over a flat plate helped to raise understanding about main physical phenomena and by the 1970's boundary layer codes were developed, such as *STAN5* [30] which then served as the basis for *TEXSTAN* [31]. However, these two-dimensional codes were not able to capture three-dimensional flow phenomena. During the same time period, the inviscid Euler solutions emerged, and later in the 1980's three-dimensional Navier-Stokes codes were developed, as summarised by Denton [32].

For the past thirty years, CFD has been used extensively to study heat transfer problems in gas turbines. The focus in the literature study is put on assessing various RANS models. RANS and Large Eddy Simulation (LES) are two of the most widely used CFD methods. LES can capture unsteady

flow effects, however, its computational cost is still too high for industrial expectations [33, 34], which is one of the main advantages of RANS methods. Similarly, DNS (direct numerical simulation) is a valuable method for discovering detailed flow structures but is not viable to use in regular industrial applications. Some of the other interesting developments include using hybrid LES-RANS, zonalisation and detached-eddy simulation (DES) [34]. Such hybrid LES-RANS methods would reduce some of the high grid demands whilst still being able to capture the unsteady turbulent flow structures [35]. The recently developed Stress-Blended Eddy Simulation (SBES) model by Menter [36] has been shown to be promising amongst the hybrid LES-RANS formulations. The SBES improves the shielding of RANS-modelled boundary layers and a rapid transition between LES and RANS formulations.
Some other solutions to improve CFD analysis are to use data-driven algorithms and extended RANS methods. Physics informed machine learning can be used to improve the turbulence models [37]. Such methods could be used to predict the Reynolds stress tensor. However, a potential problem is that the flow cases are vastly different from each other which could create a bias in the models. Nonetheless, there are no universal turbulence models which can predict greatly differing flows either. Unsteady RANS simulations or URANS is an extension of RANS which are able to include slow and unsteady flow effects. URANS is computationally less expensive than hybrid RANS/LES and LES itself, however, the use of sophisticated turbulence modelling closures is still required [38], similarly as for RANS analyses. Another modification of RANS is the partially-averaged Navier-Stokes (PANS), proposed by Girimaji [39], which serves as a ”bridging model” between DNS and RANS. The model aims at resolving turbulence anisotropy and introduces additional parameters which are the ratio of unresolved-to-total kinetic energy and the ratio of unresolved-to-total dissipation rate [35]. Hence, the two extremes depending on those parameters would be that either all of the turbulent structures are fully modelled as in RANS, or calculated as in DNS. As expected, this model is computationally more expensive than RANS but can largely reduce the cost for modelling complex flows as compared to DNS and detached eddy simulations. Seok et al. [35] implemented PANS using the open source CFD tool *OpenFOAM*, however, it can also be used in commercial software since only the RANS model coefficients should be changed [40].

The industry standard up to this day is RANS modelling due to its availability and comparatively lower computational cost. The cost of the more sophisticated LES and DNS is still too large for routine everyday use [41, 42], however, the hybrid RANS-LES formulations are introduced with the aim to bridge this gap. The literature study is focused on RANS methods and investigating various turbulence models and their performance. However, certain limitations exist for these methods which shall be addressed. First of all, turbulence and transition modelling is an important aspect of CFD methods which naturally imposes modelling errors. Various turbulence models have been developed for Reynolds stress tensor closure with different performances at specific flow conditions. Denton [32] states that high Reynolds number flows in turbomachinery are never steady, therefore large modelling error is imposed. In those cases, LES are expected to give more accurate results. Various models have been correlated to experiments with different flow conditions, and the models can be set up for various applications. According to Denton [32], it is not likely that a general turbulence or transition model will be developed which is superior to all others, at least until DNS can be used as a design tool. This is a well-known limitation of RANS which the researchers have tried to limit with correlations to experimental data. Furthermore, the experiments, with which the CFD calculations are often compared to, are also susceptible to unknown boundary conditions, such as free stream turbulence intensity [32]. Nevertheless, CFD is an immensely valuable tool for turbomachinery design but multiple uncertainties should be taken into account.

Important factors for HTC evaluation on gas turbine vane are boundary layer thickness, laminar to turbulent boundary layer transition, turbulence modelling, freestream turbulence, surface roughness, secondary flows, pressure gradient and others. The complexity of heat transfer nature is the reason why sophisticated CFD methods are generally used for the prediction of HTC. A thinner boundary layer leads to a higher HTC which is usually observed when investigating the HTC at the leading edge of a gas turbine vane Figure 2.5b. Increased turbulence levels also increase heat and mass transfer, furthermore, higher freestream turbulence tends to suppress the boundary layer thickness on endwalls, as found by Giel et al.[8].The correlation of HTC and boundary layer thickness holds for either a fully laminar or a fully turbulent boundary layer, however, before a boundary layer becomes fully turbulent it is in a transitional state. In a gas turbine nozzle guide vane, the boundary layer can be in the transitional

state for a significant portion of the vane surface [29] unless the boundary layer is turbulent due to high freestream turbulence intensity or a coolant flow triggers an early transition. The transitional boundary layer largely increases the HTC [43], therefore capturing transition correctly is of great importance in heat transfer problems.

Some of the typical examples of calculated Stanton number and HTC distributions are shown in Figure 2.5. The transitional region in Figure 2.5b is vividly apparent on the suction side of the vane where the HTC is rising, according to experimental data from von Karman Institute on vane *MUR235* [44]. Notably, the three different turbulence models were reported to achieve only limited success trying to capture this phenomenon in the particular study. In Figure 2.5a a three-dimensional Stanton number (St) distribution is shown for different freestream turbulence length scales, and the Stanton number is proportional to the convective HTC. Notably, the Stanton number increase at the leading edge is expected, and there is also a considerable increase close to endwalls on the suction side which is the effect of secondary flows as explained in more detail in Section 2.4.

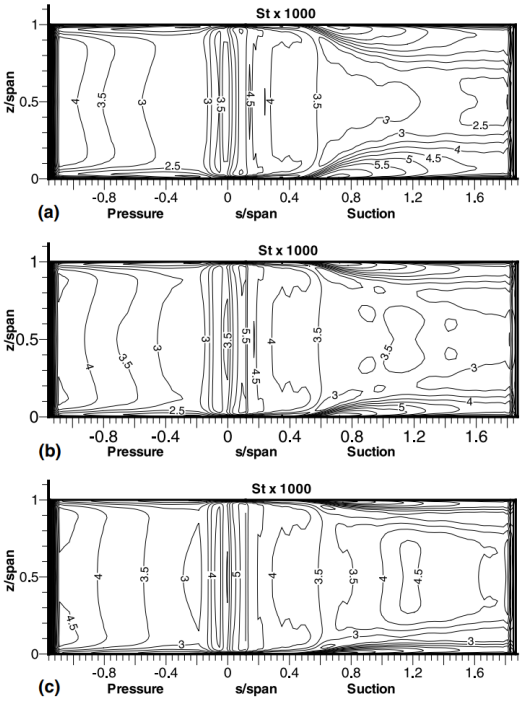

(a) Stanton number distribution on a transonic turbine vane using $k-\omega$ turbulence model at turbulence intensity of 9% and with varying turbulence length scales a) length scale = 0.03, b) length scale = 0.09 c) length scale = 0.23. From Garg & Ameri [45]

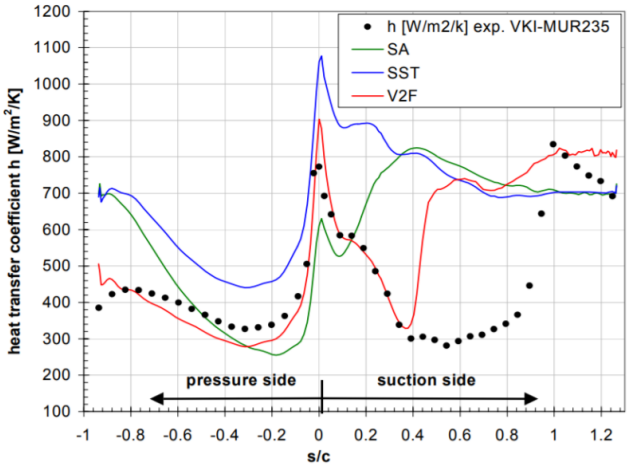

(b) Two dimensional HTC distribution for transonic guide vane MUR235 at midspan, measurements together with the results of three different turbulence models for a flow with transition, from Pecnik et al. [44]

Figure 2.5: Examples of typical three dimensional and two-dimensional Stanton and HTC distributions around a transonic turbine nozzle guide vane. Effects of secondary flows shown in Figure 2.5a and transition behaviour in Figure 2.5b

Conjugate heat transfer is of great interest in research as well. A conjugate model incorporates both convective and conductive heat transfer, where the solution of one mode is providing the boundary condition to the other. Often these models are effective when analysing the cooling performance of internally cooled gas turbine vanes since the fluid and solid regions have strong aerothermal interaction [41]. The thesis is focused on the analysis of a vane without internal cooling scheme, hence, a convective external heat transfer analysis is incorporated.

There are challenges that are likely to remain within the domain of RANS modelling in the future. Apart from the already established turbulence and transition modelling errors, Tyacke et al. [34] summarise that issues involve compressive and extensive strain, curvature and rotational effects, surface roughness and others. Surface roughness is of interest in gas turbines, especially considering the lifetime of components operating at high temperatures. Surface roughness influences skin friction, boundary

layer growth, laminar-turbulent transition and heat transfer. Typically a newly manufactured blade could be considered as smooth in CFD modelling, and it would be a good approximation for low Reynolds number flow. However, over the lifetime of the blade and in high Reynolds number flows in turbine the surface roughness can significantly affect the efficiency and loss coefficient [32]. If an effort is made to model the roughness then an option is to use roughness parameters in near-wall modelling, implement discrete element models accounting for blockage and obstruction drag, or fully discretise the roughness profile [46]. The latter is, naturally, the most accurate but in many applications would not be a feasible approach. Near-wall modelling is largely an empirical approach, hence it is apparent that rough surfaces are difficult to model with RANS methods.

2.3. Turbulence and transition modelling for gas turbine vane heat transfer

RANS methods require specialised models for estimating the small scale turbulence and this section aims at providing an overview of some of the most successful turbulence models. Not all of the different models can be realistically reviewed in this paper, however, the focus is on those which have proven to either provide accurate HTC predictions or are able to capture transition. Furthermore, more attention is shifted to those models which are available in commercial software tools because such tools will be used in the analysis.

2.3.1. Turbulence modelling

RANS averaging of flow quantities introduce a Reynolds stress tensor term which must be modelled or solved for. Eddy viscosity models are a class of modules for which eddy viscosity is estimated, and there are Reynolds stress models (RSM) which directly solve for the Reynolds stresses. Two of the simplest eddy viscosity models are $k-\varepsilon$ model solving for turbulent kinetic energy k and turbulence dissipation rate ε, and $k-\omega$ where ω is the specific turbulence dissipation rate. These were among the first models which emerged in the progress of CFD modelling. The $k-\varepsilon$ model requires damping functions on the wall which are not accurate for adverse pressure gradients [47], and the model is not able to accurately model transitional flows. Therefore, this model will not be investigated in detail. However, it forms the basis for some of the other, more advanced, models. The $k-\omega$ turbulence model does not require damping functions and is more applicable for turbomachinery purposes. However, the $k-\omega$ model, similarly as the $k-\varepsilon$ model, often overestimates turbulence production at the stagnation point, and also it is largely dependant on freestream turbulence conditions [48]. Both of these two-equation RANS models have an underlying assumption that the boundary layer is turbulent which is the reason for high turbulence production at the leading edge where usually the boundary layer is not developed to the turbulent state. The various methods to limit this overprediction at the leading edge and regions of a large normal strain include introducing parameters that modify the turbulent kinetic energy production term in equations like it is done with Kato-Launder constraint [49]. Some of the other methods dealing with this limitation of the standard $k-\omega$ model are the realisable $k-\varepsilon$ model and Durbin's realisability constraint which are described in the next paragraphs.

SST model

One of the proposed solutions to the leading edge anomaly is the SST $k-\omega$ model which includes the production limiter parameter. SST $k-\omega$ is a blended model which in principle uses $k-\varepsilon$ far away from the wall and $k-\omega$ close to the wall with a blended region in-between them [50]. This idea forms the basis of the SST $k-\omega$ model, or simply the SST (shear stress transport) turbulence model. The SST $k-\omega$ model has been shown [51] to prevent the unrealistic growth of turbulence kinetic energy at the stagnation point by means of implementing Durbin's realisability constraint [52]. SST $k-\omega$ turbulence model by itself cannot capture transition accurately, often predicting it at too low Reynolds numbers [53]. However, it is often used in conjunction with transition models, such as $\gamma - Re_\theta$ or one equation γ, where the additional transport equations are solved for intermittency (γ) and momentum thickness Reynolds number (Re_θ). The former makes up the SST $k-\omega\ \gamma - Re_\theta$ model which is widely used for heat transfer problems. Furthermore, the SST $k-\omega$ model has been shown to be capable of predicting secondary flow phenomena [12]. The SST $k-\omega\ \gamma - Re_\theta$ model should be included in the analysis when estimating HTC around a vane, and a more thorough literature review on it is in Section 2.3.2.

Moreover, a hypothesis is formed that the inclusion of the transitional model will considerably improve HTC predictions both at midspan of the vane and close to endwalls as compared to the original SST $k-\omega$ model, similarly as it was found by Papa et al. [14] for the endwall region.

Models based on $k-\varepsilon$

There are many turbulence models developed which are based on the two-equation $k-\varepsilon$ model. One of such developments is the RNG $k-\varepsilon$ model. Re-Normalisation Group (RNG) method by Yakhot et al. [54] was made in order to renormalise Navier-Stokes equations to improve accounting for small turbulence scales, and the model achieved considerable success at the time. However, the RNG $k-\varepsilon$ model, as found by [55], fails to capture the transition onset, and it overestimates heat transfer over the airfoil surface. The overall performance is significantly worse as compared to Reynolds stress models and transition SST $k-\omega$ model on the suction side of the vane.

Another non-linear $k-\varepsilon$ model is the realisable $k-\varepsilon$ which is introduced to limit the turbulence production at the leading edge. This model incorporates a realisability constraint on turbulence quantities, such as velocity fluctuation, turbulence kinetic energy k and ε [47]. Luo et al. [12] found that SST $k-\omega$ outperforms the standard realizable $k-\varepsilon$, even though the latter can successfully predict the general trend of HTC distribution. Another study [56] assessed the realizable $k-\varepsilon$ model and argued that the secondary velocities are underpredicted resulting in weak predictions of HTC on the endwalls and airfoil surface as compared to other turbulence models, like $\overline{v^2}-f$. Due to these reasons, both the RNG and realisable $k-\varepsilon$ models are not included in detailed analysis for an uncooled vane.

Another model which is based on $k-\varepsilon$ is the $\overline{v^2}-f$ model. The $\overline{v^2}-f$ model has been shown to have good performance in HTC calculations [23, 44, 56], especially well capturing HTC on the pressure side of the turbine vane [23, 57, 58] where there is no laminar-turbulent transition. This model is based on $k-\varepsilon$ but extended with a transport equation for wall-normal stress component v^2 of the Reynolds stress tensor [59] and includes an elliptic relaxation parameter f. Instead of calculating the evolution of eddy viscosity based on k, the evolution of eddy viscosity is calculated from the velocity scale v^2 representing velocity fluctuations normal to the streamline [59]. The model is designed such that near-wall turbulence effects can be estimated accurately which is of high importance in heat transfer predictions [60]. This is the main reason why the model has seen success in multiple flow cases in the literature.

$\overline{v^2}-f$ model is widely discussed in the literature, and it often gives satisfactory results in heat transfer problems. Hermansson et al. [56] found it to give good predictions of Stanton number on the endwall surface. The author stated in 2004 that due to implementing the square of the normal fluctuating velocity component v^2, the model is able to better capture heat transfer phenomena [56]. However, this paper dates back to 2004, and other models, such as the SST $k-\omega$ model together with $\gamma-Re_\theta$ transition, have potentially become superior. Furthermore, the $\overline{v^2}-f$ model is not able to accurately predict transition [58], therefore the HTC predictions on the vane suction side are often erroneous.

One equation Spallart-Almaras model was created for low turbulence intensity flows [44], therefore its applicability to turbine nozzle guide vane problem is very limited. Furthermore, Pecnik et al. found out that it largely underpredicts leading edge HTC and predicts transition falsely [44]. This model is quite popular for general CFD flow cases in the literature, however, it has not been used as extensively as SST $k-\omega$ or $\overline{v^2}-f$ models for heat transfer problems and its performance is not comparable either. Therefore, this model will not be included in the analysis.

Standard $k-\varepsilon$ model requires damping functions at the wall but another method to model the viscous sub-layer and the buffer layer is the two-layer approach which makes up the two-layer $k-\varepsilon$ model first proposed by Rodi [61]. The computations are split into two layers – the turbulent dissipation rate ε and turbulent viscosity μ_t are specified in the layer next to the wall as functions of wall distance. The estimated values of ε in the layer close to the wall are then blended smoothly with the values calculated far away from the wall [60]. The model still greatly relies on empirical correlations and its success in heat transfer problems has been very limited. Andreinini [62] investigated the two-layer $k-\varepsilon$ model for a three-dimensional flow in the endwall regions of a vane, and the model was not able to detect

any of the secondary flow effects. Its performance was not matching the other investigated turbulence models which were SST $k-\omega$ and $\overline{v^2}-f$.

Elliptic blending models

Elliptic blending models and elliptic relaxation parameters are of interest in complex flows. The elliptic blending concept was first introduced by Manceau & Hanjalic [63] in 2002 for Reynolds stress models. The aim of incorporating the elliptic parameter was to obtain a more accurate model for near-wall turbulence by evaluating the stress component normal to the wall. The turbulence anisotropy due to wall proximity is one of the main reasons for the use of these proposed parameters [53], hence an argument can be made that its performance is expected to somewhat emulate Reynolds stress models which are capable of capturing turbulence anisotropy, unlike the models based on Boussinesq hypothesis. Using these elliptic parameters as a basis, multiple two-equation models were developed, such as the $k-\varepsilon$ elliptic blending model. The aforementioned $\overline{v^2}-f$ model has the elliptic relaxation parameter implemented as well. A case with a flow over a curved surface was investigated by Lardeau and Billard [64], who also introduced a lag elliptic blending model as an extension to the classical elliptic blending model. The authors compared three turbulence models, elliptic blending $k-\varepsilon$, lag elliptic blending $k-\varepsilon$ and the SST $k-\omega$ with the LES data (see Lardeau [64]). Additional production terms are introduced for the lag elliptic blending model which are attributed to the "lag between stress and strain rate". Due to implementation of lag factor, the model can better account for curvature and rotation effects [53]. The results of comparing turbulence models suggest that both elliptic blending models provide a better agreement with LES calculations than the SST $k-\omega$ model for a flow with a strong curvature. Moreover, the lag elliptic blending model shows a considerable improvement with respect to the classical elliptic blending $k-\varepsilon$ model [64]. The flow in turbine nozzle guide vane has a strong curvature, therefore, it might be interesting to implement this model in heat transfer calculations and compare it with the SST $k-\omega$ and $\overline{v^2}-f$ models.

The lag elliptic blending model is comparatively newer than the other mentioned turbulence models, and, unlike the classical elliptic blending model, it has not seen that much use in the literature in heat transfer studies yet. Outside of the turbomachinery field a study by Xu investigated the model to predict transition in hydrofoils with a conclusion that it is able to predict the natural transition in a case where SST $k-\omega\,\gamma-Re_\theta$ fails to model it accurately [65], however, the bypass transition mode is the dominant one in gas turbines [29]. Biswas and Durbin continued to investigate the lag elliptic model in 2019 [66] after developing a lag formulation also for $k-\omega$ model [67]. The authors confirmed that flow over 2D complex curvatures is better predicted than with the SST $k-\omega$ model. Furthermore, the authors suggested that the model is also effective for three-dimensional diffuser flows with separation. However, these benefits of improved eddy viscosity predictions were not observed for flows with accelerating boundary layers [66].

Accounting for turbulence anisotropy

One of the challenges for eddy viscosity models is accounting for turbulence anisotropy when velocity fluctuations are different in various directions. By definition, the Boussinesq hypothesis implemented in EVM assumes isotropic turbulence. The elliptic blending models have reached some success in dealing with turbulence anisotropy, however, only by means of modelling it. Apart from eddy viscosity models, the other class of RANS models, Reynolds stress models (RSM), solve for all Reynolds stresses, therefore they are able to capture the anisotropy much better. This would also be promising for modelling secondary flows, as the anisotropy of Reynolds stresses largely drives the secondary flow phenomena [68]. However, RSM models are more prone to numerical instabilities and the solution can take a significant amount of time because there are more transport equations to solve as compared to two-equation turbulence models, like $k-\omega$. RSM also avoid turbulence production overprediction at the leading edge but the model is often unstable in complex flows [60]. Development of lag elliptic blending models aim at capturing the anisotropic turbulence whilst being considerably less expensive than full scale RSM. Casartelli et al. [69] applied various advanced RANS models in a study of centrifugal compressors. The models that implemented a measure of anisotropy provided a better agreement with the experimental data, and they were capable of modelling the turbulent secondary flow. Regarding

the SST $k-\omega$ model, a couple of non-linear constituent relations stemming from RSM concepts have been introduced to better account for turbulence anisotropy in eddy viscosity models.

Cubic relations [70] and quadratic [71] are two of such relations proposed to deal with turbulence anisotropy by extending the linear relation between the Reynolds stresses and the mean strain rate. The linear relation is shown to underpredict the turbulence anisotropy, and both quadratic and cubic constitutive relations are also implemented in the *Star-CCM+* software package. The quadratic relation between the Reynolds stresses and the mean strain rate allows for $k-\varepsilon$ based models to predict the secondary flows more accurately, which suggests that it might allow for models like $\overline{v^2}-f$ to achieve satisfactory modelling of turbulence. The cubic relation incorporates the cubic functions of the velocity gradient and this way extends the non-linear quadratic relation. Both of these non-linear relations can also be applied to the SST $k-\omega$ model, in fact, these relations partly contribute to the success of this model. The cubic relation does not achieve the detail in which RSM can account for turbulence anisotropy but it provides a powerful approximation without incorporating the usual drawbacks of RSM such as numerical stability and cost [60].

Wall functions and wall-integration are two methods to deal with the flow conditions in the proximity of the wall. Notably, if the computational mesh is fine enough close to the wall then the viscous sub-layer can be solved and no additional functions are needed to model it. The condition for wall-integration to be feasible is to have the y^+ value of the first cell next to the wall around or below one everywhere on the surface. The other approach would be to use wall functions and a coarser mesh, however, this approach is not as accurate and the HTC results are predicted erroneously, as found by Luo et al. [12].

Turbulence models and film cooling

In film cooling problems, it is of paramount importance to capture mixing between the coolant jet and the mainstream. Various turbulence models treat such mixing flows differently, and limitations should be acknowledged. Dyson et al. [72] report an overprediction of adiabatic cooling effectiveness with the SST $k-\omega$ model on the suction side of the vane for an attached jet. Similarly, the suction side adiabatic cooling effectiveness is overpredicted with the $\overline{v^2}-f$ model [73]. The reason for the overprediction is argued to be the limited jet diffusion predicted by the RANS model, although the general trend of effectiveness is captured successfully [5, 72]. Li et al. [74] report improved predictions when applying anisotropic turbulence parameters, signifying the importance of capturing anisotropic turbulence for such problems as well. Furthermore, an application of transition models can improve the prediction of coolant ejection from the channel into the mainstream [5]. The authors implemented realizable $k-\varepsilon$ turbulence model with enhanced wall treatment in their study. It was argued to provide more accurate predictions of laterally averaged cooling effectiveness in the leading edge region as compared to SST $k-\omega$ model.

Sillieti et al. [75] compared $\overline{v^2}-f$, RKE and SST models in a flow with fan-shaped film cooling holes. The authors compared CFD results with the experimental data, and RKE provided more accurate surface temperature predictions as compared to the $\overline{v^2}-f$ model. Overall, it was established that the RKE model provided the best agreement with the experimental data, especially in the region 2-4 cooling hole diameters downstream of the injection point [75]. Zhao et al. [76] also implemented RKE model in the showerhead film cooling effectiveness analysis due to its capabilities of providing accurate predictions in high speed airfoil flows. Lag elliptic blending $k-\varepsilon$ model has not been extensively implemented in film cooling problems, however, due to its similarities with the RKE and its capabilities of predicting complex flows, it can be of interest in the cooling analyses. Furthermore, the elliptic blending model is improved as compared to RKE in terms of accuracy in the near-wall region [60].

RANS methods are generally limited in terms of providing high fidelity results in problems involving mixing of two streams. Often the models predict a long streak of coolant flow able to avoid fully mixing out with the mainstream, which is not expected in real gas turbine application. Such pattern is visible, for example, in study by Zhao et al. [76]. Furthermore, RANS models by definition are not able to capture the inherent unsteadiness of the shear mixing layer between coolant and mainstream jets. Ravelli et al. [5] also reported large levels of turbulence anisotropy present in showerhead cooling regions, and

RANS models are not able to resolve such flow. Hybrid RANS-LES formulations can be implemented to ensure scale resolving in the regions where mixing takes place. Obviously, hybrid configurations or even full LES simulation increase the computational cost.

2.3.2. Transition modelling

An accurate prediction of laminar-turbulent transition length and transition onset, where the transition begins, is of paramount importance for calculating HTC distribution. Transition typically occurs on the suction side of a vane, and the boundary layer can be in the transitional state for a considerable portion of a non-cooled vane surface. For a film cooled vane, however, transition modelling is not an issue since the boundary layer is triggered to a turbulent state by the coolant [8]. Multiple approaches are developed to predict the laminar-to-turbulent transition location. Some turbulence models, like $\overline{v^2} - f$, rely on the turbulence closure model when computing transition. Pecnik et al. [44] showed that this method is able to capture transition in the study performed using the $\overline{v^2} - f$ turbulence model. However, many other turbulence models, such as the standard $k - \omega$, for example, fail to predict transition onset, and this approach for capturing transition "should not be relied on" despite some promising results by $\overline{v^2} - f$ model [53]. Other approaches for transition modelling are to use experimentally obtained correlations or to introduce additional transport equations [53]. Such methods have seen success in the form of the $\gamma - Re_\theta$ transitional model. Generally, transitional models are preferred for capturing transition because turbulence models are designed with an assumption that fully turbulent flows should be predicted, with the exception of low-Reynolds number $k-\varepsilon$ models which include damping functions near the wall [60].

$\gamma - Re_\theta$ transition model

As mentioned in Section 2.3, the SST $k - \omega$ turbulence model can be used in conjunction with the $\gamma - Re_\theta$ transition model by Menter and Langtry [77], and the success of the model has been proven in the literature. This transition model is based on introducing two transport equations for the intermittency function γ and momentum thickness Reynolds number Re_θ which is the criterion for the transition onset [77]. Therefore, SST $\gamma - Re_\theta$ has four transport equations to solve for (k, ω, γ and Re_θ).

The intermittency function describes the state of the boundary layer and the probability of it being fully turbulent. For example, γ = 1 when the boundary layer is fully turbulent and γ = 0 when fully laminar [60]. The transition onset is modelled by finding the momentum thickness Reynolds number Re_θ at a location where the transition begins. The calculation of Re_θ itself, however, is not implemented because the quantity in the model is related to a vorticity-based Reynolds number. The correlation of Re_θ is defined at freestream but is then convected and diffused into the boundary layer where this parameter is required to model transition, this way enabling to implement the information of freestream turbulence characteristics into the calculations of transition onset. The model is based on using local variables, thus the methodology is labeled as "local correlation-based transition modelling".[77]

The model has seen great success in the literature for capturing transition onset [14, 78, 79]. Papa et al.[14] also mention that heat transfer predictions on the suction surface are excellent in the three-dimensional flow regime in the vicinity of endwalls, however, the authors report overprediction of heat transfer at the leading edge, which is likely associated with the excessive turbulence production at the stagnation [14]. A recent study aimed to analyse heat transfer and transition predictions of the SST $\gamma - Re_\theta$ in a low pressure turbine stage, the results again suggested that the model is able to predict the spanwise distribution of transition onset. However, even though the general trends were captured, the $\gamma - Re_\theta$ predicted a late transition in the hub region and somewhat early at the midspan [80]. Generally, the $\gamma - Re_\theta$ model has proven its success over time but often the numerical results have not shown a perfect match with experimental data which, on the other hand, is not surprising, given the correlation-based nature of this transition model. As Dick and Kubacki mention in their transition model review in 2017, the $\gamma - Re_\theta$ has been used by many research groups over the years and the authors have not recorded a 'complete failure' of this model [79]. Overall, the $\gamma - Re_\theta$ model has been shown to possess transition predictive capabilities, which encourages the implementation of this model in the current research as well.

The original $\gamma - Re_\theta$ model by Menter and Langtry has been developed over the years with new correla-

tions. Smirnov and Smirnovsky [81] introduced modifications to the model in 2009, the main difference being an addition of a variable that limits the intermittency coefficient dissipation. The authors stated that the modified version provided a better agreement with the experimental data on turbine vanes [81]. Furthermore, the problem with the original model is that it cannot account for crossflow induced transition [82]. Therefore, Muller and Herbst aimed at extending the model further in 2014 by introducing an additional mode of destabilization [83]. The authors found out that the agreement with experimental data is satisfactory [83]. Following this development, Bode et al. validated the modified $\gamma - Re_\theta$ model which accounts for crossflow transition, and concluded that the model indeed can capture transition in three-dimensional flow with crossflow [82]. Bode continued studying this model and in 2018 introduced another criterion to better account for three-dimensional transitional behaviour and the impact of turbulence length scale [84]. The modifications by Muller and Herbst (see [83]) are also included as optional in the *Star-CCM+* software package [60] which is to be used in research at hand. Therefore, it is of relevance to investigate if crossflow transition plays a significant role in transitional behaviour close to endwalls or not. A hypothesis is that the crossflow can affect the flow due to the vortex structures close to the endwalls of the turbine nozzle guide vane.

Moreover, Suluksna et al. [85] introduced a correlation which is also implemented in the *Star-CCM+* software package, called Suluksna-Juntasaro correlation. Obtained by means of numerical experiments, the transition onset and transition length are controlled, and the correlation is established between a pressure effect parameter and momentum thickness Reynolds number Re_θ. To validate the model, the authors tested the correlation on a flat plate with different turbulence intensities and pressure gradients (see [85]). The original Menter $\gamma - Re_\theta$ model with the additional proposed parameters by Suluksna et al. is shown to agree with experimental measurements for moderate (1%-4%) and low turbulence intensities, however, for high freestream turbulence intensity (over 4%) the model predicted an early transition onset [85]. The authors concluded that the model is more suited to flows with low and medium freestream turbulence levels. Furthermore, the proposed model is shown to be able to accurately estimate flows with separation. The proposed model with Suluksna-Juntasaro correlation can accurately predict transitional behaviour induced by separation, and the results for flow separation and reattachment point predictions are satisfactory as well [85]. Hence, this correlation is especially of interest for flow cases with low or moderate turbulence intensities and also in the presence of strong pressure gradients. These findings suggest applying the Suluksna-Juntasaro correlation for cases with both low and high turbulence intensities in order to validate the statement that the model with correlation is not appropriate for modelling transition for cases with high turbulence intensities when comparing to experimental data from Giel et al.[8]. Giel et al. performed experiments with both low (0.5%) and high (8%) turbulence intensity at freestream conditions, the test case from here onward is referred to as the ”Giel cascade”.

Generally, $\gamma - Re_\theta$ is one of the most well-established transition models in the literature, and nowadays it is included in the majority of turbine nozzle guide vane heat transfer problems. Since it is a correlation-based model, multiple variations of it have been developed. Another transition model is one equation γ model which is a simplified version of the $\gamma - Re_\theta$ model [60]. The model was proposed by Smirnov and Langtry in 2015 and solves only for turbulence intermittency avoiding the transport equation for transitional momentum thickness Reynolds number [86]. Such modification simplifies calculations requiring less computing power, however, it is expected to be less accurate as compared to a more elaborated $\gamma - Re_\theta$ model. The γ transitional model also has the correlation for crossflow transition which on the *Star-CCM+* software can either be enabled or disabled in calculations [60]. This model can be used to compare or verify the calculations of $\gamma - Re_\theta$ and investigate whether there are significant differences in transition onset prediction. However, in the current study, it is not intended to include this model in the detailed analysis due to sufficient computational resources available for the more elaborate $\gamma - Re_\theta$ model.

$k_l - k - \omega$ transition model

The three equation transition model $k_l - k - \omega$ model by Walters and Cokljat [87] is shown to be able to capture transition behaviour. This model is based on laminar kinetic energy k_L, a concept that was first introduced by Mayle and Schulz [88]. Local parameters are used to predict transition onset [89],

similarly as for the $\gamma - Re_\theta$ model. Medina suggests that even though the original $k_l - k - \omega$ model over-predicts laminar kinetic energy (LKE) at turbulence intensities below 6%, the author also claims that this LKE transition model coupled with $k - \omega$ turbulence model provides excellent results [89]. The concept of laminar kinetic energy has been discussed further in the literature, and more variations of Walters' original model are created. A recent paper [90] introduces the $k_l - k - log(\omega)$ model which is developed further building upon the work of Bassi [91]. The authors of [90] claim that the improved $k_l - k - log(\omega)$ model is able to provide an improved transition prediction as compared to the well-established $\gamma - Re_\theta$ transition model. Salimipour [92] compared various modifications of the $k_l - k - \omega$ model for a flow over an airfoil with a separation bubble. Results were compared to DNS data, and the $k_l - k - \omega$ model was able to provide results closer to DNS data for separation-induced transition flow. For high angles of attack of around 14°, the model was shown to be able to capture the transition better than the SST $\gamma - Re_\theta$ model [92]. However, the original $k_l - k - \omega$ model is found to be computationally more expensive and has slower convergence than the SST $\gamma - Re_\theta$ model in a low Reynolds number flow study [93].

Overall, in the literature this three-equation transition model has not attracted as much attention to specifically heat transfer problems when compared to the $\gamma - Re_\theta$ model. An analysis of LKE based model in a flow over vane cascade was performed [94] without comparing results to the $\gamma - Re_\theta$ model. The authors concluded that the model was able to predict the high Reynolds number flow but the agreement with experimental data for low Reynolds number flow was limited [94]. Another study by Liu investigated specifically the transition performance for low Reynolds number flow applications. In this range, $\gamma - Re_\theta$ provides better transition onset predictions [95].

A study by Marconcini et al. [96] is one of the only few comparisons of an LKE based model and $\gamma - Re_\theta$ model in terms of secondary loss coefficient in a turbine nozzle vane cascade. The authors validated the LKE based transition model by Pacciani et al. [97]. The LKE based model was capable of accurately predicting transition onset on the pressure side of the vane. The model, however, overestimated the effect of horseshoe vortex, and the secondary flow penetration towards the mid-span was found to be predicted too large in high turbulence intensity cases [96]. In general, the simulated results were quite similar to the ones obtained with $\gamma - Re_\theta$ model. The secondary flow field was predicted slightly closer to experimental data by the $\gamma - Re_\theta$ model but LKE based model gave a better agreement on the pressure side of the vane. Hence, the LKE based model was able to predict the general features of the flow field, and it is interesting to follow the development of LKE based models further. The $k_l - k - \omega$ model is not available on some of the commercial software packages, like *Star-CCM+*, but it is incorporated in *ANSYS FLUENT* [98].

2.4. CFD modelling of secondary flows around gas turbine NGV

Secondary flows play a major role in high pressure gas turbine nozzle guide vane HTC predictions. These form a complicated structure of flow which is a challenge for CFD modelling. Not only do secondary flows directly affect heat and mass transfer in the flow but they also tend to sweep the coolant away from the surface in the gas turbines [29]. The flow structure in a high pressure gas turbine is rather complicated and largely three-dimensional with a typically high turbulence intensity. Secondary flows influence the flow close to the endwalls of a turbine vane. Hermansson et al. [56] estimated that 15% of the span is influenced by vortices close to the endwall for a relatively low turning angle, however, the extent of this depends on blade aspect ratio, endwall boundary layer and specific flow conditions. Luo et al. [12] investigated that passage vortex develops even up to $2/3$ of the half span at the exit of the flow channel within a cascade of vanes, hence it can be stated that not only the endwall but a significant portion of the vane itself is subjected to secondary flow effects. In case of a swirling inflow, another vortex is formed that can also be regarded as a secondary flow structure.

The evolution of vorticity of a particle depends on viscous forces and vortex filament stretching. Viscous forces lead to vortex eventually dissipating and the strength of vorticity to decrease. Vortex filament stretching can be visualised when imagining horseshoe vortex system, or corner vortices. The horseshoe vortex is forming as the vortex line of the endwall boundary layer is stretched and bent around the vane surface as visualised in Figure 2.6. In terms of quantifying strength of a vortex, a vorticity and Q-criterion can be implemented. Vorticity is formally defined as a curl of velocity [99]. The Q-criterion is

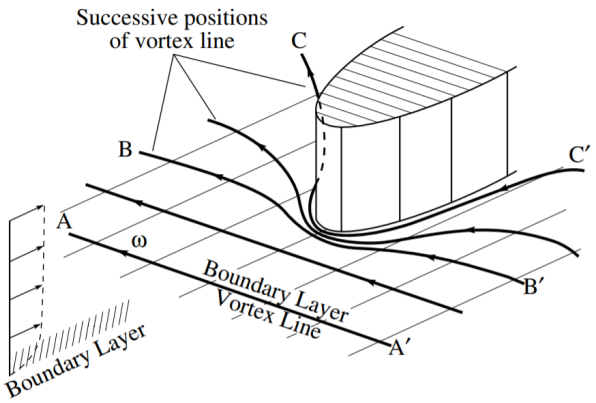

Figure 2.6: Vortex lines bending around the airfoil and forming the horseshoe vortex, from Greitzer [99]

a measure of vorticity with respect to the strain rate. It is defined in Equation 2.4 where Ω is a vorticity tensor and S the rate-of-strain tensor. A positive Q-criterion suggests that a particular region in the flow is vorticity dominated, a negative that it is strain or viscous stress dominated [60]. Isosurfaces of Q-criterion are often used to visualise vortical structures in the flow field in CFD analyses [15].

$$\Omega = \nabla u \tag{2.3}$$

$$Q = 1/2(|\Omega|^2 - |S|^2) \tag{2.4}$$

The conceptual theory on secondary flows is relatively well established in experiments. However, it is challenging to capture the three-dimensional effects in numerical simulations. The main structures interfering with the flow at the nozzle guide vane are the horseshoe vortex and the passage vortex together with smaller corner vortices [14]. A typical breakdown of these structures is visualized in Figure 2.2 on an amplified scale. As argued by Cui et al. [15], even though the general endwall flow features are widely accepted between researchers, there exists some disagreement on details regarding the interaction between passage vortex and the suction side leg of the horseshoe vortex, since different results have been reported in experimental cases.

The challenge in CFD RANS modelling is to capture those effects of secondary flows as they largely influence the HTC and losses. At the leading edge on the endwall where the horseshoe vortex is forming, heat transfer is enhanced due to roll-up of the endwall boundary layer [12]. The passage vortex impinges on the suction side of the airfoil which causes the increase of heat transfer there as well [14]. This effect is also shown in Figure 2.5a where an increased HTC is apparent on the suction side at the endwall region.

Secondary flows are mainly unsteady and LES could better capture such flows [15], however, a turbulence model should be used when relying on RANS calculations which forms a challenge to reduce the modelling error. Various studies have been performed to assess the performance of different turbulence models in predicting losses and HTC at endwalls and different locations along the span of the vane. Turbulence, transition modelling and turbulence boundary conditions remain the main modelling error sources when calculating secondary flow effects using RANS simulations. As already established, the unsteady nature of the secondary flows makes LES, URANS, DES and other more advanced methods interesting to implement, however, it is still a common practice to rely on computationally less expensive RANS and various turbulence models to estimate the secondary flow effects [55, 100]. Due to the strong anisotropy of turbulence, the Reynolds stress models are expected to be superior in evaluating the effects of secondary flows as compared to the eddy viscosity models, provided that numerical stability can be reached. Recently Li et al. [55] found RSM model providing results with a closer match to the experimental data as compared to SST and standard $k - \omega$ models on a vane close to endwalls, however, the transition prediction was not accurate. The eddy viscosity models can also be used to capture the HTC enhancement due to secondary flows but the limitations should be acknowledged.

Pecnik et al. [44] found that CFD RANS methods using eddy viscosity models are also able to capture the aerodynamic loss from the passage vortex.

Regarding the comparative assessment of different models, Luo et al. [12] state that the SST $k-\omega$ model outperforms the well-established $\overline{v^2}-f$ model in predicting heat transfer enhancement due to secondary flows. On the other hand, $\overline{v^2}-f$ has been used by many [23, 56, 101] to predict HTC on endwalls and at span locations close to endwall. Hermanson et al. [56] established that the $\overline{v^2}-f$ model is able to provide better predictions as compared to the realizable $k-\varepsilon$ and the two-layer $k-\varepsilon$ models, which is also in agreement with the literature on flows without secondary flow influence. Due to the use of elliptic functions in the $\overline{v^2}-f$ model it is expected to somewhat capture the three-dimensional flow phenomena due to its ability to deal with near-wall turbulence and turbulence anisotropy. This explains why the $\overline{v^2}-f$ model has gained attention for secondary flow problems in the past, however, these aforementioned authors published the studies in the period between 2003 and 2006 without comparing the $\overline{v^2}-f$ model performance with the SST $k-\omega$ model.

In the year 2015, Andreinini et al. [62] compared a two-layer model, $\overline{v^2}-f$, SST $k-\omega$, and SST $k-\omega$ $\gamma-Re_\theta$ models and their ability to predict the flow field and heat transfer along the span of a gas turbine vane. Notably, the various turbulence models provided contrasting results at different turbulence intensities. In most cases the two-layer $k-\varepsilon$ provided results largely differing from the experimental data, however, the other models were able to predict the Stanton number distributions to a certain extent [62]. For a low turbulence intensity (below 1%), the SST $k-\omega$ model provided the closest agreement with experimental data for the mean Stanton number on the endwall which agrees with the findings of Luo et al. [12]. Similarly, for a high turbulence intensity (around 19%) SST $k-\omega$ model estimated the mean distribution the closest to experiments, also calculating the general trend more accurately. However, none of the models were able to capture transition on the suction side of the airfoil at vane midspan for high turbulence intensity cases, whilst only the $\overline{v^2}-f$ model was able to reproduce the physical trend in low turbulence intensity case [62]. This is noteworthy since the SST $k-\omega$ coupled with $\gamma-Re_\theta$ transition model was not able to capture transition in this particular case. However, the authors reported an overprediction of the HTC at the stagnation point which suggests that turbulent kinetic energy production at the leading edge is likely large and transition onset is predicted to occur too far upstream as compared to experimental data. This can occur due to a mismatch of turbulence boundary conditions. Another study by Ameri [57] investigated the $\overline{v^2}-f$ model and concluded that even though the agreement with experimental data is relatively good on the pressure side, the suction side and effects of three-dimensional flows were not captured.

Overall, it seems that there is a consistency of the SST $k-\omega$ model being able to predict the three-dimensional flow effects better than the $\overline{v^2}-f$ model close to endwalls of the turbine vane despite $\overline{v^2}-f$ model being used predominantly in the older papers from the early 2000s. The authors of a recent study that involved analysis of leading-edge fillet influence on the secondary flow field also state that the SST $k-\omega$ turbulence model is the most applicable for evaluating secondary flow effects. Zhang et al. [24] arrived at a similar conclusion as well when comparing the original SST $k-\omega$ with SST $k-\omega$ coupled with the $\gamma-Re_\theta$ transition model. The authors stated that the two models provided representative results for a cooled endwall. Papa [14] added that coupling of the $\gamma-Re_\theta$ transition model to the SST $k-\omega$ turbulence model greatly improved the agreement with the experimental data in the three-dimensional flow region. However, in the qualitative comparison, it can be seen that the CFD results overpredicted the effect of the horseshoe vortex [14]. Another study by Wang et al. [102] compared the SST $k-\omega$ and standard $k-\omega$ models on the outlet guide vane endwall region. Heat transfer at the leading edge was again overpredicted as compared to experimental data. The horseshoe vortex was argued to be the main contributor to heat transfer near the leading edge [102]. Similarly, the secondary flow effect was overpredicted on the suction side leg of the horseshoe vortex as well.

Levchenya & Smirnov [103] analysed the horseshoe vortex on a symmetrical airfoil using SST turbulence model. The authors also found a system of horseshoe vortex, rather than one or two single vortices. These structures correspond to a corner vortex, horseshoe vortex, secondary vortex and tertiary vortex (in Figure 2.7 starting from the top), and they have also been found in experiments [103]. Notably, as found in simulations and also supported by Levchenya's findings, the core of horseshoe vor-

tex itself is the strongest among the four, followed by tertiary and secondary vortices. The authors also reported that spatial oscillations of endwall Stanton number distribution were observed in simulations, which is in accordance with experiments. However, the amplitude of tertiary and secondary vortex was predicted too large. The authors argued that it is due to the SST model's smoothing effect of the low frequency unsteadiness [103]. The modelling of this unsteady effect is outside of RANS capabilities. Furthermore, the finer mesh resulted in more smaller vortex structures appearing. The authors argue that, when comparing to the experimental data from Prasner & Smith [104, 105], the time-averaged pattern did not include the secondary vortex, however, at some instants it appeared when investigating temporal behaviour [103]. This discussion signifies that the unsteady effects of the secondary flows should be taken into account when high fidelity results are required. The SST model tends to predict HTC variations with a too large amplitude, and it tends to display structures which in experiments might appear only momentarily. Since a steady state RANS-based simulation cannot capture these unsteady effects, it remains as a limitation when modelling the secondary flow field.

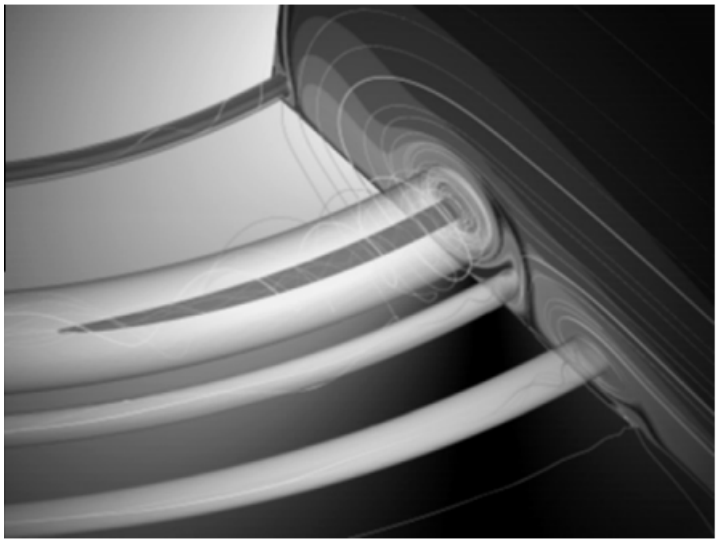

Figure 2.7: Horseshoe vortex system modelled by SST vortex upstream of the blade, from Levchenya [103]. Starting from the top where the leading edge is located: corner vortex, horseshoe vortex, secondary vortex, tertiary vortex. The authors also reported effect of grid resolution on this horseshoe vortex system.

Notably, even though the SST $k-\omega$ model is shown to be the most successful turbulence model in terms of capturing the secondary flow effects among the models readily available in commercial software packages, quite often the agreement with the experimental data is relatively modest due to the complicated flow structure. Even though the main three-dimensional flow phenomena are likely to be recognisable in the simulations, the question often remains how well these effects are captured by RANS methods and what is the extent of the turbulence and transition modelling errors. Furthermore, the lag elliptic blending $k-\varepsilon$ model has not been analysed in the literature for turbomachinery cases involving secondary flows. Due to its ability to better account for turbulence anisotropy, it is likely to capture the HTC enhancement due to secondary flows. The model has been shown to be incapable of accurately predicting transition location at vane midspan [58], however, it is worth exploring its performance in predicting specifically the secondary flow phenomena. It must be noted that the SST $k-\omega$ $\gamma-Re_\theta$ model can also be equipped with corrections for turbulence anisotropy and rotation [60], which, together with its superior performance in transition predictions, forms a likely reason why the newer lag elliptic blending model has not been extensively applied for HTC prediction on gas turbine vane cases in the literature.

2.5. Turbulence boundary conditions and HTC measurements

Freestream turbulence intensity and length scale greatly affect the HTC on the vane surface. Denton [32] states that the uncertainty in accurately obtaining the freestream turbulence intensity value in prac-

tical experiments is one of the main limitations of CFD modelling. If the turbulence intensity and length scale are not accurately measured or estimated, then the boundary condition in calculations would not be representative of the experimental case. Furthermore, studies [55, 106] have shown that the turbulence boundary conditions of length scale and intensity have a significant effect on heat transfer. A higher turbulence intensity at the inlet increases the turbulent spot production in the flow and ultimately the transition onset moves forward, i.e. the transition occurs at a lower Re_θ [43]. The $\gamma - Re_\theta$ transition model has incorporated the state of the boundary layer dependence on freestream turbulent conditions by introducing the Re_θ transport equation [77]. Eddy viscosity ratio, which is influencing heat transfer calculations, is computed by turbulence kinetic energy which, among others, is affected by turbulence intensity and length scale [58]. Hence, the turbulence models are also greatly affected by the incoming freestream conditions.

For example, the standard $k - \omega$ model is known to be sensitive to inlet turbulence intensity, and it also tends to overpredict turbulent kinetic energy production at the leading edge. Pecnik et al.[44] found that for a test case of high pressure flow passing over a stator vane the $\overline{v^2} - f$ model was more sensitive to turbulence intensity as compared to the SST $k - \omega$ model. Incoming flow turbulence conditions also affect secondary flow development. Garg & Ameri [45] stated that the turbulence length scale affects the influence of passage vortex, and a recent study by Li et al. [55], which implemented the RSM for turbulence modelling, concluded that freestream turbulence and length scale significantly affect the endwall flow field. Finally, film cooling effectiveness is also influenced by the freestream turbulence. A higher turbulence level can enhance mixing between coolant and the mainstream, reducing the cooling effectiveness [107]. Evidently, not only finding a suitable turbulence model is crucial, but an accurate estimation of turbulence intensity and length scale is just as important. In addition, it is desirable to investigate the sensitivity of HTC results to turbulence characteristics.

A CFD practitioner aims at using a representative turbulence length scale when comparing CFD results and experimental data but quite often the turbulence length scale is not measured in experiments. However, Steelant and Dick [108] developed a method that relates the local turbulence intensity to the flow acceleration through the channel. The derived expression can be used to find a proposed local turbulence intensity at the leading edge of the airfoil for comparison between numerical analyses with different turbulent length scales and experimental results. The authors validated the so-called Steelant-Dick postulation on a flat plate and linear blade cascades [108]. The postulation has been shown to be applicable for turbulence length scale estimation at the freestream condition [109]. Other studies [58, 110] have used Steelant-Dick approximation to find the inlet turbulent length scale but it has not been widely discussed in the literature and some more validation of this approximation is desired for other test cases. Giel et al. [8] have experimentally estimated the length scale in their test cases using hot wire measurements, and these values will be used as boundary conditions for the CFD calculations in the thesis. However, there are multiple aspects to consider when working with the measured values. Firstly, the accuracy of the measurements is often limited and, secondly, the definition of turbulent length scale is to be considered. The turbulent length scale to be specified in CFD RANS codes is usually found to be considerably lower as compared to the integral turbulence length scale measured in experiments, depending on how it is defined in RANS code when using commercial software [12, 45, 109].

3

Theory

The key theoretical concepts upon which the research is built are described in this chapter. First, convective heat transfer theory is provided in Section 3.1 which is closely tied to the boundary layer theory presented in Section 3.2. The boundary layer theory forms the basis for laminar-turbulent transition physics that are explained in Section 3.3. The parameters influencing film cooling performance are described in Section 3.4.1. Finally, the study aims to model the physics using computational fluid dynamics, thus, the CFD theory including turbulence and transition modelling is presented in Section 3.5.

3.1. Convective heat transfer

Convection and conduction are the two main modes of heat transfer in gas turbine vanes [10]. The convective heat transfer is significant in the gas turbine nozzle guide vane where a hot gas coming from a combustor is passing over a vane. Conduction is the heat transfer within a solid, hence important to consider when investigating heat transfer within the vane. External HTC is a measure of convective heat transfer which is in the presence of fluid motion. The enhancement of heat transfer by convection can be related to the heat transfer by conduction with the Nusselt number Nu. It is defined as $Nu = HTC \cdot L/\lambda$ where the HTC is the convective heat transfer coefficient and λ is the thermal conductivity. Correspondingly, Nu = 1 is associated with a case when heat transfer is purely by conduction, and large values above 100 represent a case where convection largely dominates with a turbulent flow present.

3.1.1. The heat transfer coefficient

The Newton's law of cooling states that the heat transfer is proportional to the temperature difference and the surface over which the heat is exchanged [111]. The constant of proportionality is denoted as the heat transfer coefficient (HTC) with units $W/(m^2K)$, and it relates the heat flux to the temperature difference. The HTC is defined in Equation 3.1, and it is an important parameter when analysing heat transfer problems.

The HTC is dependant on many properties of the flow. Considering flow over a turbine vane, the turbulence characteristics, secondary flows, boundary layer parameters and non-dimensional flow parameters affect the heat transfer. As summarised by [10] more specifically, the Nusselt number is a function of the following parameters, $Nu = f(Ma, Re, Pr, Tu, \Omega, T_R, \Lambda, \frac{dp}{dx_i}$, *secondary flow*). Hence, the problem is guided by compressibility, viscosity, inertial forces, shear, turbulence and other phenomena. The secondary flows also locally increase the vorticity Ω.

$$HTC = \frac{q}{(T_s - T_{ref})} \tag{3.1}$$

Typically, several regions of different heat transfer rates can be distinguished when analysing a flow over a blade Figure 3.1. Firstly, it is noted that the heat transfer magnitude is related to the size of the boundary layer and whether it is in a turbulent or laminar state. In the stagnation region, the boundary layer is the thinnest, leading to large temperature and velocity gradients [112]. The laminar-turbulent transition region is marked with an increased heat transfer. Furthermore, the separation, shock-boundary layer

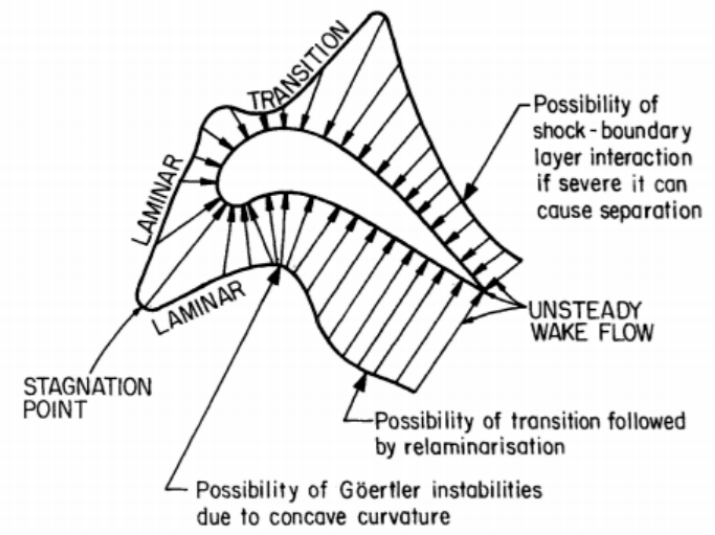

Figure 3.1: A typical distribution of relative magnitude of heat transfer rate around a turbine vane, and physical phenomena affecting it, from [10]

interaction and relaminarisation also affect the heat transfer rates.

For a given temperature difference between a wall and a fluid, an increase in heat transfer rate corresponds to an increase of HTC, and vice-versa, according to Equation 3.1. However, in general terms, the heat transfer is influenced by the aforementioned parameters, and not explicitly the HTC. The HTC is a parameter calculated from the Newton's law of cooling. The choice of the reference temperature in the HTC definition (Equation 3.1) is naturally affecting the calculated HTC value but not the recorded heat transfer rate. In literature, multiple approaches are discussed, some authors use the inlet total temperature as a reference temperature [113]. However, for compressible flows the commonly used reference temperature is the adiabatic wall temperature which is also implemented by Giel et al. [8] in their test cases.

Adiabatic wall temperature

Adiabatic wall temperature is usually chosen as a reference temperature for compressible flows. Considering an adiabatic flow, the total enthalpy h_0 is constant and given by Equation 3.2. For a calorically perfect gas (κ = constant) the Equation 3.3 holds, where $\Delta h = h_0 - h_\infty$ and $\Delta T = T_0 - T_\infty$. [58]

$$h_0 = h + \frac{u_\infty^2}{2} \tag{3.2}$$

$$\Delta h = \Delta T c_p \tag{3.3}$$

Combining these equations allows expressing the total temperature according to Equation 3.4. In high speed compressible flows, the total temperature is often related to the recovery temperature or adiabatic wall temperature, given in Equation 3.5. The dynamic part $\frac{u_\infty^2}{2}$ of Equation 3.4 describes frictional heating caused by viscous dissipation of the fluid when it is being compressed. The Equation 3.4 as an approximation for the adiabatic wall temperature is valid only for a flow with Pr = 1, meaning that the momentum boundary layer is equal to the thermal boundary layer. Otherwise, a recovery factor is implemented which accounts for the adiabatic wall heating due to dissipation. Recovery factor $r_c = Pr^{1/3}$ in a turbulent boundary layer and $r_c = Pr^{1/2}$ in a laminar boundary layer [112]. In the experiment by Giel et al.[8], the authors used $r_c = Pr^{1/3}$ in the definition of the adiabatic wall temperature.

$$T_0 = T_\infty + \frac{u_\infty^2}{2c_p} \tag{3.4}$$

$$T_{aw} = T_{\infty} + r_c \frac{u_{\infty}^2}{2c_p} \tag{3.5}$$

The adiabatic wall temperature has been shown to be representative when evaluating HTC. The concept of the adiabatic wall temperature can be visualised as shown in Figure 3.2. For compressible flows, it should be used as a reference temperature in Equation 3.1. In the experiment by Giel, the authors have used a slightly different definition of adiabatic wall temperature in the Stanton number calculations as explained in Table 4.1.1.

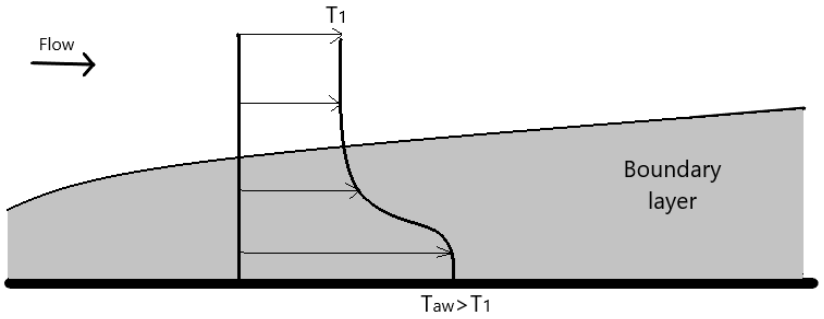

Figure 3.2: In a high speed compressible flow the fluid is stagnated on a wall, and the temperature with which the wall heat flux $q_w = 0$ is increased due to frictional heating from viscous dissipation.

Stanton number

$$St = \frac{HTC}{\rho c_p U_{ref}} \tag{3.6}$$

Another way to express a normalised convective heat transfer around a body is by means of the Stanton number. The classical definition of the Stanton number is shown in Equation 3.6. The exact definition used by Giel is written out in Table 4.1.1. The HTC and St are scaleable and proportional. The specific heat, density and reference velocity, used in the Stanton number definition, are typically taken at the freestream conditions.

3.1.2. Parameters affecting heat transfer on gas turbine nozzle guide vane

The convective heat transfer around gas turbine vane is influenced by different physics phenomena. The first stage of a high pressure turbine is susceptible to a highly turbulent flow of gas at high temperature. The main parameters affecting the heat transfer on gas turbine vanes are turbulence conditions, the state of the boundary layer and its thickness, laminar-turbulent flow transition, surface roughness, pressure gradients, thermal conductivity and viscosity of a gas. Secondary flows severely affect HTC distribution as well.

Generally, it is known that higher turbulence is tied to a stronger mixing of the flow which enhances the convective heat transfer. A highly turbulent gas coming from a combustion chamber is passing over a gas turbine nozzle guide vane, researchers have established the importance of freestream turbulence conditions for HTC evaluation on the vane. It is, typically, the most influential transition affecting parameter on a gas turbine nozzle guide vane. Higher turbulence intensity at freestream leads to an earlier transition, i.e. transition onset more upstream.Heat transfer in RANS eddy viscosity model codes is defined based on eddy viscosity (Equation 3.15 for SST $k-\omega$). The eddy viscosity is computed from turbulent kinetic energy which is affected by turbulence intensity, according to Equation 3.19. Thus, the HTC dependence on turbulence conditions is apparent not only in experiments but also implemented in numerical codes.

Pressure gradient and a possible separation impact the state of the boundary layer, thus, influencing the HTC. The curvature of a surface can have a stabilising or de-stabilising effect on the boundary layer.

The suction side of an airfoil is a convex surface having a stabilising effect on the boundary layer, and the pressure side is concave with a destabilising effect [99]. Furthermore, the wall-to-gas temperature ratio is found to affect aerodynamics and boundary layer, as investigated by Maffuli and He [114, 115]. Gas properties, such as thermal conductivity and viscosity of the gas, directly affect heat transfer and the HTC. The heat flux equation is shown in Equation 3.7. Other factors influencing transition and heat transfer are surface roughness and compressibility. A rough surface can trigger an earlier transition. Shockwaves also can cause a transition to occur [43]. Furthermore, the turbine NGVs nowadays are often, if not always, equipped with film cooling. The coolant injection often triggers transition and the boundary layer is often in a turbulent state for the greatest part of the airfoil surface.

3.1.3. Convective heat transfer implementation in *Star-CCM+*

Turbulent heat flux in *Star-CCM+* code is defined as shown in Equation 3.7 [60]. The term is implemented in the energy equation when using RANS models. Notably, eddy viscosity μ_t is proportional to the mean turbulent heat flux, thus, the measure of turbulence directly affects the heat flux. Eddy viscosity is calculated using the turbulence models as explained in Section 3.5. Therefore, various models are likely to predict differing heat flux distributions if the eddy viscosity implementation differs between them.

$$\bar{q} = -\left(\lambda + \frac{\mu_t c_p}{Pr_t}\right)\nabla\bar{T} \tag{3.7}$$

The gradient of mean temperature $\nabla\bar{T}$ drives the heat flux. Furthermore, the turbulent Prandtl number Pr_t is defined as a ratio between the diffusivity of momentum and diffusivity of heat. It usually varies between 0.7 and 0.9 [58, 116, 117]. The turbulent Prandtl number value is not specified in the Giel experiment but it is taken as 0.85 for the simulations in the present work. It is noted that specifying a constant value is a simplification since the turbulent Prandtl number varies with temperature. The specific heat c_p and thermal conductivity λ are gas properties.

3.2. Boundary layer theory

A boundary layer forms when a fluid is in motion over a solid surface. It serves as an interface between a surface and a fluid in motion, thus, having a dominant influence on heat transfer. The concepts of momentum and thermal boundary layers are addressed in this section, together with introducing momentum thickness and intermittency. In literature, the boundary layer term is often related to the momentum boundary layer. From here onwards, the ”boundary layer” term will be referred to the momentum boundary layer.

3.2.1. Momentum boundary layer

The momentum boundary layer is the block of fluid on the solid surface, in which the flow properties differ from the freestream value. For example, the velocity within the boundary layer varies between zero and a freestream value. The no-slip condition at the contact between a solid and fluid causes the velocity at a surface to be equal to zero. Wall shear and viscous effects of the fluid lead to a sheared velocity profile within a boundary layer [118].

A laminar boundary layer develops on a surface but, eventually, it transitions into a turbulent state (more on transition in Section 3.3). Due to high levels of mixing, the turbulence is diffusive, and momentum is transported more effectively in a turbulent boundary layer as compared to a laminar one. Subsequently, the velocity profile within a boundary layer is changing and the thickness of the turbulent boundary layer is larger than in a laminar one. Similarly, the skin friction is increased. The same reasoning applies to the thermal boundary layer which causes the rate of heat transfer to increase in the turbulent boundary layer as compared to a laminar boundary layer. Along the chord of a flat plate, the boundary layer thickness is increasing, hence the heat transfer coefficient is decreasing in fully laminar or fully turbulent regions due to lower temperature gradients. The variation of heat transfer coefficient for a flow over a flat plate is visualised in Figure 3.3. From such flat plate or other simple geometry experiments, researchers have developed various correlations relating Nusselt number to Reynolds and Prandtl numbers for a flow over a solid surface.

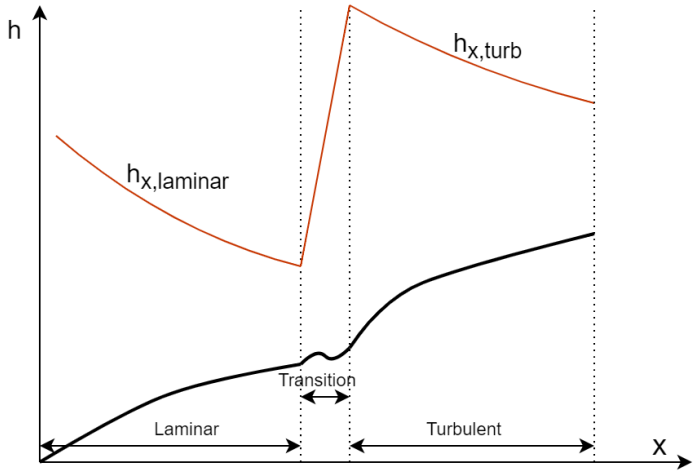

Figure 3.3: A typical convective heat transfer coefficient distribution in a flow over a flat plate

A fully turbulent boundary layer can be split in different regions with various strengths between viscous and turbulent stresses [47]. For a flow over a flat plate, the Reynolds number typically is much larger than unity, meaning that inertial forces are dominant. Right on top of a surface, there is a viscous sublayer where the fluid is in contact with the surface, and the turbulence is damped near the wall. This layer is typically very thin in practice (y^+ < 5) and the shear stress is constant and equal to the wall shear stress [47]. From this, it follows that there is a linear relationship between the mean velocity and distance from the wall. Thus, this layer is sometimes referred to as the linear sub-layer. Outside of the viscous sub-layer, the turbulent stresses are getting more dominant and the layer in the range of 30 < y^+ < 500 is denoted as log-law layer. In this region the turbulent stresses are dominant. In between the viscous sub-layer and log-law region, there is a so-called buffer layer region where turbulent and viscous stresses are of similar strength. Finally, an outer region outside the log-law region is inertia-dominated without any direct viscous effects present [47]. When developing a CFD model, it is essential to discretise the prism layer with resolution such that the viscous sub-layer can be modelled.

Momentum thickness

The flow in the boundary layer is slowed down as compared to the freestream velocity U_∞ and the velocity within the boundary layer varies with the distance from the surface, i.e. $u = u(y)$. Hence, the momentum in the boundary layer is lower as compared to a hypothetical case of a flow with invariant velocity within the boundary layer. Considering that no boundary layer is present, the deficit can be balanced by displacing the surface such that the surface is subjected to the same deficit of momentum. This concept is visualised in Figure 3.4. The momentum thickness is then defined as the distance of this displacement and calculated with Equation 3.8. Notably, as the boundary layer develops the momentum thickness is increasing. The momentum thickness concept is used in the definition of momentum thickness Reynolds number which is an essential parameter in correlations of laminar-turbulent transition.

$$\theta = \int_0^\infty \frac{u}{U_\infty}(1 - \frac{u}{U_\infty})dy \tag{3.8}$$

$$Re_\theta = \frac{\rho U \theta}{\mu} \tag{3.9}$$

Intermittency

Intermittency γ is a measure of the state of the boundary layer. It is defined as a fraction of time during which the flow is turbulent over any given point on the surface [43]. The γ = 0 for a fully laminar boundary layer, and γ = 1 for a fully turbulent boundary layer. Most transition models are based on the concept of intermittency.

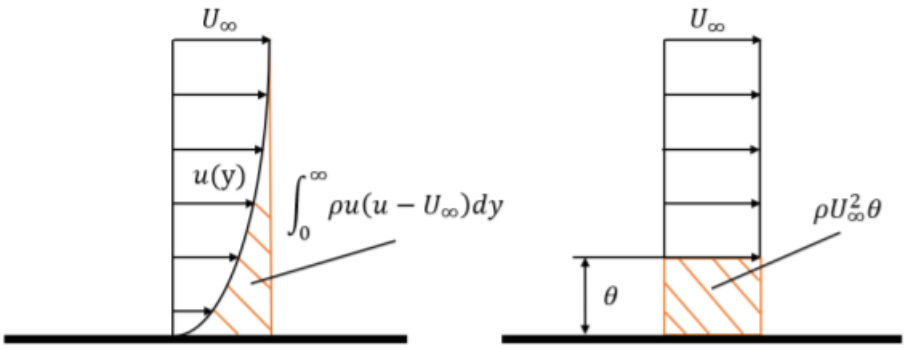

Figure 3.4: The concept of momentum thickness. The momentum thickness θ equals the height of a superficially displaced block of fluid in a boundary layer, from [58]

3.2.2. Thermal boundary layer

Considering that the fluid and the wall have different temperatures, a thermal boundary layer is forming in analogy to the momentum boundary layer [111]. The thermal boundary layer is thickening along the wall in flow direction, similar to the momentum boundary layer. For a given temperature difference between the wall and freestream, a thinner boundary layer corresponds to a higher temperature gradient dT/dy which is a reason why a higher heat transfer rate is observed for thinner boundary layers [10]. Similarly as for the momentum boundary layer, the thermal boundary layer has a varying temperature profile within it, i.e. $T = T(y)$.

In a flow over a surface with non-matching temperatures, both momentum and thermal boundary layers will develop. The diffusivity of heat and momentum determines the relation between the two boundary layers. The thermal boundary layer can be expected to be thicker than the momentum boundary layer if the diffusivity of heat is larger than the diffusivity of momentum, and vice-versa. The relation between the two boundary layers is described by a non-dimensional parameter, called Prandtl number Pr. Prandtl number is the ratio between molecular diffusivity of momentum and the molecular diffusivity of heat in a fluid [111]. Typically, the Prandtl number varies between 0.7 and 1.0 for gases, suggesting that the thermal boundary layer often is contained within the momentum boundary layer [58].

$$Pr = \frac{\mu c_p}{k} \tag{3.10}$$

3.3. Laminar-Turbulent transition

The transition of the boundary layer is of high importance in heat transfer problems. A typical convective heat transfer coefficient distribution for a flow over a flat plate is shown in Figure 3.3. A similar profile is often observed on the suction side of an airfoil, the HTC is rapidly increasing in the transition region before reaching the highest value at the end of transition when the boundary layer is turbulent. Hence, it is paramount to predict an accurate transition onset and length in order to understand how the heat transfer rates vary on the airfoil surface.

In this section, the physical transition mechanisms are discussed. The boundary layer transition to a turbulent state can be triggered in multiple ways but it starts with instabilities developing that disturb the laminar boundary layer. Two major modes of transition on a gas turbine NGV are natural and bypass transition which are discussed in more detail in this section. On a high pressure gas turbine NGV, a reverse transition from turbulent to laminar may be present as well [43]. A separation-induced transition can also occur, however, it is more common in compressors and low pressure stages of gas turbines. Moreover, for blade and vane rows downstream of NGV, a wake-induced (periodic-unsteady) transition is likely when a wake from the trailing edge impinges on the subsequent blade's surface. It must be noted, however, that the theory of transition is still not fully understood despite years of research [79] but DNS and LES simulations have revealed many details of the transition modes. On top of these transition modes, a crossflow-induced transition can occur in gas turbines as well when a crossflow causes

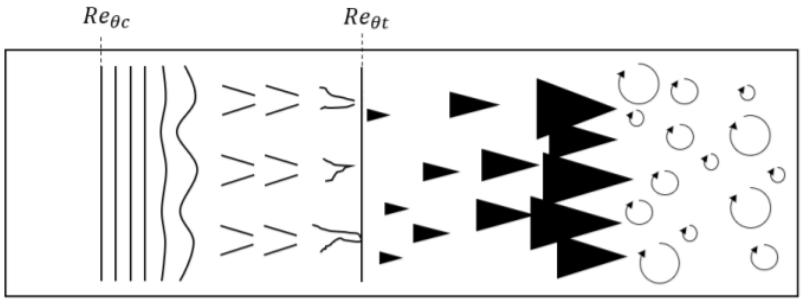

Figure 3.5: A visualisation of the natural transition process. Tollmien-Schlichting waves appear when the critical momentum thickness Reynolds number is reached. The high shear layer above hairpin vortices breaks down into turbulent spots (noted with black triangles) that eventually grow and coalesce into a single unit forming a fully turbulent boundary layer. From [58]

an instability in the boundary layer. It is the only three-dimensional transition mode that the $\gamma - Re_\theta$ transition model can account for by introducing an additional term [82], as explained further in Section 3.5.2.

Natural transition

A natural transition occurs in boundary layers that are sufficiently smooth with an undisturbed flow with low incident turbulence. Considering a flow over a flat plate, a laminar boundary layer becomes sensitive to the long wavelength disturbances causing two-dimensional Tollmien-Schlichting (T-S) waves. A visual schematic of the natural transition process is shown in Figure 3.5. The disturbances start occurring when the critical momentum thickness Reynolds number is reached. The T-S waves are the primary instabilities causing a deviation from the initially laminar boundary layer flow [101]. Subsequently, the primary instabilities grow to eventually cause a spanwise variation, forming secondary instabilities. The secondary instabilities are three-dimensional and they evolve into the hairpin vortices. The hairpin vortices impose a region of high shear above themselves that ultimately collapses and decomposes into smaller structures of chaotic motion, forming the turbulent spots [47, 58, 119] that are noted with black triangles in Figure 3.5. The turbulent spots grow larger and coalesce, eventually forming a fully turbulent boundary layer.

Bypass transition

Bypass transition is the most common transition mode in gas turbine nozzle guide vane due to the typically high freestream turbulence of the gas coming from the combustion chamber [43]. For the freestream turbulence that is sufficiently high (above 1% [79]) the initial T-S wave instabilities can be bypassed, and the flow directly collapses into turbulent spots [58]. A more theoretical approach is associated with elongated disturbances in a streamwise direction that are induced in the laminar boundary layer. These are termed streaks or Klebanoff distortions, and they are zones of forward and backward jet-like periodical perturbations. High frequency disturbances are damped by the laminar shear layer whilst the streaks are caused by deep penetration of low frequency disturbances. The dampening of high frequency disturbances is called shear-sheltering [79]. Whilst the streamwise streak patterns are of large wavelength, the instability patterns are of short wavelength. This means that even though the high frequency perturbations are damped by the boundary layer shear, they are responsible for exciting the instability patterns. The Klebanoff distortions or streaks grow in size and amplitude, eventually breaking down and forming turbulent spots. Thus, the instability mechanism of T-S waves is bypassed and the flow breakdown is considerably faster. The details of bypass transition have been obtained by DNS and LES simulations. [79]

3.4. Film cooling

Showerhead film cooling fundamentals are described in this section. Showerhead term refers to the film cooling applied to the stagnation line region at the leading edge of the NGV which is subjected to

the highest metal temperatures. Similar to the film cooling on the pressure and suction sides of the vane, the coolant is injected from the internal channels through the cooling holes to the external side of the vane surface. A film layer is developed in the high temperature environment, protecting the vane in the region of injection and downstream of the hole.

3.4.1. Flow parameters

Various parameters, such as cooling hole geometry, blowing ratio, turbulence intensity and others, influence the showerhead film cooling performance. The blowing ratio which reflects the ratio of coolant mass flow to the mainstream is defined in Equation 4.5 [5, 76]. This definition is also implemented in the present work. The blowing ratio influences the film cooling effectiveness. A too large blowing ratio can cause the coolant flow to lift off from the airfoil external surface. In such a case, the coolant stream "overshoots" the region just downstream of the hole, significantly reducing the cooling effectiveness. On the other hand, an insufficiently high blowing ratio can result in hot gas ingestion that can damage the vane and potentially cause engine failure. At the leading edge, the coolant is susceptible to separation from the surface even at low blowing ratios of around BR = 0.5 [5]. Theoretically, the reason for strong susceptibility to lift-off is the lack of crossflow at the leading edge and the main flow being decelerated as it approaches the stagnation point [120].

Film cooling around the leading edge region considerably affects aerodynamics and heat transfer on the entire airfoil surface [107]. The leading edge region typically has the highest heat transfer rates on the airfoil surface. Furthermore, this region is susceptible to high freestream turbulence and non-uniform and unsteady inflow from the combustor. The coolant at the leading edge penetrates the boundary layer causing a transition. Therefore, the boundary layer becomes turbulent downstream of the leading edge enhancing the heat transfer rates. This is a clear example of showerhead cooling influencing heat transfer on the whole surface of the airfoil. Leading edge film cooling can also be applied to rotor blades, in such case, the unsteady wakes shed by the upstream airfoil also affect the flow physics and mixing of the coolant [107].

High freestream turbulence can significantly reduce film protection [107]. The high turbulence enhances mixing and causes coolant jets to dissipate faster into the mainstream. In such a scenario, a higher blowing ratio is desired since it increases the momentum of the cooling jet, hence, the coolant dissipation into the mainstream is slowed down [107]. Furthermore, a highly turbulent mainstream flow can penetrate the protective film layer and reduce the cooling effectiveness. Chen et al. [121] experimentally investigated film cooling on a flat plate surface. The authors reported that higher freestream turbulence enhanced mixing between coolant and the mainstream, reducing the effectiveness of the cooling jets that were well-attached to the surface [121]. The enhanced flow mixing is the main detrimental factor of freestream turbulence, however, the likely coolant lift-off is of major importance for the showerhead film cooling. In the leading edge region, higher freestream turbulence promotes dispersion of the coolant back towards the vane surface [122], thus, improving the coolant coverage on the wall. Coolant coverage on the vane surface and film effectiveness are often studied by ensuring an adiabatic wall on the vane surface. Other studies have exclusively focused on heat transfer coefficient enhancement. The heat transfer downstream of the cooling hole is enhanced due to the mixing of the coolant jets with the mainstream boundary layer which produces high turbulence [107].

Goldstein and Taylor [123] summarised the heat and mass transfer effects of coolant injection through discrete holes on a flat plate. The results were obtained in terms of a local film-cooled heat transfer coefficient HTC/HTC_0 where HTC_0 corresponds to the heat transfer coefficient for an uncooled case. Several regions can be distinguished as shown in Figure 3.6. The region immediately upstream of the cooling hole (region A) is unaffected by the coolant jet. However, if the coolant momentum is sufficiently high it can push the mainstream flow back causing a flow interaction similar to a flow around a solid rod [107]. The region in-between two coolant holes is also unaffected unless the distance is low enough for two coolant jets to interact. In such case the HTC would be increased. The small region immediately downstream of the injection hole (region C) experiences the lowest HTC. A stagnation region is created underneath the jet. The blowing ratio does not affect the presence of this region [107], however, the length of low HTC region would increase if a higher BR causes coolant lift-off. The region D along the edges of the injection holes is subjected to high heat transfer rates due to large shear stresses and

eddies caused by strong mainstream interaction. The maximum HTC is typically recorded at region E in Figure 3.6 downstream of the holes. The extent of heat transfer in this region largely depends on the blowing ratio. For a low BR, the coolant stays attached to the surface and the HTC is relatively low due to a lack of strong interaction with the mainstream. As the BR increases, the region grows in length as and the HTC is increased due to enhanced mixing with the mainstream. If the lift-off of coolant is experienced due to a high BR, the region E moves downstream where the coolant jet reattaches. In case of a coolant separation, the mainstream penetrates underneath the coolant jet and it forms large eddies that further enhance the HTC downstream. Finally, region F can occur downstream of the hole at high BR due to partial reattachment of a separated coolant jet. [47]

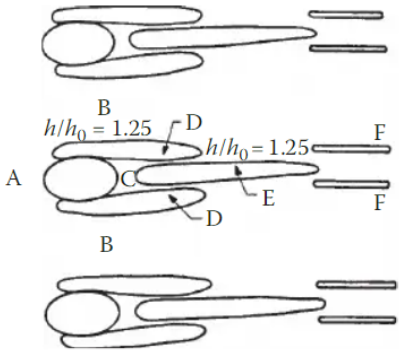

Figure 3.6: Regions of various heat/mass transfer rates around cooling holes, from Dutta et al. [107]

Evidently, the heat/mass transfer rates in film cooling are largely influenced by mixing phenomena and interaction between the coolant jet and the mainstream. The film cooling effectiveness, however, is investigated on an adiabatic surface and is strongly influenced by coolant and mainstream temperatures. The definition of film cooling effectiveness is provided in Equation 4.4.

3.4.2. Geometrical parameters

Apart from the momentum of the coolant jets and coolant temperature, the geometrical parameters largely influence film cooling performance as well. The most important parameters to consider are injection angle, the shape of a cooling channel, and the diameter or size of the holes. Injection angle β, which is defined in Figure 4.16a, plays an important role to ensure that the coolant does not lift off from the vane surface at the leading edge. In the case of showerhead film cooling, typically the coolant channels have a compound angle with respect to the mainstream direction. The cooling channels are forming 20°- 45° angle with the leading edge surface [5], and the channels are perpendicular to the mainstream flow direction.

The shape of cooling channels can be varied. A uniform-cross-section cylindrical shape is the simplest form but it is often implemented in designs. However, a fan-shaped diffusing cooling hole geometry has gained attention in research and practical designs. Chen et al. [121] compared both shapes and concluded that simple-angled fan-shaped holes provided better coolant coverage than the cylindrical holes for a flat plate film cooling. At higher blowing ratios fan-shaped holes are less susceptible to coolant liftoff. An apparent disadvantage of fan-shaped cooling holes as compared to the cylindrical holes is the ease of manufacturing. Furthermore, adding a compound angle increased the coolant coverage, especially for the cylindrical holes [121]. The addition of a compound angle provides stronger resistance against the coolant liftoff at high blowing ratios [124]. The pitch between the cooling holes affects the performance, and the distance between separate cooling rows is to be considered as well. The pitch between holes determines whether two coolant jets mix together in case the distance between them is sufficiently small.

3.5. Computational fluid dynamics

A brief introduction to CFD modelling is given with a focus on RANS solvers and turbulence modelling. The turbulence models used in the thesis and the theory of turbulence modelling are described in Section 3.5.1. Transition modelling and a thorough description of the $\gamma - Re_\theta$ model are in Section 3.5.2. A brief summary of the CFD basic theory is provided, and the reader is guided to [47] for a more complete review of the general CFD theory.

Computational fluid dynamics is a tool to numerically solve partial differential equations for governing physics of fluid flow. The equations are derived from fundamental laws of physics: the conservation of mass, conservation of energy and conservation of momentum. These laws are described in continuity equation, energy equation and momentum equations, respectively. An equation of state is required to close the set of equations for a compressible flow involving heat transfer. The equations of state relate density and internal energy to temperature and pressure, and they describe the thermodynamic properties of the fluid. [47, 58]

Navier-Stokes equations are typically used to describe the conservation of momentum. By applying the concept of Reynolds averaging, the flow quantities are decomposed into the mean and fluctuating components. Reynolds averaging of flow quantities introduces the unclosed Reynolds stress term. This term is the Reynolds stress tensor $\tau_{ij} = \rho\overline{u_i' u_j'}$ consisting of the so-called Reynolds stresses, and turbulence models are introduced to provide a solution to the closure problem. Generally, the time-averaged value of the Reynolds stress tensor can be expressed with Equation 3.11 [125]. However, the individual constituents of this equation also have unknown parameters that should be modelled.

$$\frac{\partial(\overline{u_i' u_j'})}{\partial t} + \underbrace{K_{ij}}_{advection} = \underbrace{P_{ij}}_{production} + \underbrace{T_{ij} + D_{ij}^{v} + D_{ij}^{p}}_{diffusion} + \underbrace{\Phi_{ij}}_{pressure\ strain} + \underbrace{\varepsilon_{ij}}_{dissipation} \tag{3.11}$$

Multiple terms in Equation 3.11 involve advection, production with an inclusion of a source term and an increase of turbulence intensity by energy transfer from the mean flow, turbulent diffusion, viscous diffusion, pressure diffusion, pressure strain correlation and dissipation. Turbulence models are introduced to close the set of equations by modelling the unclosed terms. This can be done by introducing additional transport equations. Prandtl mixing model requires no extra equations, multiple other eddy viscosity models require, typically, one or two, and finally the Reynolds stress models have seven transport equations solving for all Reynolds stresses [47].

3.5.1. Turbulence modelling

First, the concept of energy cascade is presented before addressing the turbulence modelling in CFD. In the flow field, the turbulent structures have various sizes or scales. The largest turbulence eddies are capable of interacting with the mean flow and they extract energy from it. This process is called vortex stretching. Angular momentum is conserved during vortex stretching, and the largest eddies are effectively inviscid [47]. The largest (integral) scales are also the most energetic and responsible for generating turbulence energy, which is then transferred to the medium-small scale vortices and dissipated in micro or sub-micro scales vortices [125]. This process is often labeled as the energy cascade and it is helpful for understanding how turbulence energy is produced and how the integral length scale affects the turbulence modelling. The smallest scales are called Kolmogorov microscales. The energy associated with the smallest scales is dissipated and converted into thermal energy [47]. For a direct numerical solution, it is required to implement a spatial computational grid that is able to resolve the Kolmogorov scales. LES can resolve the largest turbulent scales but RANS methods model all turbulent scales requiring a turbulence model.

Eddy viscosity models, such as $k - \omega$ or $k - \varepsilon$, form a class of turbulence models that are based on Boussinesq hypothesis. The experimental evidence has shown that turbulence decays unless there is shear in isothermal incompressible flows [47]. The turbulence causes fluid elements to exchange momentum, and turbulent stresses increase as the mean rate of deformation increases. These observations in experiments led to the Boussinesq hypothesis which is the basis of all eddy-viscosity turbulence models. In 1877, Boussinesq proposed that Reynolds stresses are proportional to the mean strain rate,

leading to Equation 3.12 [47].

$$\tau_{ij} = -\rho\overline{u_i' u_j'} = \mu_t \left(\frac{\partial U_i}{\partial x_j} + \frac{\partial U_j}{\partial x_i} \right) - \frac{2}{3}\rho k \delta_{ij} \tag{3.12}$$

The first term of the right-hand side of Equation 3.12 is analogous to viscous shear stress expression involving the strain rate term. However, the term is multiplied by the turbulent or eddy viscosity μ_t instead of dynamic viscosity. Hence, the eddy viscosity models are based on the so-called Reynolds stress analogy which is a presumption that there exists an analogy between Reynolds stresses and viscous stresses on the mean flow. The parameter k is turbulent kinetic energy per unit mass, and δ_{ij} is Kronecker delta (δ_{ij} = 1 if $i = j$ and δ_{ij} = 0 otherwise) [47]. The concept of turbulent eddy viscosity is the basis of all eddy viscosity models, such as $k-\omega$, $k-\varepsilon$ and others.

It is noted that eddy viscosity models imply an assumption of isotropic turbulence since all normal stress components have an equal contribution of $1/3$ in the three dimensional flow field. This assumption, however, is often invalid, especially in complex flows [47]. Often the most energetic largest eddies are anisotropic. Reynolds stress models (RSM) are designed to solve for all Reynolds stresses but they have an increased computational cost. In order to account for anisotropy with eddy viscosity models, they are often extended with additional parameters or constitutive relations. The lag elliptic blending $k-\epsilon$ model, for example, includes an additional transport equation for the "anisotropy measure" ϕ. Another set of models aiming to replicate the performance of RSM with reduced cost are the algebraic stress models. These models reduce the partial differential equations describing Reynolds stresses to algebraic equations to be solved alongside k and ε transport equations in the $k-\varepsilon$ model [47].

Turbulence models are required for RANS solvers. $\overline{v^2}-f$, SST $k-\omega$, lag EB and realizable $k-\varepsilon$ (RKE) models are described in greater detail in the following sections after they were found to be promising in the literature for heat transfer problems, with the RKE model being specifically introduced for improved performance in film cooling effectiveness predictions.

The SST $k-\omega$ model

The SST $k-\omega$ model, proposed by Menter [50], is one of the most widely used turbulence model for different flow cases in CFD. The model is applicable to flows with separation and adverse pressure gradients, making it appealing for both turbomachinery and external aerodynamics flow simulations. The SST model extends the classical two-equation $k-\omega$ by implementing the Durbin's realisability constraint to limit the turbulent kinetic energy production at stagnation. Furthermore, the model definition allows to treat regions near the wall and far away from it separately with an inclusion of a blending region. This is one of the main advantages of the SST model that increases the accuracy of flow field prediction [52]. As discussed in Chapter 2, the model has been used extensively in HTC predictions in turbomachinery, and it can be coupled with a transition model.
Two transport equations are solved for turbulent kinetic energy k (Equation 3.13) and specific dissipation rate ω (Equation 3.14). The equations are written without source terms, and P and D are production and dissipation terms, respectively.

$$\frac{\partial}{\partial t}(\rho k) + \nabla \cdot (\rho k \bar{\boldsymbol{u}}) = \nabla \cdot [(\mu + \sigma_k \mu_t)\nabla k] + P_k - D_k \tag{3.13}$$

$$\frac{\partial}{\partial t}(\rho \omega) + \nabla \cdot (\rho \omega \bar{\boldsymbol{u}}) = \nabla \cdot [(\mu + \sigma_\omega \mu_t)\nabla k] + P_\omega - D_\omega \tag{3.14}$$

The eddy viscosity μ_t is calculated with Durbin's realizability constraint preventing the unrealistic growth of k in the stagnation region [51].

$$\mu_t = \rho k \; \mathit{min}\left(\frac{1}{\mathit{max}(\omega/\alpha^*, (SF_2)/a_1)}, \frac{C_T}{\sqrt{3}S} \right) \tag{3.15}$$

Non-linear constitutive relations and curvature correction for the SST model

Non-linear constitutive relations introduce non-linear functions of the strain and vorticity tensors with an aim to account for anisotropy of turbulence. Quadratic and cubic relations are included in the *Star-CCM+* software package. The cubic relation is derived from Reynolds stress transport model, hence it represents an Explicit Algebraic Reynolds Stress Model (EARSM) [60]. The RSMs perform better than eddy viscosity models in anisotropic turbulence but, apart from demanding more computational resources, can be unstable in complex flows. The cubic relation can serve as a compromise between these factors, allowing for the eddy viscosity based SST $k-\omega$ model to better account for anisotropic turbulence. The detailed formulation is provided in the *Star-CCM+* user guide [60].
When implementing the cubic relation, Equation 3.16 is used for eddy viscosity calculation, instead of the original equation implemented in the SST $k-\omega$ model (Equation 3.15). Coefficients C_μ and β^* are model coefficients and they are calculated involving the information about the strain rate tensor, full equations in [60].

$$\mu_t = \frac{C_\mu}{\beta^*}\frac{\rho k}{\omega} \tag{3.16}$$

The SST $k-\omega$ model can also be equipped with the curvature correction. The turbulent kinetic energy transport equation is typically insensitive to stabilising and destabilising effects associated with strong (streamline) curvature and frame-rotation. Curvature correction provides an option to incorporate correction factors for these parameters, this way altering turbulent kinetic energy production according to the local rotation and vorticity rates [60]. Smirnov & Levechya implemented the curvature correction factor for the SST model in RANS simulations when investigating horseshoe vortex modelling [126]. The authors reported that the implementation of the curvature factor resulted in a more complex horseshoe vortex system and endwall local heat transfer patterns upstream of the leading edge of an airfoil. The main reason was argued to be a considerable reduction of eddy viscosity produced inside the vortex cores as compared to simulations without the inclusion of the curvature correction.[126]

Implementation of turbulent length scale

Implementation of turbulence length scale is discussed as the HTC results are often sensitive to the specified length scale. The length scale measured in experiments and the implementation in RANS CFD codes often differs [12]. In CFD codes the turbulent length scale is computed from turbulence kinetic energy which is connected to turbulence intensity and the local velocity magnitude through Equation 3.19. Equation 3.17 shows the equation for $k-\omega$ based models, and Equation 3.18 for $k-\varepsilon$ based models with the corresponding model coefficient values of β^* and C_μ.

$$\Lambda_t = \frac{k^{1/2}}{\omega\beta^{*1/4}} \tag{3.17}$$

$$\Lambda_t = \frac{C_\mu^{3/4}k^{3/2}}{\varepsilon} = \frac{0.164k^{3/2}}{\varepsilon} \tag{3.18}$$

$$k = \frac{3}{2}(TuU)^2 \tag{3.19}$$

In an experimental setup, the measured length scale commonly replicates the size of the largest eddies in the flow field. It is denoted as the integral length scale Λ_I. In the test case by Giel et al. [8], it is measured with hot-wire probes. The energy scale Λ_k is representative of the average of energy-carrying eddies defined in the freestream and can be calculated with Equation 3.20 [12]. This serves as an approximation of the experimentally obtained integral length scale measurement.

$$\Lambda_k = \frac{1.5(2/3k)^{3/2}}{\varepsilon} = \frac{0.8165k^{3/2}}{\varepsilon} \tag{3.20}$$

It is noted from Equation 3.18 and Equation 3.20 that the length scale Λ_t in CFD RANS implementation is about $1/5$ of the Λ_k which is an estimate of the integral length scale. Considering that Giel reported $29.2mm$ length scale in the experiment [8], the turbulent length scale specified in the CFD code would

be $\Lambda_t = 6mm$. A similar analysis applies to the $k-\omega$ models.

Lag-elliptic blending $k-\varepsilon$ model

The lag elliptic blending model (lag EB) is an extension of the classical blending model, proposed by Lardeau and Billard [64]. The introduced "lag" term accounts for misalignment between strain and stress tensors. Similar to the classical blending model, the lag EB model has a transport equation for the blending factor, α. Additionally, another transport equation is implemented for the scalar measure of anisotropy, or "reduced stress function". It is defined as $\phi = \bar{v^2}/k$ which can be labeled as a lag effect on the eddy viscosity. The derivation of ϕ stems directly from elliptic-blending RSM, i.e. it uses the same assumptions as the derivation for the lag model [64]. The derivation of the lag model stems from the premise that often the turbulence kinetic energy production is overestimated in the regions where the anisotropy tensor and strain tensor are not aligned. An example of such a case is when a vortex is shed from a trailing edge of an airfoil. The lag EB model aims to introduce a method to account for such misalignment between stress and strain tensors. [64]

The considered lag elliptic blending model is based on $k-\varepsilon$. The model implements four transport equations. Two transport equations are for turbulence kinetic energy k and dissipation rate ε which are similar to the SST model but ω equation is replaced with the ε equation. Two additional transport equations are given in Equation 3.21 and Equation 3.22 without source terms. The blending parameter α has a value of 0 on a surface and 1 in a freestream. The reduced stress function is defined in such a way that the value of ϕ is required to be provided at the inlet, and $\phi = 2/3$ in the freestream where the turbulence is isotropic [53, 58].

$$\frac{\partial}{\partial t}(\rho\phi) + \nabla\cdot(\rho\phi\bar{\boldsymbol{u}}) = \nabla\cdot\left[(\frac{\mu}{2} + \frac{\mu_t}{\sigma_\phi})\nabla\phi\right] + P_\phi \tag{3.21}$$

$$\nabla\cdot(\Lambda^2\nabla\alpha) = \alpha - 1 \tag{3.22}$$

$$\mu_t = \rho C_\mu \phi k \; \textit{min}\left(t, \frac{C_T}{\sqrt{3}C_\mu\phi S}\right) \tag{3.23}$$

Eddy viscosity is calculated as described in Equation 3.23 with the anisotropy measure implemented, and parameter t is the turbulent time scale [60]. The production and dissipation terms are calculated similarly as for the $k-\varepsilon$ based $\overline{v^2}-f$ model, with the addition of production term for the measure of turbulence anisotropy ϕ. The formulation of this production term, P_ϕ, is deemed to improve the numerical robustness by implementing different formulations close to walls and in freestream, as compared to a single elliptic relaxation parameter f [53]. The inclusion of the Reynolds stress anisotropy tensor, the near-wall turbulence damping function and the vorticity tensor enables the lag EB model to achieve high performance in modelling separation and reattachment, vortex shedding, rotation and curvature effects.

The length scale implementation for lag elliptic blending $k-\varepsilon$ model slightly differs from the classical $k-\varepsilon$ implementation. The equation for the length scale is given in Equation 3.24. The first term is identical to Equation 3.18, however, an additional term consisting of kinematic viscosity is added.

$$\Lambda = C_L\sqrt{\frac{k^3}{\varepsilon^2} + C_\eta^2\sqrt{\frac{\nu^3}{\varepsilon}}} \tag{3.24}$$

$\overline{v^2}-f$ model

The $\overline{v^2}-f$ model implements additional transport equations for the wall-normal stress and elliptic relaxation parameter f to extend the classical $k-\varepsilon$ model. The wall-normal stress component of the Reynolds stress tensor is described by the velocity fluctuation normal-to-wall term $\bar{v^2}$ [59]. Hence, four transport equations are implemented for k, ε, v^2 and f. Evolution of eddy viscosity is calculated from the velocity scale v^2. The model formulation is similar to the EB $k-\varepsilon$ model without the lag term. However, the $\overline{v^2}-f$ is an older model than EB $k-\varepsilon$.

Realizable $k-\varepsilon$ model

The realizable $k-\varepsilon$ model is promising in film cooling problems as described in the literature review in Section 2.3, hence, it is implemented to investigate the showerhead cooling effectiveness. As compared to the original two-equation $k-\varepsilon$ model, the realizable $k-\varepsilon$ contains a new transport equation for the turbulent dissipation rate ε, and a critical model coefficient C_μ is expressed as a function of mean flow and turbulence properties instead of being constant [60]. These modifications allow the model to satisfy mathematical constraints on normal stresses that are consistent with the physics of turbulence. The model coefficient C_μ being variable agrees with the experimental observations, and the coefficient is included in the eddy viscosity computations. The "two-layer" approach is implemented which allows an all-y^+ wall treatment. However, it is noted that the elliptic blending and lag elliptic blending $k-\varepsilon$ models are expected to improve the accuracy in the near-wall region. [60]

Hybrid RANS-LES models

Hybrid RANS-LES formulations have been developed to resolve some of the turbulent scales with a considerably reduced computational cost as compared to LES methods. Detached eddy simulation (DES) is one of such developments. Stress blended eddy simulation (SBES) was introduced more recently by Menter [36]. SBES formulation improves shielding of RANS zones and achieves a more rapid RANS-LES 'transition'. SBES model has been implemented in the $ANSYS$ software package, the Scale-resolving hybrid (SRH) model has been implemented in the *Star-CCM+* software package. The SRH model implements unsteady RANS and LES interchangeably. The model applies spatial-temporal filtering and allows RANS formulation to switch to LES in the regions where spatial and temporal resolution are sufficient [60]. Hybrid models are computationally more expensive than full-scale Reynolds Stress models, and they imply the use of transient simulations.

An initial solution must be provided for a transient simulation. This is often done by providing a steady-state RANS solution. An implicit solver is implemented in the current study with the second order temporal discretisation. Convective Courant-Friedrich-Lewy (CFL) number is an important parameter to consider for transient simulations. The CFL number is dictated by the temporal and spatial resolution as shown in Equation 3.25. The CFL in the regions of interest should be below unity to capture transient behaviour. A mean CFL number or a specific range of between minimum and maximum CFL values can be imposed when implementing adaptive time-stepping.

$$CFL = \Delta t \frac{\Delta x}{U} \tag{3.25}$$

Scale resolving models need to be equipped with a realistic inflow condition. As opposed to specifying turbulence intensity as it is done for the statistical RANS models, an inflow profile needs to be provided to ensure a flow with realistic turbulence characteristics. Mathematical methods have also been developed to achieve realistic turbulence characteristics at the inflow. Superimposing Gaussian noise to the mean velocity field is one of the simplest approaches. Anisotropic linear forcing (ALF) can be applied at the control volume in the inlet region. ALF extracts turbulence characteristics from a RANS simulation. Then the turbulence kinetic energy, dissipation rate, and velocity components are applied to a forcing volume in scale resolving simulation to replicate the statistical turbulence levels of RANS simulation. [60]

3.5.2. Transition modelling

Some turbulence models, including $\overline{v^2}-f$, attempt transition modelling, others are coupled with specific transition models. The $\gamma - Re_\theta$ transition model is described in greater detail in this section. It is a common practice to implement the SST $k-\omega$ turbulence model in conjunction with this transition model.

The $\gamma - Re_\theta$ model description

The $\gamma - Re_\theta$ transition model is applied for flows in which the boundary layer is laminar for a significant portion of an airfoil. It is a two-equation model, consisting of transport equations for intermittency γ (Equation 3.26) and transition momentum thickness Reynolds number Re_θ (Equation 3.27). The $\gamma - Re_\theta$

model evaluates the local flow features to account for natural, bypass and separation induced transition modes, as well as wake-induced and reverse transition [82]. The model controls transition length and transition onset by implementing correlations based on experimental data obtained on reference geometries.

$$\frac{\partial(\rho\gamma)}{\partial t} + \nabla \cdot (\rho \mathbf{U}\gamma) = \nabla \cdot \left[(\mu + \frac{\mu_t}{\sigma_f})\nabla\gamma\right] + P_\gamma - E_\gamma \tag{3.26}$$

$$\frac{\partial(\rho\overline{Re_{\theta,tr}})}{\partial t} + \nabla \cdot (\rho \mathbf{U}\overline{Re_{\theta,tr}}) = \nabla \cdot \left[\sigma_{\theta,tr}(\mu + \mu_t)\nabla\overline{Re_{\theta,tr}}\right] + P_{\theta,tr} + D_{SCF} \tag{3.27}$$

The D_{SCF} is a crossflow-induced transition term that can be either enabled or disabled in *Star-CCM+* implementation. Production terms P_γ and $P_{\theta,tr}$ are written out in the equations below. The formulation of equations is such that $\gamma = 0$ in the fully laminar boundary layer and it allows for relaminarisation to be predicted. In the viscous sublayer and outside of the boundary layer the destruction term is disabled such that the freestream value of intermittency is equal to one ($\gamma = 1$). [60]. The attention is guided towards the implementation of two variables which are obtained from experimental correlations, F_{length} and $Re_{\theta,tr}$.

$$P_\gamma = F_{length} C_{a1} \rho S [\gamma F_{onset}]^{0.5} (1 - C_{e1}\gamma) \tag{3.28}$$

$$P_{\theta,tr} = C_{\theta,tr} \frac{\rho^2 U^2}{500\mu} (Re_{\theta,tr} - \overline{Re_{\theta,tr}})(1 - F_{\theta,tr}) \tag{3.29}$$

The value of $\overline{Re_{\theta,tr}}$ is calculated at every cell via the transport equation. Similarly, the intermittency γ is computed at every cell as well, meaning that the $\gamma - Re_\theta$ model has a local treatment of the flow quantities. Then the value of $\overline{Re_{\theta,tr}}$ is used to find F_{length} and the critical momentum thickness Reynolds number $Re_{\theta,cr}$ based on experimentally found correlations. The variable F_{length} controls the length of transition, and the $Re_{\theta,cr}$ the location of the transition. As shown in Equation 3.28, the variable F_{length} controls the strength of the production term in the intermittency transport equation. This means that a higher F_{length} results in a shorter transition length since the production of γ is increased, and $\gamma = 1$ corresponds to a turbulent boundary layer. The $Re_{\theta,cr}$ is the momentum thickness Reynolds number at which the intermittency starts to increase, it is based on experimental correlations performed often on flat plates. The F_{onset} in Equation 3.28 serves as a switch that triggers the production of intermittency in the location where the transition occurs. It is noted that $Re_{\theta,tr}$ is not the same variable as $\overline{Re_{\theta,tr}}$. The $\overline{Re_{\theta,tr}}$ is computed via the transport equation and its value is specified at freestream. This freestream value is then diffused into the boundary layer with the production term controlling the strength of this process [77]. The $Re_{\theta,tr}$ is a single value containing the information at which Re_θ the transition occurs. As explained in Section 3.2.1, the Re_θ increases along the streamwise direction of flow over a flat plate, then at a specific location $Re_\theta = Re_{\theta,tr}$ when the transition occurs.

Experimental correlations for $\gamma - Re_\theta$ model

Experimental correlations are applied to find $Re_{\theta,tr}$, $Re_{\theta,cr}$ and F_{length}. Amongst the most popular correlations for $Re_{\theta,tr}$ is the non-zero pressure gradient correlation by Menter et al. [77]. Alternatively, Langtry [127] developed a zero-pressure gradient correlation depending on turbulence intensity (Equation 3.30). The correlation by Langtry is also implemented in Suluksna-Juntasaro calibration, included in the *Star-CCM+* software package [60].

$$Re_{\theta,tr} = \begin{cases} (1173.51 - 589.428Tu + 0.2196/Tu^2); & Tu \leq 1.3 \\ 331.5(Tu - 0.5658)^{-0.671}; & Tu > 1.3 \end{cases} \tag{3.30}$$

U[stream of the transition location, the instabilities in the boundary layer start occurring due to the production of intermittency. The location where the intermittency starts to increase is marked by the critical momentum thickness Reynolds number $Re_{\theta,cr}$. Notably, the value of $Re_{\theta,cr}$ is lower than $Re_{\theta,tr}$. The relation between $Re_{\theta,cr}$ and $Re_{\theta,tr}$ is determined via experimentally obtained correlations.

$$Re_{\theta,cr} = func(\overline{Re_{\theta,tr}}) \tag{3.31}$$

The experimental correlations for $Re_{\theta,tr}$ or transition onset are based on the values in freestream. Hence, the $Re_{\theta,tr}$ cannot be applied locally to each cell in the computational domain. Therefore, the transport equation for $\overline{Re_{\theta,tr}}$ is introduced. The transport equation (Equation 3.27) is constructed such that the freestream value is convected and diffused into the boundary layer [77]. Then, by using the correlation, local values of $Re_{\theta,cr}$ and F_{length} are computed from $\overline{Re_{\theta,tr}}$. Due to $\overline{Re_{\theta,tr}}$ being calculated locally by using the information of the freestream conditions, the edge between freestream and the boundary layer needs to be defined. In *Star-CCM+* this is defined as "freestream edge" [60]. Suluksna et al. defined it as $y = 2\delta(x)$, where $\delta(x)$ is the size of the boundary layer at location x along the chord [85].

To close the model, two additional correlations for $Re_{\theta,cr}$ and F_{length} are obtained to find the local values which depend on the locally computed $\overline{Re_{\theta}}$. The correlation implemented in *Star-CCM+* as a default option is the Suluksna-Juntasaro correlation [85], which uses Equation 3.32 for $Re_{\theta,cr}$ and Equation 3.33 for F_{length} correlations.

$$Re_{\theta,cr} = \textit{min}\left[0.615\overline{Re_{\theta,tr}} + 61.5, \overline{Re_{\theta,tr}}\right] \tag{3.32}$$

$$F_{length} = \textit{min}\left[0.5 + exp(7.168 - 0.01173\overline{Re_{\theta,tr}}), 300\right] \tag{3.33}$$

Suluksna - Juntasaro correlations are based on the zero-pressure gradient $Re_{\theta,tr}$ correlation (Equation 3.30), aimed to improve the results at lower free-stream turbulence intensities. Suluksna et al. [85] performed correlations on various test cases with turbulence intensity ranging from 1% to 7% and better agreement with experimental data was reached on cases with 1%-4% turbulence intensities. The authors stated that the correlation is applicable for flow cases with low and medium turbulence intensities.

The correlations for $Re_{\theta,cr}$ and F_{length} are obtained from experiments on a flat plate, and there are many more correlations made by other authors. Some of these, for example, are published by Sorensen [128], Elsner [129] and Kelterer [130], all of whom implemented the Menter's non-zero pressure gradient $Re_{\theta,tr}$ correlation [77]. Kelterer at al. [130] stated that the performance of the $\gamma - Re_{\theta}$ transition model greatly depends on the correlations implemented and the solver. It is noted that both $Re_{\theta,cr}$ and F_{length} correlations are functions of $\overline{Re_{\theta}}$ [77]. Therefore, the $Re_{\theta,cr}$ and F_{length} correlations cannot be applied to an arbitrary $Re_{\theta,tr}$ correlation but they should be applied to $Re_{\theta,tr}$ correlation with which they were derived.

Kelterer et al. [130] compared various other correlations and derived new correlations themselves. The derived correlations are provided in Equation 3.34 and Equation 3.35 for $Re_{\theta,cr}$ and F_{length}, respectively. The Kelterer correlation is included in the method of the current work, and for detailed expression of Sorensen and Elsner correlations the reader is guided to the original paper by Kelterer et al. [130].

$$Re_{\theta,cr} = \begin{Bmatrix} 1.02 \cdot \overline{Re_{\theta,tr}} - 35 + tanh\left[-\left(\frac{\overline{Re_{\theta,tr}}-138}{54}\right)\right] \cdot 36; & \overline{Re_{\theta,tr}} \leqslant 215 \\ tanh\left[-\left(\frac{\overline{Re_{\theta,tr}}-215}{15}\right)\right] \cdot 45 + 155; & \overline{Re_{\theta,tr}} > 215 \end{Bmatrix} \tag{3.34}$$

$$F_{length} = \textit{min}\left[250 \cdot exp(-\left(\frac{\overline{Re_{\theta,tr}}}{130}\right)^{1.7}) + 10; 40\right] \tag{3.35}$$

Final remarks on $\gamma - Re_{\theta}$ model

The y^+ value should be below one everywhere along the surface when implementing the $\gamma - Re_{\theta}$ transition model, a fine streamwise resolution is required as well [60]. The transition model is to be implemented when a significant portion of the airfoil surface is under a laminar flow. In gas turbine NGV, the incoming flow is typically highly turbulent. In such a case, it is not needed to implement the transition model simply because the boundary layer would mostly not be in the laminar state. Alternatively, a coolant often triggers transition at the leading edge such that the boundary layer is turbulent.

4

Methodology

The methodology section is split into two parts corresponding to two separate analyses. First, the validation case is described where an experimental case of a linear cascade of blades is replicated in a CFD model. The calculated HTC results are compared to the experimental data to validate CFD methodology and various turbulence models. Following that, a CFD model of nozzle guide vane equipped with showerhead film cooling is presented. For this flow case, the adiabatic cooling effectiveness is investigated, and the effect of a swirling inflow is analysed. However, the obtained results are not compared to experimental data. In both flow cases, a hybrid RANS-LES simulation is attempted after presenting steady-state RANS results.

4.1. Validation case

An experimental case from Giel [8] is recreated in a CFD model to validate the CFD methodology and turbulence models. The focus is put on evaluating the interaction between the endwalls and the vane. The heat transfer is calculated on the whole surface of the vane, including the regions close to endwalls.

4.1.1. Giel test case description

Experimental case by Giel et al. [8] is described in this section. A linear cascade of blades placed on a wall is subjected to airflow at sea level conditions. The authors performed a series of experiments but the particular experiment was conducted to investigate secondary flow influence on blade heat transfer, together with effects of laminar-turbulent transition, shock and turbulence characteristics. The temperature data was obtained on the airfoil surface, and the Stanton number was then calculated based on the temperature. The recorded Stanton number data will be compared to the results obtained with CFD simulations.

The experimental setup is shown in Figure 4.1a. A cascade of blades is subjected to flow at sea level conditions, the inflow angle is 63.6°. Cylindrical electrical cartridge heaters were placed under the surface of blades along the whole span of the blades. An optional turbulence grid is located upstream of the cascade to generate turbulence. Hence, there are flow cases with a high turbulence intensity at the inlet (around 8%) when the grid is placed, and low turbulence intensity (around 0.5%) when removed. [8]
In total, there were eight separate flow cases tested as shown in Table 4.2. They are labelled as Case A to Case H in this document from here onwards. The inlet Mach number was kept fixed at Ma_{in} = 0.38 for all cases, but the outlet Mach number was either Ma_{out} = 1.32 or Ma_{out} = 0.98 depending on the pressure set at the exhaust. Low Reynolds number and high Reynolds number cases were tested, where an ambient temperature air was throttled at 0.5 bar inlet total pressure for the former and 1.0 bar for the latter. The high Reynolds number cases had Re_x = 1.0 $\times$ 10^6 at the inlet and Re_x = 1.8 $\times$ 10^6 at outlet, the low Reynolds number cases had Re_x = 0.5 $\times$ 10^6 at the inlet and Re_x = 0.9 $\times$ 10^6 at outlet. The Reynolds number in the current work is evaluated using the axial chord, denoted with the subscript x. The exit Mach number was controlled by means of a valve between the test section and exhaust header. Finally, the boundary layer width was estimated to be around 2.0 cm when the grid

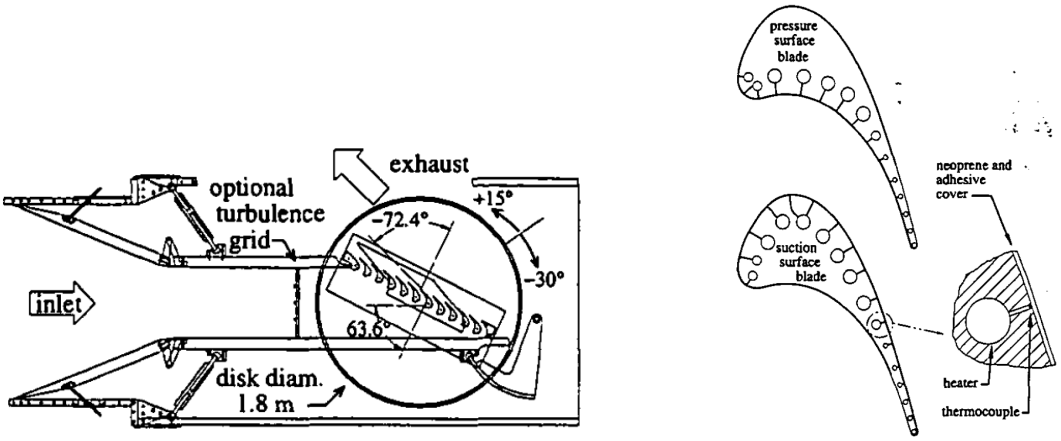

(a) The experimental setup.

(b) Heaters and thermocouples placed under the blade surface.

Figure 4.1: Experimental and measurement setup, from Giel et al. [8].

for turbulence generation was installed, and 3.2 cm when removed. Geometric properties of the blade and the described boundary conditions are summarised in Table 4.1.

Table 4.1: Geometric and flow properties of the experimental case as described by Giel et al. [8]

Geometric property	Value
Axial chord	12.7 cm
Blade Span	15.24 cm
Blade pitch	13.0 cm
True chord	18.42 cm
Flow property	
Inlet Reynolds number $Re_{x,in}$	0.5×10^6 or 1.0×10^6
Outlet Reynolds number $Re_{x,out}$	0.9×10^6 or 1.8×10^6
Inlet Mach number $Ma_{is,in}$	0.38
Outlet Mach number $Ma_{is,out}$	0.98 or 1.32
Inlet flow angle	63.6°
Endwall boundary layer width at the inlet (with turbulence grid)	2 cm
Endwall boundary layer width at the inlet (no turbulence grid)	3.2 cm

Heat flux rates were obtained from a calibrated resistance layer, together with temperature measurements by calibrated liquid crystals. Metal blades were manufactured of high conductivity copper and consisted of a low conductivity composite layer over which the heat transfer was measured. The layer consists of adhesive film and neoprene rubber [8]. Liquid crystals were sprayed on the surface. The composite layer conductance was calibrated in a separate test with an uncertainty margin of $\pm$5% and did not vary significantly over the various test cases with a wide range of heat fluxes. A separate blade set which was equipped with static pressure taps was used for static pressure measurements. More details of the experimental setup are available in the original paper by Giel et al. [8].

Hot wire measurements were incorporated to measure the turbulence intensity and length scale. A density-velocity product in the freestream was calibrated to the wire output voltage to compensate for the fact that the pressure in the rig was below the atmospheric pressure. Data were recorded at a sampling frequency of 76.2 kHz, and just above 1×10^6 data points were recorded for each length scale. The lowest distinguishable frequency was found to be 2.3 Hz. The resulting autocorrelations were fit to the exponential curve in form of $funct(t) = exp(-Ct)$, and the length scale was then computed as U_{avg}/C. [8]

Observations by the authors of the experiment

Three variables distinguish the test cases from each other – Reynolds number, Mach number at exit and the installation of turbulence grid. The authors observed that the grid causes a significantly earlier transition since the flow has high turbulence intensity at the inflow.

The cases without a turbulence grid installed lead to more pronounced secondary flow effects due to thicker boundary layers on endwalls at the inlet. However, a reduction by $1/3$ to $1/2$ of the measured Stanton numbers was recorded away from endwalls. These findings agree with the expectations. Secondary flows enhanced the heat transfer on the suction side of the airfoil since the relatively cool secondary flow fluid was impinging on the airfoil surface which was heated. Vortices lifted off from the endwall surface and, eventually, exited the cascade at a spanwise location of around 25% of the span. The authors state that the induced freestream turbulence from the secondary flow field was sufficient to ”trip” the flow near endwalls, this way preventing separation. [8]

The exit Mach number (either 1.33 or 0.98) determined whether a shock was present, or not. The oblique shock was observed at the trailing edge of the blade, and it impinged on the suction side of the adjacent blade. In heat transfer data the shocks are observed, since the shock impingement caused thickening of the boundary layer, thus, reducing the heat transfer rate on the suction side. Behind the shock location, however, the secondary flows tended to raise heat transfer once again. Finally, when flow approached the trailing edge, the Stanton number was reducing as the boundary layer was growing again. In cases with $M = 0.98$ at the outlet, no shock was observed. After the transition location, the Stanton number data contours develop smoothly towards the trailing edge. The recorded HTC distributions on the airfoil surface for multiple subsonic cases are shown in Figure 5.1a (Case F) and Figure 5.3a (Case D).

The peak Stanton number at the leading edge is decreased by around 20% for test cases with the higher inlet Reynolds number. In the high Reynolds number case, the authors highlighted that the pressure side is transitional, and a complicated suction side Stanton number pattern was observed [8]. Notably, the HTC is proportional to St by $\rho_{in}U_{in}c_p$, according to Equation 4.1. Hence, the Reynolds number relates St and HTC values. Therefore, the pattern of observing a lower peak St in the high Reynolds number cases may not be observed when investigating HTC values.

Finally, it is noted that in the high Reynolds number and low turbulence flow cases (Case G and H) dots of paint affected HTC distribution on the suction side surface. The dots were invisible and ”barely perceptible to touch” but the boundary layer was very sensitive to small disturbances due to the high Reynolds number [8]. These painted dots affected transition at chordwise position $s/span$ = 0.33 on the suction side, and they were painted at 50%, 33% and 67% spanwise locations.

Definition of Stanton number

The adopted Stanton number definition by the authors of the experiment is given in Equation 4.1. Adiabatic wall temperature is used as a reference temperature, and it is computed according to Equation 4.2. Recovery factor r_c is specified as $r_c = Pr^{1/3}$. Prandtl number Pr =0.72 is applied in CFD simulations.

$$St = \frac{q}{\rho_{in}U_{in}c_p(T_s - T_{aw})} = \frac{HTC}{\rho_{in}U_{in}c_p} \tag{4.1}$$

$$\frac{T_{aw}}{T_{t,in}} = r_c + \frac{1 - r_c}{1 + 0.5(\gamma - 1)M_{is}^2} \tag{4.2}$$

The density term ρ_{in} in Equation 4.1 is obtained from the total quantities at the inlet as shown in Equation 4.3 and described by Giel et al. [131].

$$\rho_{in} = \frac{P_t}{RT_t} \tag{4.3}$$

It is noted that the results in [8] are given in terms of the Stanton number. A decision is made to compare the CFD results and experimental test results in terms of HTC, where $HTC = q/(T_s - T_{aw})$ as shown in Equation 4.1, and the given adiabatic wall temperature definition is implemented. Then the Stanton number is multiplied by $\rho_{in} U_{in} c_p$ to convert the experimental results from St to HTC.

Uncertainties in experiment

It is important to acknowledge the uncertainties involved in experimental cases before comparing its results with the CFD simulations. The authors have described the uncertainties and the summary is provided in the following section. Overall, the maximum uncertainty in determined Stanton numbers is less than 13% in the regions where $St < 0.001$. In regions where $St > 0.002$, the uncertainty is below 8%. [8]

The main sources of the uncertainty are the uncertainty of conductance of the low conductivity layer, estimated to be around $\pm$ 5%, together with adiabatic wall temperature (δT_{aw} = 0.6°C), liquid crystal temperature (δT_{lc} = 0.3°C) and copper substrate temperature (δT_{Cu} = 0.3°C). The evaluated error in the Reynolds number and Mach number are $\pm$ 0.003 $\times$ 10^6 for the former, and 0.001 - 0.003 for the latter. Furthermore, it is noted that a correction factor for the radiative heat loss was applied to the determined local surface heat flux q''. With emissivity of ϵ = 0.98, the radiative losses were estimated to be at most 6% but typically much lower for large portions of the blade surface. Subsequently, the radiation correction will not be implemented in CFD simulations. [8]

4.1.2. CFD model setup

The experimental test case is replicated in the CFD model. A periodic model is implemented with the blade geometry consisting of 143 points along the surface of a cross-section. The $Star - CCM+$ software package is used to perform simulations.

Boundary conditions

Boundary conditions are shown in Figure 4.3, and flow boundary conditions in Table 4.3. Periodic boundaries are applied, instead of modelling multiple blades and passages. The stagnation inlet and pressure outlet are the boundaries at inflow and outflow, respectively. By adjusting the outlet pressure, the exit Mach number is adjusted, depending on which flow case is modelled. The inlet total pressure is around 1 atm for simulations with Re_{in} = 1.0 $\times$ 10^6, and around 0.5 atm for Re_{in} = 0.5 $\times$ 10^6. On top of the total pressure, the inlet flow angle, total temperature, turbulence intensity and length scale are specified at the inlet. The pressure side and suction side of the airfoil are treated as no-slip walls with specified temperatures on them. The endwalls are modelled as no-slip adiabatic walls. For a special case when a heat transfer estimate is desired on the endwalls to investigate the secondary flow field, a temperature can be specified, as it was done in a different experiment by Giel [131]. Hence, the endwalls are split upstream of the leading edge at a location $-0.3c_x$, as the endwalls were heated from that location up towards the outlet in that particular experiment. The inlet is placed one axial chord upstream of the leading edge, which is also a location where the turbulence characteristics and the boundary layer width were measured. The outlet is located at $2.7c_x$ downstream from the leading edge, corresponding to the endwall size. This outlet placement is considered far enough downstream since convergence problems were not experienced, and an additional simulation with the outlet placed at $4c_x$ downstream of the leading edge with free-slip condition at the extension of endwalls did not result in significant differences in the flow field characteristics.

Table 4.2: Overview of the test cases as specified by the authors of the experiment [8].

	Ma_{out}	$Re_{x,in}$	Tu_{in}
Case A	1.32	0.5×10^6	8%
Case B	0.98	0.5×10^6	8%
Case C	1.32	0.5×10^6	0.25%
Case D	0.98	0.5×10^6	0.25%
Case E	1.32	1.0×10^6	8%
Case F	0.98	1.0×10^6	8%
Case G	1.32	1.0×10^6	0.5%
Case H	0.98	1.0×10^6	0.5%

Table 4.3: Flow boundary conditions specified in the CFD model. The pressure and temperature values are averaged over inlet or outlet.

$P_{t,in}$	1×10^6 Pa (Cases E-H) or 0.5×10^6 Pa (Cases A-D)
P_{out}	16.9 kPa (Cases A,C); 23.5 kPa (Cases B,D); 30.5 kPa (Cases E,G); 52.0 kPa (Cases F,H)
$T_{t,in}$	300 K
T_{wall}	326 K
Λ_t	6 mm (Cases A,B,E,F) or 1 mm (Cases C,D,G,H)
Tu_{in}	8%, 0.5% or 0.25%

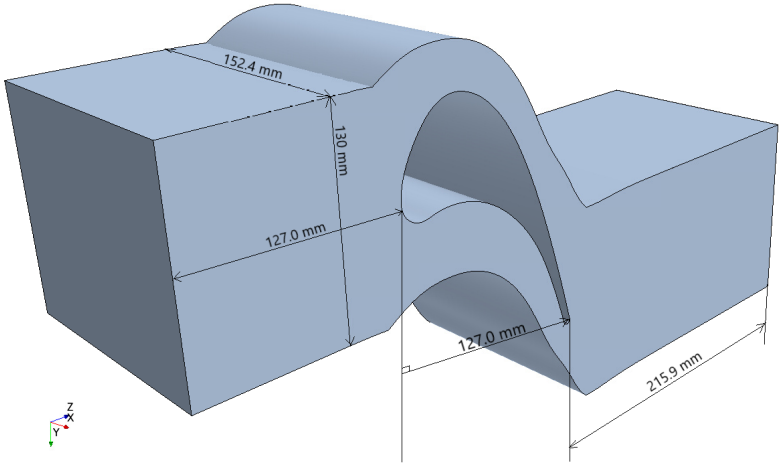

Figure 4.2: Computational domain

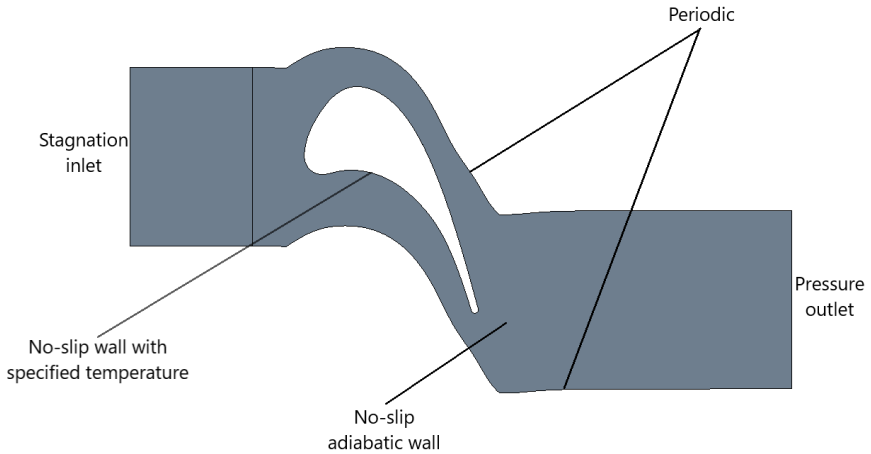

Figure 4.3: Boundary conditions

Inlet boundary layer thickness on endwalls is estimated to be either 2 cm or 3.2 cm in experiments, depending on the flow case. This is replicated by specifying an inlet 2D total pressure and temperature

distribution. The distribution is obtained by simulating a channel flow with the same flow conditions (the same Mach number, Reynolds number, turbulence intensity and length scale) at the inlet and outlet. The channel is modelled with a width equal to the span of the blade. Downstream of the inlet, the endwall boundary layer is growing. Hence, when the boundary layer of the channel flow has developed to the postulated size of 2 cm or 3.2 cm, the total pressure and total temperature profiles at that location are taken and applied then as boundary conditions on the vane CFD model at the inlet. The channel flow is simulated for all eight test cases, considering that the inlet total pressure and boundary layer size vary per case. When specifying a uniform inlet pressure profile, around 10% lower HTC enhancement was recorded in the regions on the suction side close to endwalls.

The ideal gas model is incorporated in the simulations with the ratio of specific heats κ = 1.4. Dynamic viscosity, thermal conductivity and specific heat C_p are dependant on temperature and specified according to experimental data with reference being dry air in atmospheric conditions. Uniform temperature is specified on airfoil walls. The authors of the experiment found out that the implemented measurement technique replicated a uniform temperature boundary condition much closer compared to a uniform heat flux boundary [8]. The average total temperature specified at the stagnation inlet is 300 K, and the temperature on the airfoil surface 326 K in the CFD model. The ratio between the surface temperature and the static inlet temperature is around 1.12, which is between the values reported on the stagnation region and separation region by the authors of the experiment.

Computational grid and solver setup

Steady-state RANS simulations are performed. The y^+ value below one is adopted both on endwalls and airfoil surface everywhere in the computational domain. The maximum cell width expansion ratio in the prism layer is limited to 1.1, both in prism layers on endwall and airfoil surfaces. The minimum orthogonality angle is 30° but for the large parts of the domain it is above 80°. The computational domain consists of around 22 million cells in total. The requirements for the computational mesh are established in order to accurately model the flow such that the main flow phenomena, especially, transition are well predicted. For transitional flows treated with wall integration, it is generally required to have y^+ < 1 on walls which sets the requirement for the adjacent-to-wall cell width. Importantly, streamwise refinement should be fine enough to capture transition onset accurately. Especially, the transitional models, like $\gamma - Re_\theta$, require high resolution in the streamwise direction to calculate the location where the transition starts [60]. Similarly, secondary flow refinement can be dependant on streamwise resolution, especially by the SST model [81, 103]. The suction side mesh refinement is shown in Figure 4.5. The pressure side is resolved with 156 nodes and the longer suction side with 304 nodes. The aim is to achieve a fine resolution of the computational domain also in a spanwise direction to sufficiently resolve secondary flows and potential crossflow.

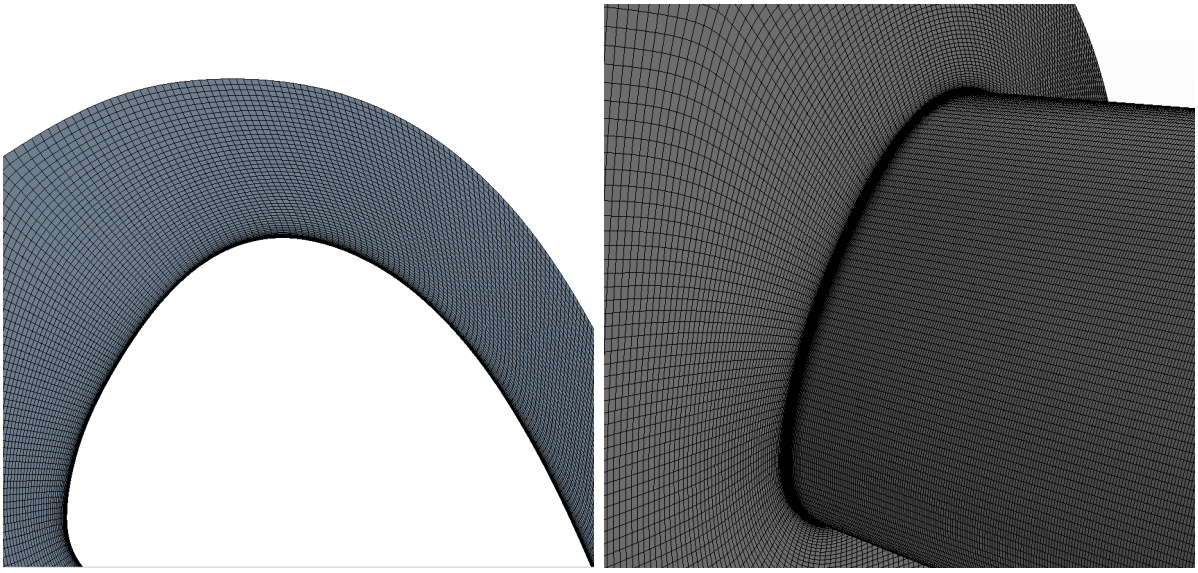

(a) Mesh resolution on the suction side. **(b)** Mesh on the endwalls and in spanwise direction.

Figure 4.4: Computational mesh

The non-normalised residuals are aimed to be below 1×10^{-5} to reach convergence. As compared to residuals for momentum equations, the energy equation residual was usually larger and was aimed to be below 1×10^{-4}. Additionally, heat transfer rate monitors are incorporated to investigate convergence. In recent literature, grids of five to ten million cells are reported when evaluating secondary flows [55, 100]. The computational mesh limitations and requirements, however, largely depend on the resources of a particular study. Smirnov et al. [81] highlighted the importance of grid refinement in HTC calculations when investigating the Giel cascade.

Turbulence and transition models

Based on the results of the literature study, the turbulence models chosen for analysis are SST $k-\omega$, lag elliptic blending $k-\varepsilon$ and $\overline{v^2}-f$ models. The SST $k-\omega$ model is analysed with and without coupling the transitional $\gamma - Re_\theta$ model. Considering that accounting for the turbulence anisotropy is of importance when modelling secondary flows, the quadratic and cubic constitutive relations will be applied to the SST model. Curvature correction is optional as well. The freestream edge of 5 mm is defined for the $\gamma - Re_\theta$ transition model. Results were found to be insensitive to freestream edge varying between 1 mm to 10 mm. The various correlations for transition parameters F_{length} and $Re_{\theta,c}$, as explained in Section 3.5.2, are Suluksna-Juntasaro (the default option in *Star-CCM+*), Kelterer et al. [130] and Sorensen [128]. Furthermore, the crossflow term can be added to the $\gamma - Re_\theta$ transition model. The horseshoe vortex is pushed towards the midspan as the flow is approaching the trailing edge. Considering the vortices in the streamwise direction, the streamlines locally are directed towards the midspan in the spanwise direction, and the crossflow term itself includes the streamwise vorticity as well. These factors serve as arguments for investigating the simulation with crossflow transition term.

A scale-resolving-hybrid (SRH) is a hybrid RANS-LES formulation that was applied to this flow case as well. Implementation of the SRH model implies the use of transient simulation. A second order implicit upwind scheme was implemented. An adaptive time step was used to ensure the CFL number below unity in the majority of the domain. The target mean CFL was set at 0.80. It was observed that the time-steps were in the magnitude of 1×10^{-6} seconds. The number of inner iterations was set to ten, and 5-10 flow-throughs were simulated after a start-up time. A total computation time starting from the initial RANS solution was around one week on 56 cores. The SST $k-\omega$ turbulence model is selected for RANS regions. The hybrid model was implemented to study the unsteadiness of the horseshoe vortex, rather than to compare HTC data to the steady-state measurements. For a scale resolving simulation, it is challenging to impose a representative turbulence level at the inflow that matches the experimental case based on measured turbulence intensity and length scale.

Anisotropic linear forcing is implemented to achieve a realistic turbulence level at the inflow. It is a numerical method for synthetic turbulence generation available in Star-CCM+ software. A forcing volume is picked at the inflow, extending from the inlet plane to a location of approximately three boundary layer widths in front of the leading edge. A similar volume is then applied to the previously simulated RANS solution. The RANS-calculated turbulence intensity, velocity components and dissipation rate are extracted from the solution in that forcing volume. Finally, the obtained field solution is applied to the forcing volume in the scale resolving hybrid simulation.

4.1.3. Main sources of uncertainty

It is expected that the turbulence and transition modelling error can lead to the largest imposed uncertainty in CFD results. However, in this section other uncertainties are addressed regarding the factors influencing an objective comparison between CFD and experimental results.

- Even though the HTC calculation and temperature difference are scaleable due to temperature difference directly affecting the heat flux calculations, the **specification of temperature on the walls** affects the HTC results.
- A **uniform temperature** is specified on the airfoil, but the authors of the experiment recorded a variation of around 20 K between the stagnation point and regions where the flow separates. Nevertheless, the authors specified that the boundary condition is much closer to a uniform temperature as compared to heat flux which had a considerably stronger variation.
- The **radiative losses** at some locations can result in up to 6% of the total heat flux rates but mostly are much lower, according to the authors of the experimental test cases. Since the radiation is not modelled, it can impose a small error.
- Even though the incoming **endwall boundary layer** width is specified, the exact profile might not match the one obtained in experiments.
- When presenting the results, the **location where the pressure side is distinguished from the suction side** is not rigorously defined. The authors specify that $s = 0$ at the "geometric stagnation line" [8], suggesting that the stagnation point is where separation from pressure and suction sides is defined. However, that does not allow investigation if CFD predicts the same exact stagnation point.
- In literature, the **turbulent Prandtl number** is mentioned to vary between 0.7 to 0.9. The value of 0.85 is incorporated in the simulations, however, since no measurements were taken during the experiment, it is taken into account as an uncertainty. The turbulent Prandtl number appears in the turbulent heat flux equation in *Star-CCM+* (Equation 3.7) which is incorporated in the energy equation. A different value can make HTC appear slightly higher or lower on various parts of the airfoil surface but it does not affect transition location or length.

These mentioned uncertainties should be taken into account, however, it is deemed that their influence on the comparison of results is relatively modest when compared to turbulence modelling errors. Furthermore, the turbulence length scale to be specified at the inlet largely influences the turbulence intensity and kinetic energy downstream, following decay, and it largely affects the calculations of turbulence models. The length scale measured in experiments typically differs from CFD code definitions, as explained in Section 3.5. It is important to address the length scale effects on HTC distribution, and a sensitivity study is performed by analysing multiple simulations with various turbulence length scales. The unsteady nature of secondary flows is another phenomenon imposing uncertainty in results. It is observed that the SST model tends to model small structures of the horseshoe vortex in steady-state simulations, which might be present only momentarily in experiments [103]. The implementation of turbulence characteristics and unsteadiness of secondary flow are two aspects interfering with the model flow field calculations, hence, are likely error sources.

4.1.4. Mesh sensitivity study - validation case

Mesh sensitivity study is performed implementing the SST $k - \omega$ turbulence model which tends to be susceptible to grid refinement [132]. Transitional model $\gamma - Re_\theta$ with Suluksna-Juntasaro correlation

is incorporated. The high Reynolds number flow case ($Re = 10^6$) is used since it imposes the limiting requirement for the first cell width regarding y^+ value as compared to the low Reynolds number ($Re = 5 \times 10^5$) case. The case with low turbulence intensity is used to investigate if a simulation with refined mesh predicts the same laminar-turbulent transition location.

The original mesh is made in an attempt to accurately model the flow such that the main flow phenomena, especially, transition are well predicted. This is done by implementing the grid requirements described in Table 4.1.2. At first, the computational mesh is made coarser in the streamwise direction to study the effects of streamwise grid refinement. The streamwise resolution was halved, but the effects on the bulk flow far away from the wall were negligible with flow parameters differing by less than 0.5%. However, closer to the walls the shear force and skin friction coefficient results were differing substantially between the two simulations. Especially, the HTC predictions on the airfoil surface were affected. This initial investigation was performed in order to establish that streamwise mesh refinement is of high importance in the following sensitivity study, on top of the mesh refinement in the normal to wall direction close to airfoil and endwall surfaces.

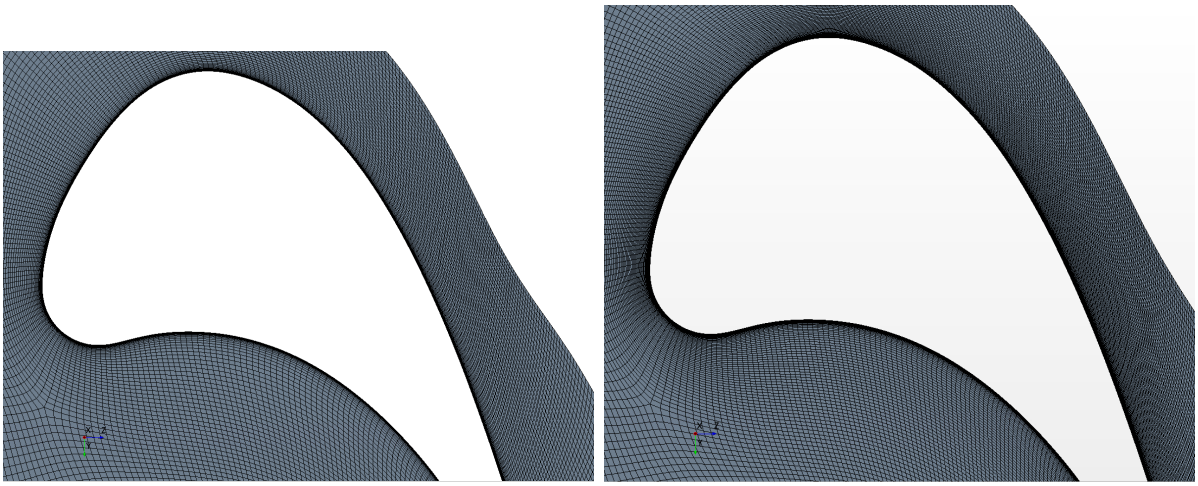

(a) Original mesh **(b)** Finer mesh

Figure 4.5: Computational domain close to the airfoil surface. More nodes are implemented in the streamwise direction.

The original mesh of 22 million cells is compared with a refined mesh in Table 4.4. The differences in the calculated flow field with respect to the original mesh are negligible, therefore the mesh is shown to be independent regarding the resolution of the bulk flow. The mesh is refined to achieve a higher streamwise resolution, and by putting more cells around the airfoil surface in the prism layer where the boundary layer is modelled. In both cases, y^+ < 1 on airfoil and endwalls, and a finer mesh consists of 36.6 million cells. The original mesh implements 157 nodes along the pressure side and 305 along the suction side, whilst the refined mesh has 189 and 369 nodes, respectively.

Multiple flow parameters are displayed in Table 4.4. The parameters on the inlet and outlet are mass flow averaged, the HTC around the airfoil and forces are integrated across the surface elements. It is shown that the discrepancy between the simulated flow characteristics is less than 1% for all parameters, the majority of them having even a significantly lower discrepancy. After making the original mesh with sufficient streamwise resolution, the discrepancies in HTC, skin friction coefficient and shear force disappeared when refining the mesh. The HTC distribution around the airfoil is shown in Figure 4.7 at midspan. The results suggest that the original mesh has a sufficient resolution for HTC calculations.

Table 4.4: Comparison of the main flow parameters between simulations with the original and the refined mesh. Both simulations were performed with the SST $k-\omega$ turbulence model.

	Original mesh	Refined mesh	Difference in %
Number of cells	22 379 520	36 683 136	
Ma at inlet	0.382	0.382	0.01
Ma at outlet	1.324	1.327	0.20
Re_x at inlet	1.00×10^6	1.00×10^6	0.00
Re_x at outlet	1.65×10^6	1.65×10^6	0.00
Shear force on vane(N)	1.456	1.507	3.81
Pressure force on vane(N)	1081.6	1079.1	0.23
Heat transfer across endwall (W)	840.18	837.04	0.37
Heat transfer across vane (W)	822	857	4.51

The pressure distribution around the airfoil at midspan is shown in Figure 4.6a. The agreement on both suction and pressure sides is remarkable, hence the pressure distribution solution is grid-independent. Skin friction coefficient distribution at midspan is displayed in Figure 4.6b, a similar distribution is obtained in both cases. Only close to the shock location on the suction side there is a slight discrepancy due to streamwise refinement. However, it is expected because the shock is a discontinuity in the flow field.

The HTC distribution around the midspan of the vane is shown in Figure 4.7. The agreement on the pressure side is apparent. Also, on the suction side, the HTC is predicted similarly between the two meshes. The highest discrepancy is right after the transition onset at $x = 0.35c_x$ where the finer mesh predicts HTC about 4% higher. However, it is important that the transition location is predicted consistently, and the results of the two meshes agree on transition starting at x = 0.34c_x in this particular flow case. The other location where a streamwise refinement is beneficial is at the shock location at $x = 0.85c_x$, however, calculations on both meshes give comparable results.

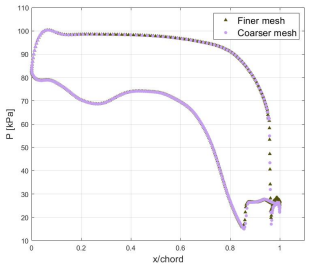

(a) Pressure distribution at midspan, comparison between the simulations with the original and the refined mesh.

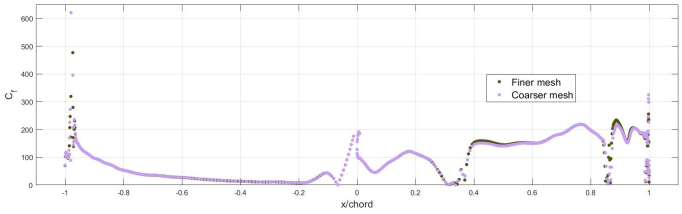

(b) Skin friction coefficient at midspan, comparison between simulation results with the refined and the original (coarser) meshes.

Figure 4.6: Mesh sensitivity study: a comparison of pressure and skin friction distributions at vane midspan.

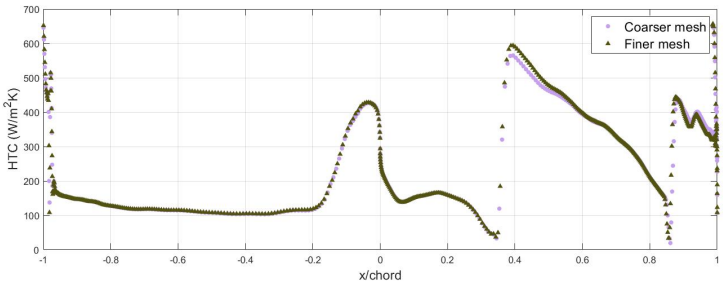

Figure 4.7: HTC at midspan - comparison between the original and the refined mesh

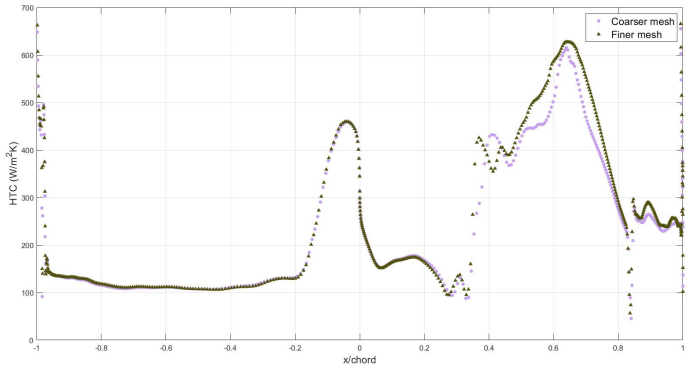

Figure 4.8: HTC at 10% span as predicted with simulations with the original mesh and refined. The secondary flow HTC enhancement is predicted slightly differently.

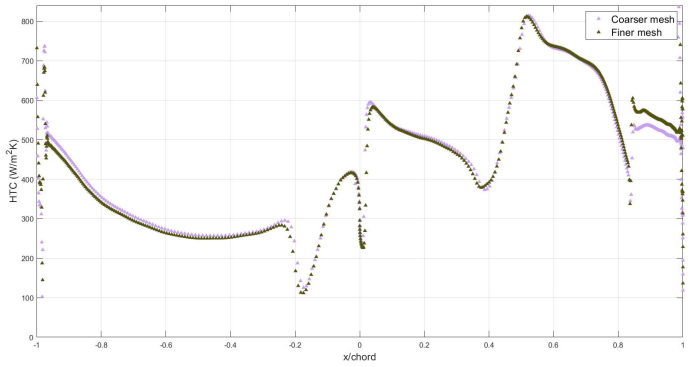

Figure 4.9: HTC at 10% span as predicted by simulations with the original mesh and the refined mesh when implementing the lag EB turbulence model. Secondary flow HTC enhancement is predicted similarly.

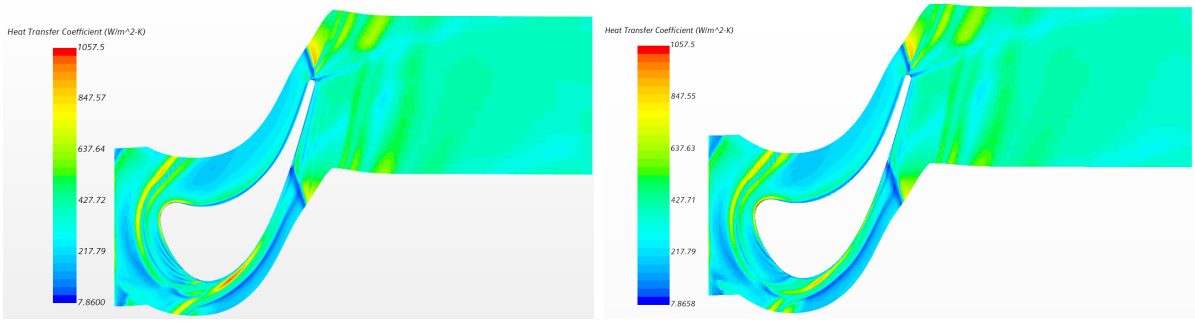

(a) Endwall HTC pattern with the finer mesh

(b) Endwall HTC pattern with the original mesh

Figure 4.10: Mesh sensitivity: predicted HTC patterns on the endwall by both, refined and original, meshes.

Endwall patterns of HTC are obtained by specifying a constant temperature on the endwalls, and the results are displayed in Figure 4.10. By a visual inspection, it is noted that the HTC pattern is calculated similarly with both meshes, the finer mesh is able to refine the vortex structures in front of the airfoil slightly more than the original mesh. The shock is predicted at the same location with both grids and the figures display the horseshoe vortex forming before the leading edge. Furthermore, the HTC enhancement close to the suction side is predicted similarly with both meshes but the strength of vortices within the horseshoe vortex system slightly differs.

It is challenging to capture the secondary flows due to their inherently unsteady nature. When investigat-

ing the HTC distributions at 10% span (Figure 4.8), the agreement between two meshes, in general, is satisfactory, especially on the pressure side. The region of uncertainty is on the suction side where the secondary flow vortices are impinging on the vane surface. In that region from $x = 0.35c_x$ to $x = 0.60c_x$, even within a single simulation, the HTC solution is varying per iteration after reaching convergence. It is noted that residuals are oscillating as well for the SST $k - \omega$ simulation, hinting at unsteadiness in the flow field. It is argued that due to the unsteadiness of a three-dimensional vortex, iteration by iteration the steady-state solver approaches a slightly different solution whilst trying to approximate the solution of a secondary flow field. However, this variation is present irrespective of the mesh refinement. Notably, the implementation of the transition model is also affecting the HTC calculation. The same shock location is predicted by both meshes. Furthermore, the finer mesh predicts a higher HTC just after the shock location on the suction side at 10% span. The maximum discrepancy of around 5% in that region is deemed acceptable considering that the primary focus of the study is not on the shock refinement.

The first HTC enhancement after the transition is associated with the suction side leg of the horseshoe vortex impinging on the wall. The secondary flow field and visualisations are shown in Section 2.1. As found by Levchenya et al. [103], the SST $k - \omega$ model refinement of the horseshoe vortex system is dependant on the mesh resolution. Levchenya found that by creating a finer mesh, more structures of horseshoe vortex appeared before the leading edge. However, in experiments they were observed only momentarily [103, 104]. These findings suggest that the steady state solver is unlikely to reach a complete mesh independent solution of the secondary flow field due to the unsteadiness of the vortex system. A similar set of simulations is performed with the lag EB model with HTC distribution at 10% span displayed in Figure 4.9. Notably, the lag EB model with both, coarser and finer, meshes predicts a matching HTC distribution. However, the model also does not predict the suction side horseshoe vortex leg attaching to the surface and causing an additional streak of large HTC on the suction side (see Figure 5.6). Nonetheless, the solution with the lag EB model is deemed mesh independent. The HTC enhancement after the shock is higher for the finer mesh, which is the only considerable discrepancy.

The mesh independence study has highlighted some of the intricacies when calculating the secondary flow field. A finer mesh in a streamwise direction is desired to better resolve shock and transition location. The finer mesh showed more variations in the secondary flow field as predicted by the steady-state solver with the SST model. The potentially unsteady behaviour suggests that URANS might be a valuable tool in evaluating HTC enhancement due to secondary flows impinging on the wall. Nonetheless, the steady solution of the SST model can give a representative solution and resolves the general features of the flow field. The mesh resolution impact on resolving the secondary flow field varies depending on the implemented turbulence model. The simulations with the lag EB model provided a fully mesh independent solution in the flow case F. Considering the calculation of the bulk flow and heat transfer data on the airfoil midspan, the mesh independence has been shown but care should be taken with SST simulations when investigating the region on the suction side where the horseshoe vortex is impinging on the wall.

4.1.5. Sensitivity to turbulent length scale

A sensitivity study is performed to analyse the impact of the freestream turbulent length scale on the predicted HTC results and flow field. Case F is chosen for analysis with $Tu = 8\%$ at the inlet and subsonic exit. It was observed that for low turbulence intensity ($Tu = 1\%$) cases the chosen length scale in the range of 0.1 mm to 10 mm did not significantly affect the results. First, the concept of turbulence decay is presented in Section 4.1.5. The results of the sensitivity study are discussed in Section 4.1.5. In the experiment, the authors reported an inlet integral length scale of 0.22 of the axial chord, which equals 30 mm [8]. As already established in Section 3.5 regarding the SST model, the energy length scale to be implemented in CFD codes is typically lower than measured in experiments, and a 6 mm length scale is used for comparison with experimental data. Considering that lag EB $k - \varepsilon$ and SST $k - \omega$ models predicted results with a closer agreement to the data when compared to the $\overline{v^2} - f$ model, these two models are implemented in the sensitivity study. Four different length scales are analysed for both lag EB and SST simulations - 0.1 mm, 1 mm, 6 mm and 30 mm. Furthermore, it should be noted that the implementation of length scale in the respective turbulence models slightly differs between the models, as explained in Section 3.5.

Turbulence decay

Turbulence decays due to dissipation and can increase only due to the presence of shear. Hence, in a gas channel or in a turbine passage, the turbulence intensity is decaying unless the shear force is present. Turbulence intensity is used in the calculation of turbulent kinetic energy Equation 3.19, which, in turn, is directly tied to the eddy viscosity (Equation 3.15), which affects the heat transfer (Equation 3.7). Therefore, turbulence decay is affecting the HTC distribution on the airfoil, it is likely that various turbulence models treat the decay slightly differently. Therefore, by changing the size of the largest energy-carrying turbulent structures at the inlet (turbulent length scale), turbulence decay will be affected. For example, since the turbulence intensity is decaying along the gas channel, a case with a higher length scale at the inlet would likely have a higher turbulence intensity locally at a specific location in the gas channel when compared to a case with a smaller turbulent length scale. Correspondingly, this leads to different values of turbulent kinetic energy calculated and also different HTC values.

Results of the sensitivity study

First, the flow cases simulated with the SST model coupled with the $\gamma - Re_\theta$ transition model are analysed and HTC data on midspan are shown in Figure 4.11a. On the pressure side, consistently, a higher length scale results in a higher HTC. From 1 mm to 30 mm length scale cases are relatively comparable on the suction side as well, predicting a similar pattern, but the 0.1 mm case vastly underestimates the HTC and also assumes a laminar boundary layer. Hence, the transition is predicted on the suction side by the SST $\gamma - Re_\theta$ model with a 0.1 mm length scale. An early transition is predicted with the simulation with 1 mm, which is also apparent in the experimental data. The length scale of 0.1 mm, thus, does not represent data and is a strong outlier among the others. The 6 mm length scale gives the closest agreement with the data on the pressure side at midspan where the flow is not affected by secondary flow phenomena, however, the suction side HTC is slightly underpredicted. Simulation with a 30 mm inlet length scale predicts the highest values on midspan which is expected since the local turbulence intensity is higher. Notably, the overprediction of HTC at the leading edge is apparent for simulations with 6 mm and 30 mm length scales whilst the 1 mm length scale replicates the stagnation HTC the closest.

By investigating the 10% span data on the suction side (Figure 4.11) and analysing the simulation results in terms of HTC distribution on the blade suction side (Figure 4.12), the additional streak of high HTC is suppressed by a higher turbulence level. The suction leg of the horseshoe vortex is not that strong for higher turbulence intensity levels. This is due to the boundary layer on the endwalls being smaller in size as the high turbulence suppresses it. However, the maximum HTC at 10% span is recorded for the6 mm length scale, followed by 30 mm, and 6 mm also represents the experimental data the closest. Sensitivity is apparent. As the larger turbulence intensities suppress the incoming endwall boundary layer, the effect of the horseshoe vortex on the suction side is weakened. The 30 mm length scale simulation has only two enhancements of HTC in SST simulations whilst 6 mm and 1 mm length scale simulations predict multiple structures of HS vortex impinging on the suction side, on top of the HTC enhancement by passage vortex, as shown in Figure 4.12.

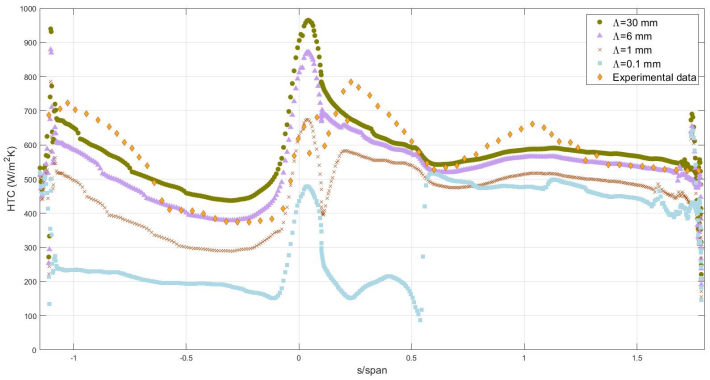

(a) Midspan

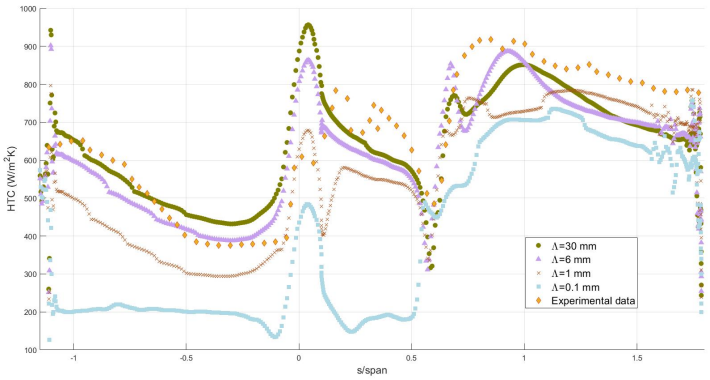

(b) 10% span

Figure 4.11: HTC rates on the airfoil surface along the streamwise direction. A comparison is made between the experimental data and simulations with the SST $\gamma - Re_\theta$ model and different turbulent length scales at the inlet.

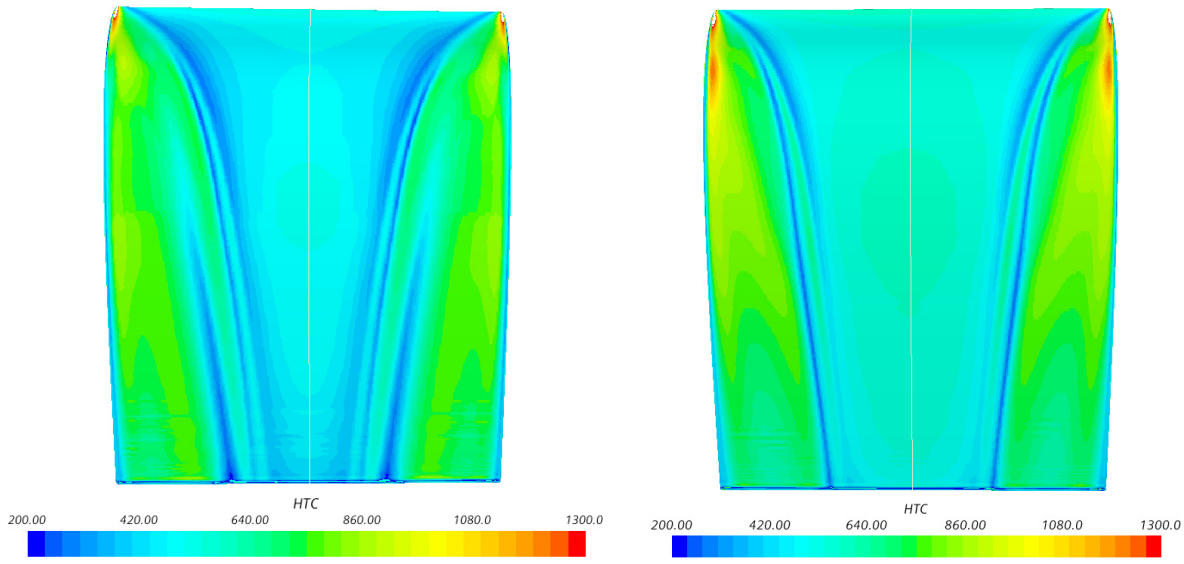

(a) 1 mm turbulent length scale at the inlet

(b) 30 mm turbulent length scale at the inlet

Figure 4.12: HTC distribution on the suction side of the airfoil, as predicted by simulations with the SST $k - \omega$ model with different turbulent length scales. HTC is enhanced when implementing the large length scale at midspan but the suction side leg of the horseshoe vortex is suppressed.

The following two are the main conclusions of the sensitivity study. In the regions where secondary flows do not influence the HTC data, a larger inlet length scale corresponds to a higher HTC, as the higher length scale leads to locally higher turbulence intensity and turbulence kinetic energy, leading to a larger eddy viscosity in those regions. Meanwhile, the secondary flow effects can be strong with smaller length scales, since the endwall boundary layer has a larger size for low turbulence intensity cases, resulting in a stronger horseshoe vortex system. The higher turbulence intensity suppresses the incoming endwall boundary layer.

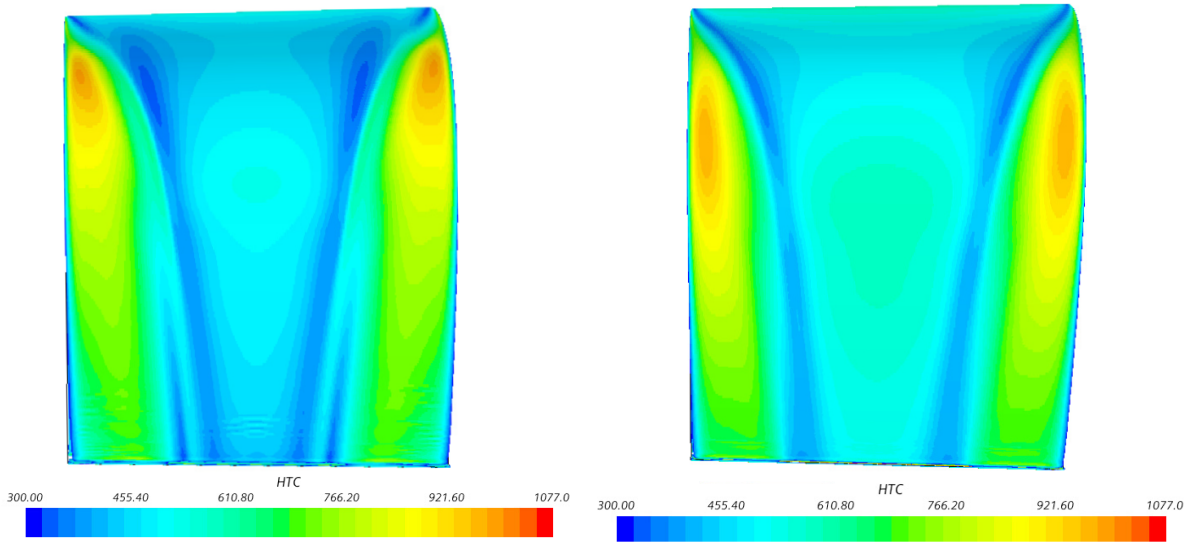

(a) 1 mm turbulent length scale at the inlet

(b) 30 mm turbulent length scale at the inlet

Figure 4.13: HTC distribution on the suction side of the airfoil, as predicted by simulations with the $k-\varepsilon$ lag EB model with different turbulent length scales. HTC is enhanced when implementing the large length scale at midspan but the additional line of high HTC disappears, which is associated with the suction side leg of the horseshoe vortex.

Similar to the SST $\gamma - Re_\theta$ model, the lag EB model also, consistently, predicts a higher HTC on the pressure side with a larger turbulent length scale, and results are sensitive to the inlet length scale, as was expected. Again, only the 0.1 mm length scale gives non-comparable results with a slightly different HTC trend on the pressure side of the airfoil, as shown in Figure 4.14a. The 30 mm length scale greatly overestimates the pressure side HTC, and 1 mm or 6 mm simulations give the closest agreement to experimental data, a similar trend as observed with the SST model. The early part of the suction side, however, is well estimated by the 30 mm length scale on midspan. It must be noted, however, that an overprediction of HTC is recorded at the stagnation point in all simulations, except for the length scale of 0.1 mm.

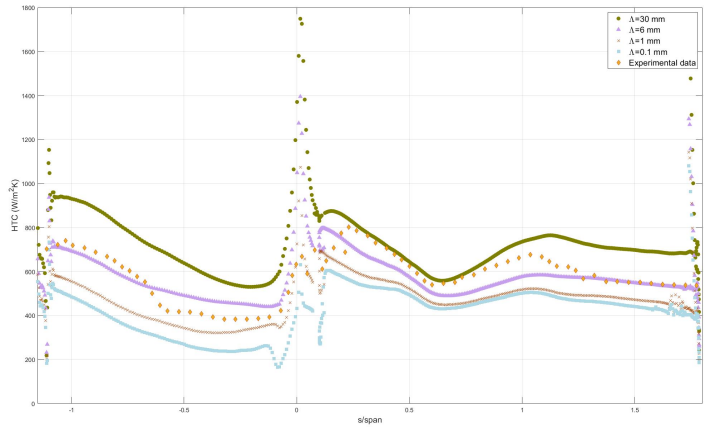

(a) Midspan

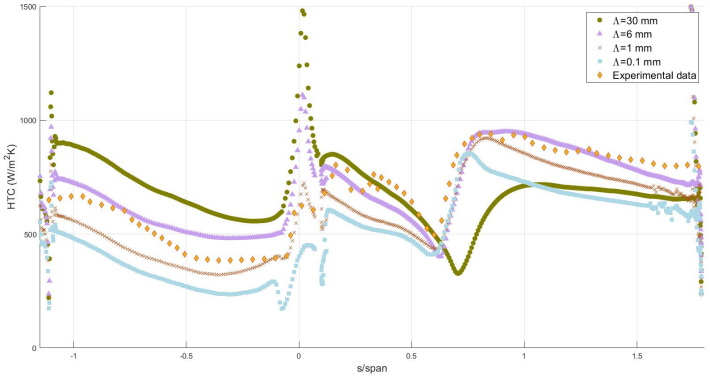

(b) 10% span

Figure 4.14: HTC rates on the airfoil surface along the streamwise direction. A comparison is made between the experimental data and simulations with the $k - \varepsilon$ lag EB turbulence model and different turbulent length scales at the inlet.

An investigation of Figure 4.13 suggests that the simulation with a small turbulence length scale of 1 mm predicts an additional streak of enhanced HTC, as SST $\gamma - Re_\theta$ does. However, it is quite weak in the lag EB model simulation, and it disappears in simulations with 6 mm inlet length scale or larger. This streak corresponds to the suction side leg of the horseshoe vortex. Notably, the closest agreement with the data at 10% span is for the simulation with a 6 mm length scale, i.e. the length scale replicating the length scale specified by Giel. The 30 mm length scale results in significantly underestimated HTC enhancement on the suction side due to a suppressed endwall boundary layer. Simulations with 1 mm and 0.1 mm length scales replicate the experimental data on the suction side, recording 5%-20% lower HTC values towards the trailing edge on the suction side, as compared to the simulation with 6mm inlet length scale. However, it cannot be stated conclusively that the simulations with a 6 mm inlet length scale have better agreement with experimental data when compared to a 1 mm length scale. Generally, towards the trailing edge the former recorded better agreement with the data, but 1 mm length scale simulations provided closer agreement at the leading edge and regions close to it. However, the additional streak of high HTC reported on the suction side in Figure 4.13 when using 1 mm length scale is not observed in the experimental data. In lag EB model implementation, similarly to the SST model, the range of magnitude between 1 mm and 10 mm is appropriate for representative inlet length scale specification.

The turbulence length scale sensitivity study has highlighted the importance of selecting a representative length scale at the inlet. Due to turbulence decay, the chosen length scale influences how large is the turbulence intensity locally, and, thus, affects the HTC and transition. However, the sensitivity study has also shown that the length scale affects the strength of horseshoe and passage vortices. Similar

findings are observed also in low Reynolds number (0.5×10^6 flow cases) and high inlet turbulence intensity case A when implementing Kelterer correlations for F_{length} and $Re_{\theta,cr}$. Transition onset shifts significantly downstream when implementing length scales below 1 mm, whilst the length scales of a 6 mm or similar represent experimental data the closest. The 6 mm turbulent length scale is chosen for simulations with both, SST $k-\omega$ and lag EB, turbulence models.

4.2. Film cooled vane

A numerical study is performed investigating a transonic turbine nozzle guide vane equipped with showerhead film cooling. Adiabatic film cooling effectiveness is analysed. RANS and scale-resolving hybrid RANS-LES simulations are performed, both with a uniform inflow and with a swirling inflow. The aims are to establish the benefits of hybrid CFD modelling, and to investigate the showerhead film cooling effectiveness under different inflow conditions.

4.2.1. CFD model description

The implemented nozzle guide vane is LS89 from von Karman institute [113]. Multiple studies have been performed investigating flow physics around this vane in an uncooled condition [58, 113], and with pressure and suction side film-cooling [9]. The flow turning angle is relatively low, there is not a strong horseshoe vortex forming as compared to the validation case. In the current study, a showerhead film cooling configuration is applied to the vane. The cooling effectiveness is investigated in a case with uniform inflow and a swirling inflow. The showerhead cooling consists of three rows of cooling channels spanning the whole leading edge between endwalls which are modelled as flat surfaces. The geometrical parameters of the domain are listed in Table 4.5.

The cooling channels are cylindrical with a diameter of 0.7 mm. The cooling holes are staggered in multiple rows on the airfoil surface. The cooling hole pitch within a row is 4 mm or 5.7 cooling channel diameters. The coolant channel length is 4.5 diameters. The cooling channels are at a 35° angle to the vane surface, i.e. the coolant injection angle $\beta = 35°$ as visualised in Figure 4.16a. The coolant channels are angled perpendicularly to the mainstream direction to ensure a crossflow. The design of the showerhead is unique but a prior investigation is performed in order to replicate a realistic setup. The stagnation line of NGV can be unsteady, hence, attention is on ensuring that the pressure side has coolant coverage in various conditions. The suction side coolant coverage is less critical since the lower pressure on that location tends to draw the gas and coolant to the suction side in the limiting case when holes are very close to the stagnation line.

Table 4.5: Vane geometrical parameters

Chord	67.647 mm
Axial chord	36.985 mm
LE radius	4.127 mm
TE radius	0.710 mm
Vane span	80 mm
Vane pitch	57.5 mm
Cooling hole diameter, D	0.7 mm
Cooling hole pitch	5.7D
Cooling channel length	4.5D
Coolant injection angle	35°

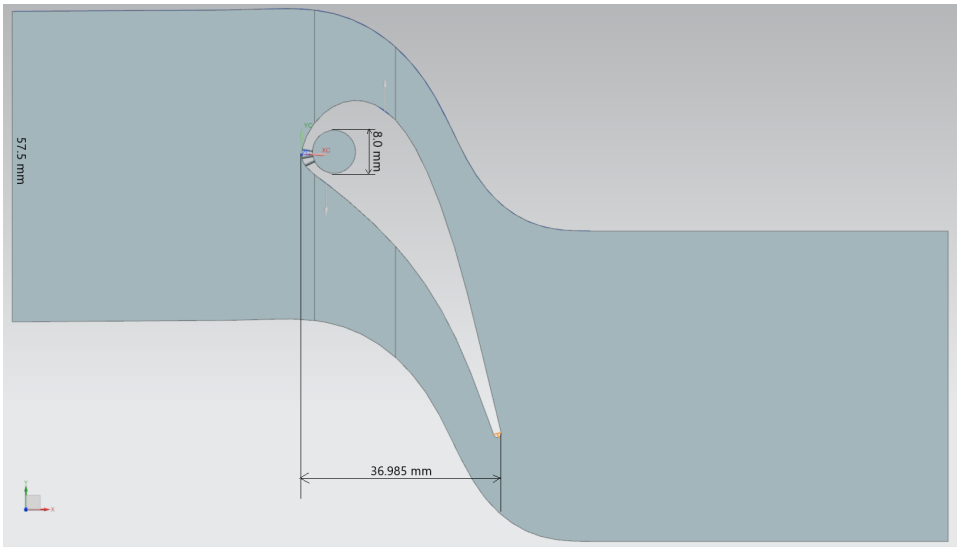

Figure 4.15: Geometry of the domain

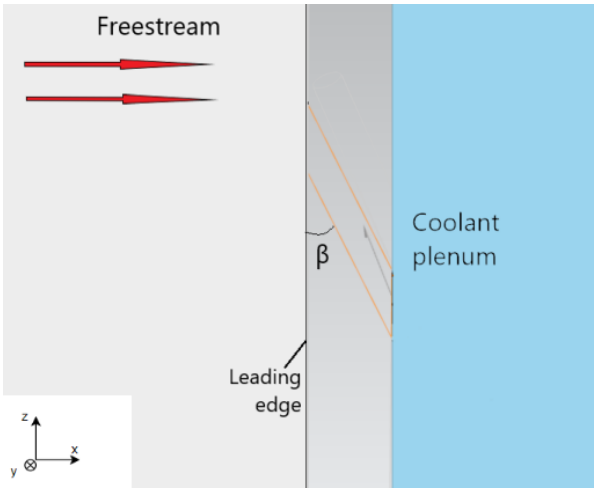

(a) Injection angle β. A schematic top view of the vane leading edge and a single cooling channel.

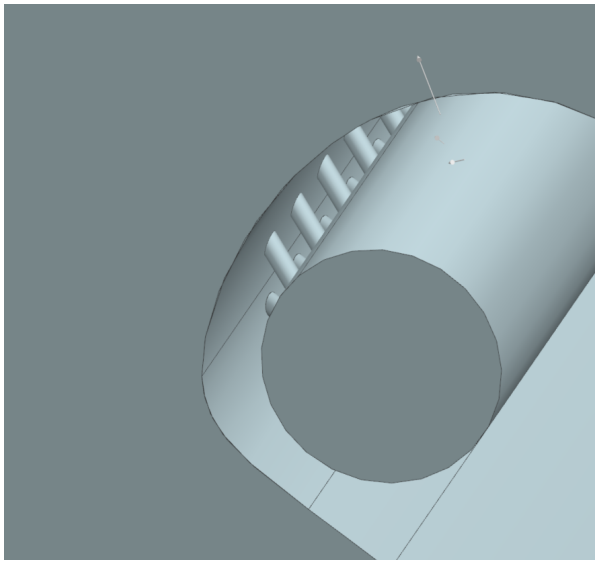

(b) Coolant plenum inlet and cooling holes

Figure 4.16: Geometry of coolant plenum and cooling channels.

Boundary conditions

Stagnation inlet and pressure outlet are implemented with total pressure specified at the mainstream inlet and static pressure at the outlet. The total temperature is also specified at the inlet, and this value is implemented in cooling effectiveness calculations. The periodic boundary condition is specified for the surfaces at the top and bottom of the domain. The endwalls and vane surface are modelled as adiabatic. A coolant plenum is modelled with a separate pressure inlet and outlet, and a lower temperature air is used as a coolant. Stagnation inlet and pressure outlet are applied for the coolant plenum, the cooling channels connect the plenum to the mainstream domain.

The temperature ratio between coolant and mainstream together with the blowing ratio are two important parameters to consider. A blowing ratio of 1.40 is used and it relates the momentum of coolant to the momentum of the mainstream, defined in Equation 4.5. Considering that the pressures are specified at domain boundaries, the BR parameter can be adjusted by regulating the pressures of the mainstream and coolant gases. The ratio of total temperatures between coolant and mainstream

$T_{t,c}/T_{t,\infty}$ = 0.71. The inlet-to-coolant pressure ratio was kept relatively low to ensure a low blowing ratio. However, it has been shown in experiments that even at low blowing ratios the coolant at the showerhead region is susceptible to lift-off due to relatively large injection angles [133].

The implemented pressure and temperature values are lower than in the actual gas turbine conditions, however, the flow physics are similar and the problem regarding cooling effectiveness is largely scalable. The pressure and temperature at the inflow are taken to roughly replicate the same range of magnitude of the experimental conditions on the NASA C3X vane, used in the study by Mangani et al. [134]. The aim is not to replicate the overall experiment conditions fully as the considered cooling configuration is different. The ideal gas model is implemented for air with the ratio of specific heats $\kappa = 1.4$. The total pressure and total temperature specified at the mainstream inlet are $P_{t,in}$ =300 000 Pa and $T_{t,in}$ =700 K, and at the coolant plenum inlet these are $P_{t,c}$ =310 000 Pa and $T_{t,c}$ =500 K, respectively. The mainstream outlet static pressure is set at 184 000 Pa, corresponding to an isentropic Mach number of 0.85 at the outlet. For RANS simulations, the turbulence intensity specified at the inlet is 8% and the length scale is 8 mm. A high turbulence intensity of 10% is specified at the coolant plenum.

Table 4.6: Flow parameters.

$T_{t,c}/T_{t,\infty}$	0.71
$P_{t,c}/P_{t,\infty}$	1.033
BR	1.40
$Ma_{is,out}$	0.85
$Re_{x,out}$	0.9×10^6

Computational domain

The geometry is created with a CAD model which is then imported into $Star - CCM+$ simulation software. A polyhedral $Star - CCM+$ mesher is used for mesh generation.

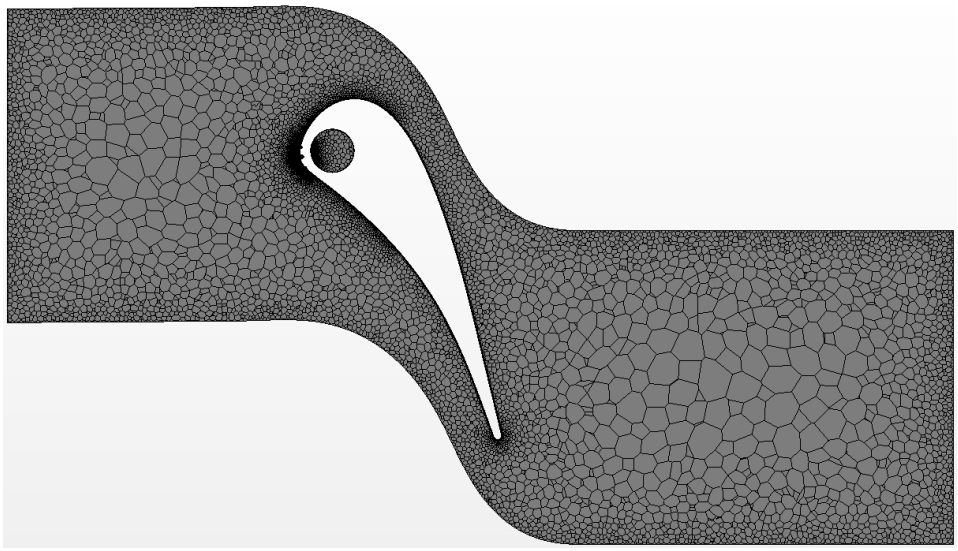

Figure 4.17: Computational grid for the film cooled vane RANS simulations, a cross-section at vane midspan.

The polyhedral mesh has a 0.6 mm base cell size specified in the domain, and the base cell size of 0.054 mm is used in the leading edge region and in the cooling channels. The midplane section of the complete computational domain is shown in Figure 4.17. Volumetric meshing control is applied in the cooling holes and the region on the leading edge in the direct vicinity of the holes as shown in Figure 4.18. This is done in order to ensure that the large grid requirements are met in the region where the coolant is interacting with the mainstream. The region on the vane just outside the leading edge is equipped with a surface control to ensure high resolution in the prism layer and smooth transition from the very fine leading edge mesh. The regions further away from the leading edge and airfoil surface

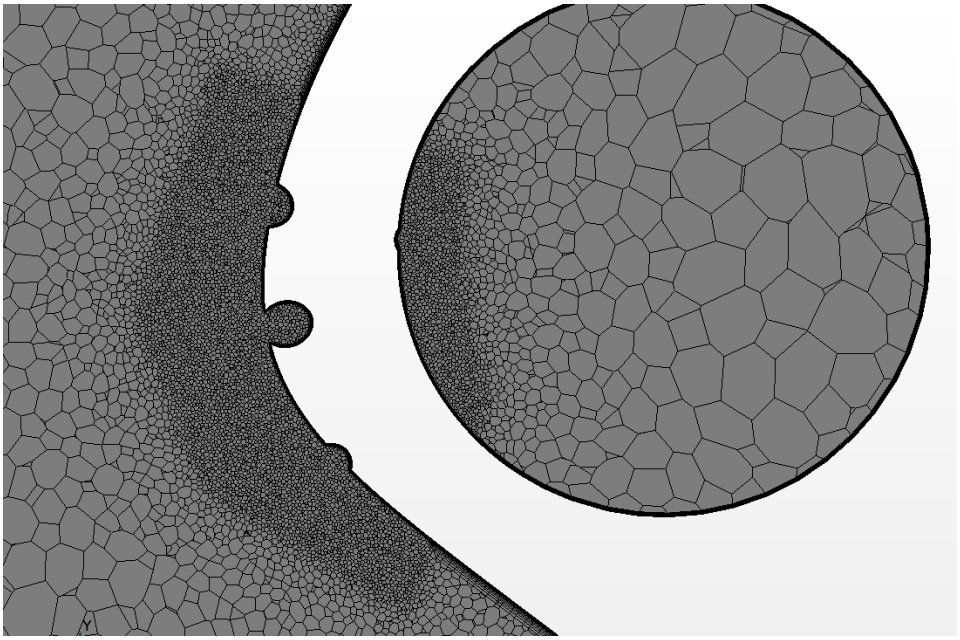

Figure 4.18: Coolant plenum and leading edge mesh resolution.

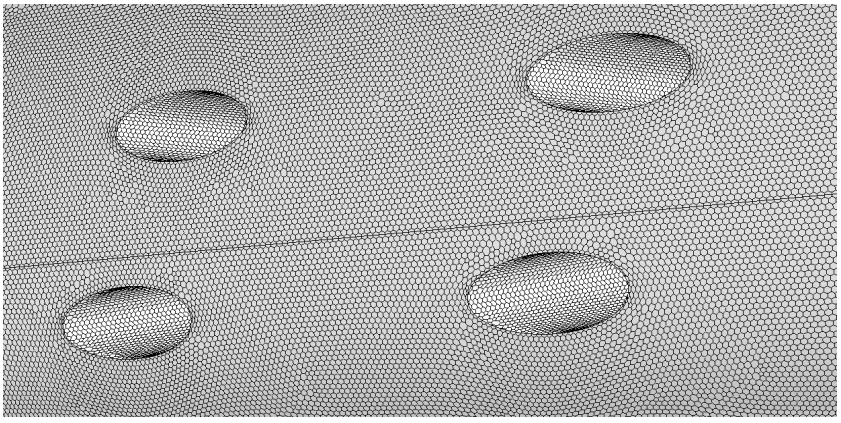

Figure 4.19: Surface mesh on the leading edge and inside the cooling holes

are made coarser to limit the computational cost.

The y^+ value on the surface inside the cooling holes and on the vane surface is ensured to be below 1. The thickness of the first layer on the wall is 7×10^{-7} m in the region of cooling holes and the leading edge. The computational mesh of 27 million cells is implemented in the RANS simulations. The results of the mesh sensitivity study are presented in Section 4.2.3. The residuals are aimed to be below 1×10^{-6} which is a criterion mostly achieved in simulations. Energy residual and, in swirling flow simulations, the y-axis momentum equation residual are obtained below 1×10^{-4}. An additional simulation of an uncooled cascade is performed with an extended outlet to confirm the solution independence of outlet placement.

Following the results of the literature review, the realizable $k - \varepsilon$ model is implemented for the film cooled vane. Alternatively, the lag EB $k - \varepsilon$ model is also applied to RANS simulations since the results were found to match closely to the realizable $k - \varepsilon$ prediction. The transient hybrid RANS-LES simulations are performed with the lag EB model for regions with RANS formulation. The SST $k - \omega$ model is not preferred in problems involving mixing between multiple jets and evaluating film cooling effectiveness, as explained in Section 2.3. A preliminary analysis with the SST model resulted in a

considerably different flow field when compared to RKE and lag EB model solutions.

Scale resolving hybrid simulations

Scale resolved hybrid model is applied to investigate the benefits of hybrid LES-RANS modelling as compared to the steady-state RANS simulation. A transient simulation is performed with the steady-state RANS result as an initial solution. The hybrid model is equipped with the lag EB turbulence model in the regions where RANS formulation is implemented. The lag EB model is chosen since it has improved near-wall treatment as compared to the RKE model which has been extensively used in the literature on film cooling problems as explained in Section 2.3. In addition, both models provided similar results in terms of adiabatic cooling effectiveness in RANS simulations, as reported in Section 5.2.1. In order to capture the unsteady behaviour in the mixing between coolant jets and the mainstream gas, the CFL number in the whole leading edge region is kept below unity. A timestep of 4×10^{-7} s is implemented. One flow-through in this case is defined as a time for a coolant particle to flow through the entire cooling channel. After a start-up time of around 2000 time steps, at least ten flow-throughs are simulated.

The temporal and spatial resolution are investigated retrospectively during the simulation. The hybrid simulation allows for the investigation of the RANS regions and scale-resolved regions. The aim is to resolve at least 80% of the turbulence kinetic energy in the leading edge region. The modelled-to-resolved energy ratio is investigated to satisfy this criterion. If the spatial resolution is insufficient in a specific region on the leading edge or slightly downstream, then the mesh is refined further in that particular region. For example, additional refinement was required in the regions close to the vane surface just downstream of the leading edge where the volumetric mesh control did not extend. The mesh that is implemented in RANS simulations is used at the beginning when running SRH simulation. Similarly, the timestep can be adjusted if the CFL criterion is not met. The total duration of computational time to simulate ten flow-throughs was around a week using 140 cores.

4.2.2. Cooling parameter and swirl definitions

Adiabatic film cooling effectiveness is defined in Equation 4.4.

$$\eta = \frac{T_{aw} - T_\infty}{T_c - T_\infty} \tag{4.4}$$

The parameters T_∞ and T_c are constant mass flow-averaged quantities over the mainstream and coolant inlets, respectively. T_{aw} is obtained when the wall is modelled as adiabatic. The blowing ratio is an important parameter in film cooling problems. The definition is provided in Equation 4.5. The coolant mass flow $\dot{m}_c$ and cross-section area A_c represent the total values summed-up over all cooling holes, i.e. $A_c = \sum_i^n A_i$ where n is the number of cooling holes.

$$BR = \frac{\dot{m}_c / A_c}{\dot{m}_\infty / A_\infty} \tag{4.5}$$

The adiabatic model allows for an investigation of the coolant coverage and interaction between mainstream and coolant jets. However, an adiabatic model does not allow for an investigation of heat transfer. There would be an enhanced convective heat transfer in the regions of high mixing that would generate strong turbulence. Furthermore, the coolant inside the channels is cooling the walls of those coolant channels. The vane would also be cooled in the leading edge region through conduction since the vane structure is connected to the coolant channels. Hence, these factors are disregarded, and the analysis is focused on film cooling effectiveness.

Inlet swirl profiles

In modern gas turbines, the swirlers help to stabilise the flame in the combustion chamber. However, often the swirling motion is conserved when flow enters the NGV. The motivation for applying a swirling profile is to investigate how it affects the showerhead film cooling performance. The swirl intensity is characterised in Equation 4.6 as a ratio between tangential and axial velocities. This is a simplified expression as compared to swirl number [18] but it can be effectively used to compare various swirl

profiles. A swirl number is a parameter commonly used to characterise swirl strengths but it is based on a swirler geometry. A cylindrical coordinate frame with origin at the center of the inlet is used to obtain the averaged velocity values over the inlet for Equation 4.6. Furthermore, a swirl introduces an additional secondary flow structure and it is expected that aerodynamic loss is increased. In addition, the mixing between coolant and the mainstream is a major loss source, present for both no-swirl and swirling flow inlet cases. The loss is compared between multiple swirling profiles in terms of the total pressure loss by implementing the definition of aerodynamic row efficiency [18, 135], shown in Equation 4.7.

$$S_n = \frac{U_{tan}}{U_{ax}} \tag{4.6}$$

$$\eta_{row} = \frac{1 - (\frac{P_{out}}{P_{t,out}})^{\frac{\gamma-1}{\gamma}}}{1 - (\frac{P_{out}}{P_{t,in}})^{\frac{\gamma-1}{\gamma}}} \tag{4.7}$$

Two swirling profiles are applied to the inflow. The first profile is created by simulating a channel flow with a circular swirl imposed on its inlet. Then the obtained profile is extracted downstream with a swirl intensity of 0.17, or 17%. The profile is shown in Figure 4.20. The second profile is extracted from a simulation of a non-reacting combustor, and it is visualised in Figure 4.21. It has a considerably higher swirl intensity of 75%. Both profiles have a swirl core aligned to the leading edge of the vane. For reference, swirling flow with a swirl number below 0.30 in a burner is considered a weak swirl, and above 0.6 a strong swirl [136].

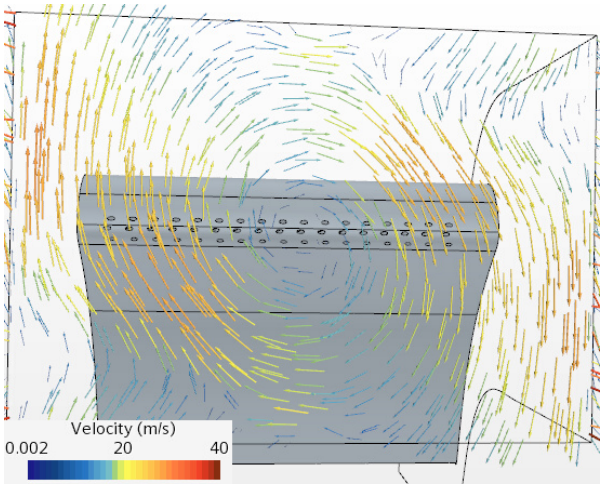

Figure 4.20: Tangential velocity vectors at the inlet, swirl intensity of 17%.

The non-reacting combustor simulation is obtained from the FACTOR project simulation [137]. The flow case consists of a non-reacting annular combustor simulator coupled with a swirler [17]. The studies were focused on analysing turbine-vane interaction. The total pressure, total temperature, and flow velocity components are extracted at the inflow of the nozzle guide vane. The aim of extracting this profile is to apply a swirling inflow with a matching hot-streak at the inlet to analyse the effect on showerhead film cooling performance. Notably, the geometry of the vane and the flow channel is not replicated exactly from the FACTOR simulation. Therefore, the focus is on drawing analysis of the effect of flow variables, such as swirl, rather than simulating a fully realistic turbine configuration.

There are some limitations that shall be addressed, regarding the application of the FACTOR swirl profile. Firstly, the simulation of the FACTOR consisted of two vanes downstream of a combustor with a periodic boundary applied on the edge of the domain, instead of one vane as in the CFD model of the current study. Hence, the geometry of the channel is wider (two vanes vs one) and the periodicity is different. A decision was made to extract a part of the inlet profile from FACTOR simulation, corresponding to a portion consisting of a complete swirl profile with the swirl core located at the center of the section. Therefore, the periodicity is altered, however, a complete swirling rotation is captured as

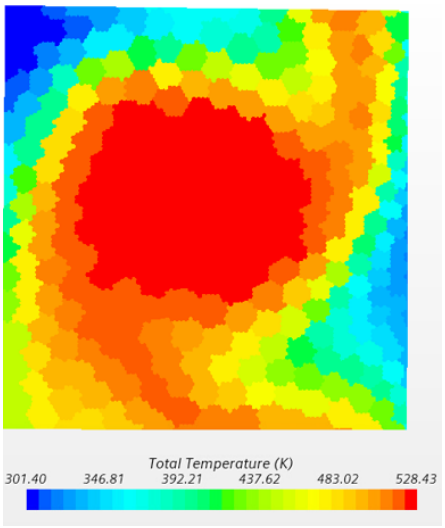

(a) Total temperature profile at the inlet.

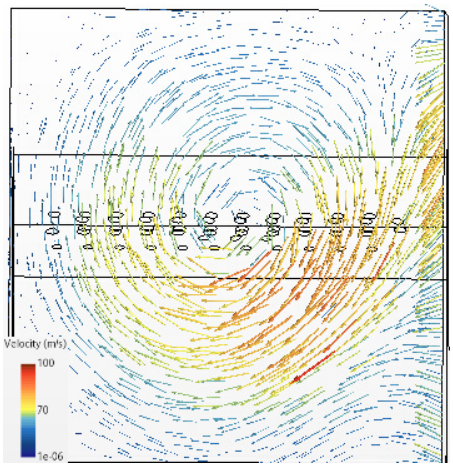

(b) Tangential velocity vector components at the inlet with vane leading edge shown in the background.

Figure 4.21: Inlet hot-streak and swirl profile derived from FACTOR inflow.

visualised in Figure 4.21b. The swirl core is leading-edge-aligned without the possibility to investigate the passage-aligned swirl due to the periodicity of the domain. Secondly, the vane span is shorter in FACTOR geometry. In order to preserve the swirl profile, it is decided to shorten the span of the showerhead CFD model for analysis of this particular flow case. In addition, the flow angles are not matched. For the FACTOR inflow the mass flow averaged total pressure at the inlet $P_{t,\infty}$ = 151 413 Pa, outlet Mach number is kept around $Ma_{is,out}$ = 0.90. The coolant-to-mainstream total temperature and total pressure ratios are maintained as in the other simulations, $T_{t,\infty}$ = 459.3 K and $T_{t,c}$ = 320 K. The blowing ratio is increased to $BR = 1.90$ to ensure that hot gas ingestion is avoided.

4.2.3. Mesh sensitivity study - film cooled vane

The computational mesh is refined for mesh independence study, and two additional configurations are made. First, the base size of the cells in the entire domain is reduced by a third, and the first cell width on the wall is reduced by 25% (labeled as 'Refined mesh'). The second configuration consists of mesh refinement exclusively at the leading edge region and the cooling holes ('Refined LE'). The cell size in the volumetric control is refined by half, and the prism layer is refined similarly to the first configuration. Finally, after observing a mesh-independent solution for refined meshes, a coarser mesh is added. For this configuration, the resolution in the leading edge region and inside the holes is slightly reduced. The base cell size in the region is increased by 10%, and prism layer first layer thickness increased up to 1×10^{-6} m whilst ensuring y^+ value below 1. The realizable $k - \varepsilon$ turbulence model is implemented. To show mesh independence the adiabatic wall temperature is plotted at the leading edge on the cross-section of the vane. The location where the temperature is obtained is shown in Figure 4.22b. The temperature variation on the whole leading edge section is provided in Figure 4.22a.

Results indicate that mesh independence is achieved. The coolant coverage predicted by the three simulations is evidently similar as reported in Figure 4.23. The area-averaged cooling effectiveness is compared in Table 4.7 and it varies within 1%. The averaging is performed on the suction side and pressure side areas ("SS" and "PS" in Figure 4.24) of the leading edge.

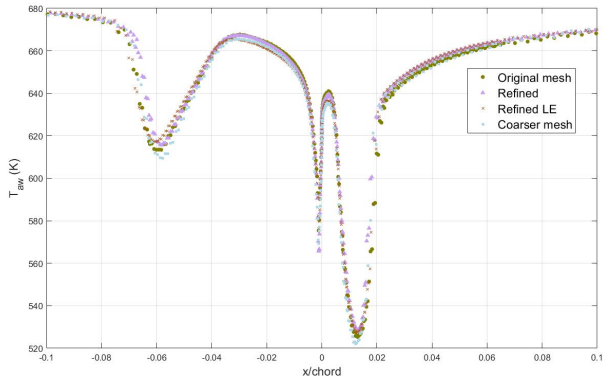

(a) Adiabatic temperature distribution on the leading edge with four different meshes

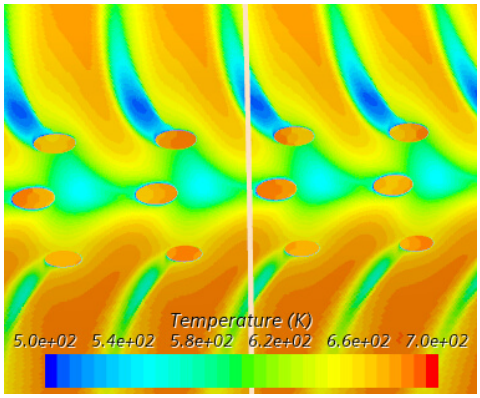

(b) Location of adiabatic temperature comparison

Figure 4.22: Comparison of temperature distribution on the vane leading edge between RANS simulations with various mesh sizes.

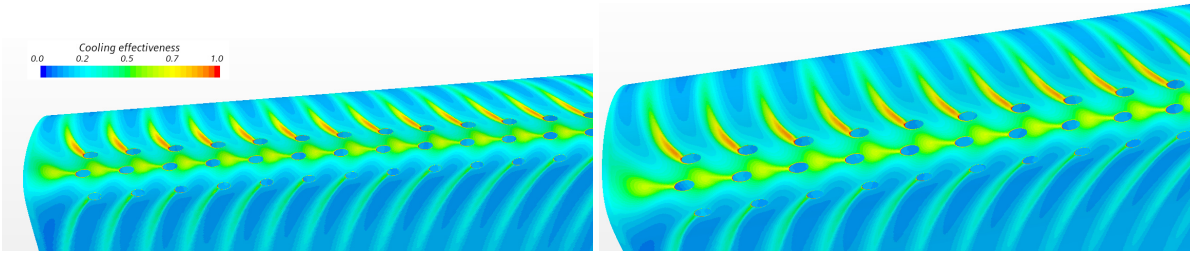

(a) Original mesh

(b) Refined mesh

Figure 4.23: Adiabatic cooling effectiveness on the vane leading edge

Table 4.7: Mesh independence study. A comparison of predicted blowing ratios and area-averaged cooling effectiveness values. and

	Original mesh	Refined mesh	Refined LE	Coarser mesh
Number of cells	33.5 million	63.8 million	71.1 million	26.6 million
η_{avg} on ”PS”	0.236	0.234	0.239	0.243
η_{avg} on ”SS”	0.300	0.298	0.302	0.303
BR	1.385	1.408	1.394	1.410

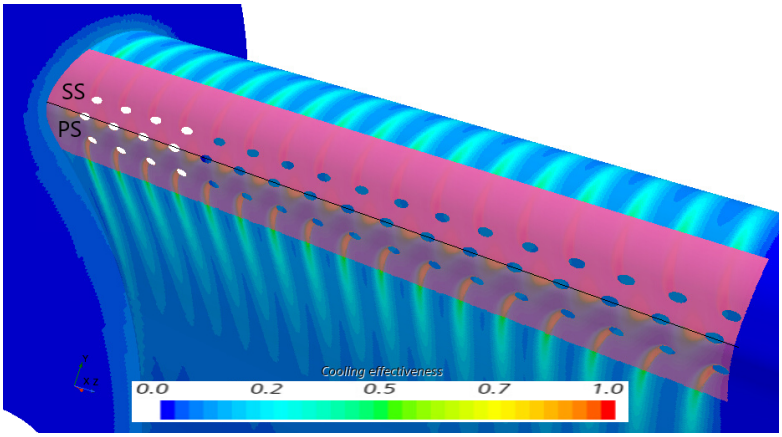

Figure 4.24: The areas ”PS” and ”SS” on the vane leading edge over which the area-averaged cooling effectiveness values are obtained

5

Results

The results section is split into two parts. First, the results are presented for the validation case in Section 5.1 and then for a film-cooled vane in Section 5.2.

5.1. Validation case

The CFD results together with a comparison to experimental data are provided first for the cases of higher Reynolds number at the inlet ($Re_x = 1.0 \cdot 10^6$ for cases F and H), then for the lower $Re_x = 0.5 \cdot 10^6$ for cases A and C. The presented cases provide the information to analyse the effects of the three flow variables of the experiment, which are the inlet turbulence intensity, Reynolds number, and outlet Mach number. The results of the four remaining cases (Case B,D,E,G) are placed in Appendix A.

5.1.1. $Re_x = 1.0 \cdot 10^6$ cases

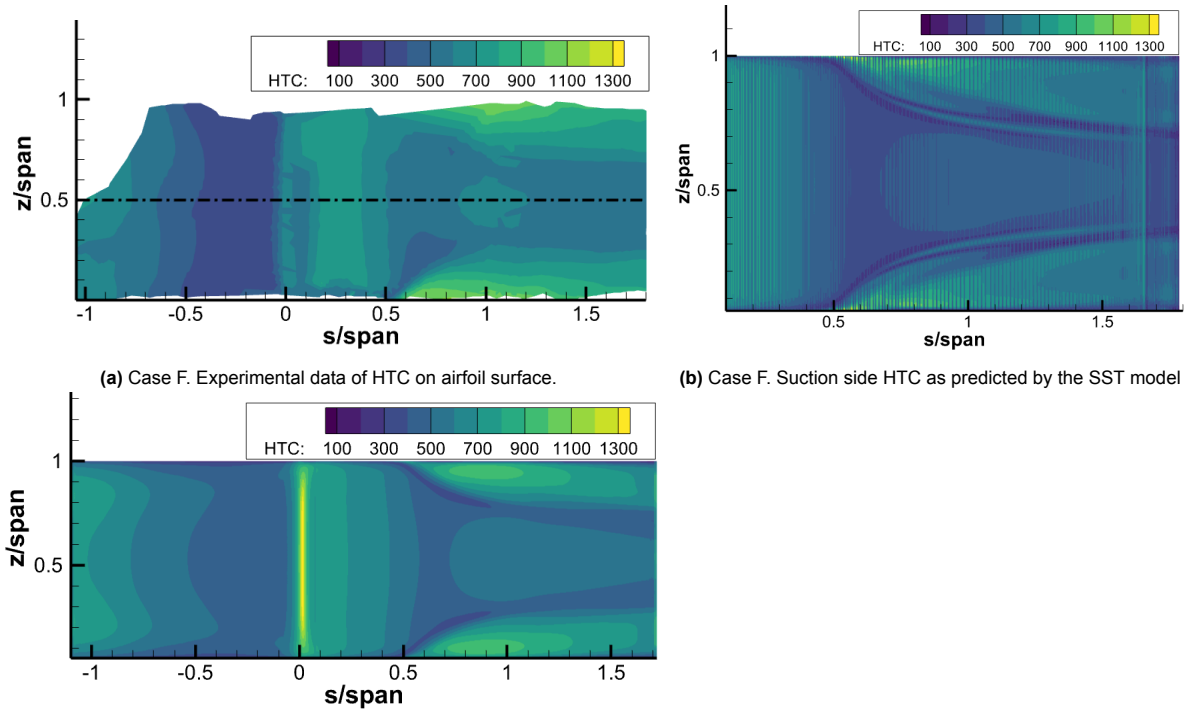

(a) Case F. Experimental data of HTC on airfoil surface.

(b) Case F. Suction side HTC as predicted by the SST model

(c) Case F. HTC distribution on airfoil surface as predicted by the lag EB model.

Figure 5.1: Case F (Tu=8%), HTC distribution on the airfoil surface. SST model predicts an additional streak of high HTC between the endwalls and the midspan. The lag EB model prediction agrees better with the experimental data on the suction side.

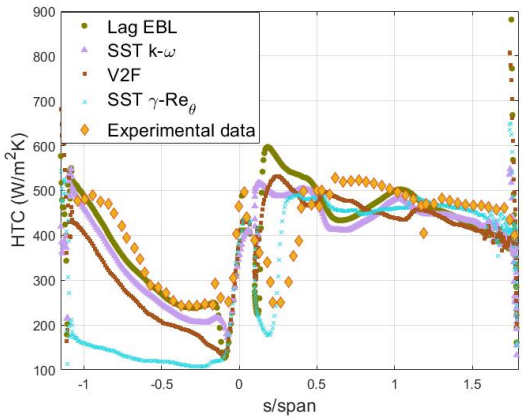

(a) Case H midspan, $Tu = 0.50\%$

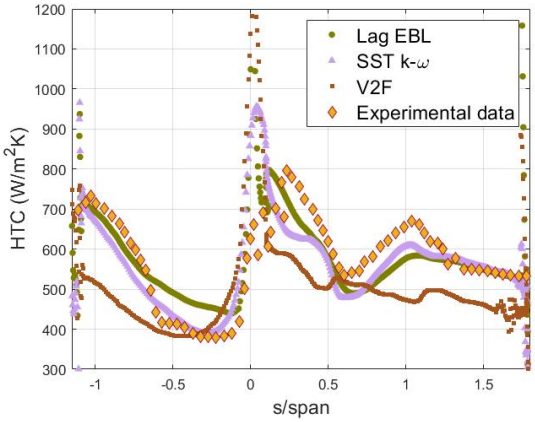

(b) Case F midspan, $Tu = 8\%$

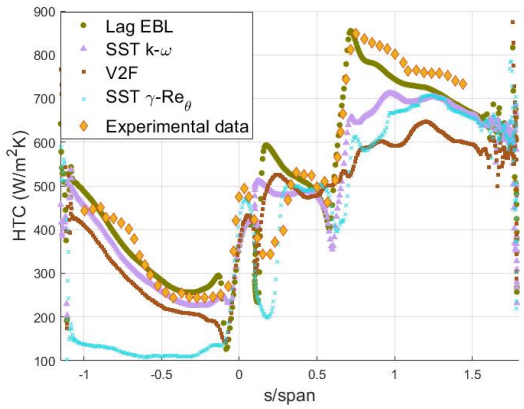

(c) Case H 10% span, $Tu = 0.50\%$

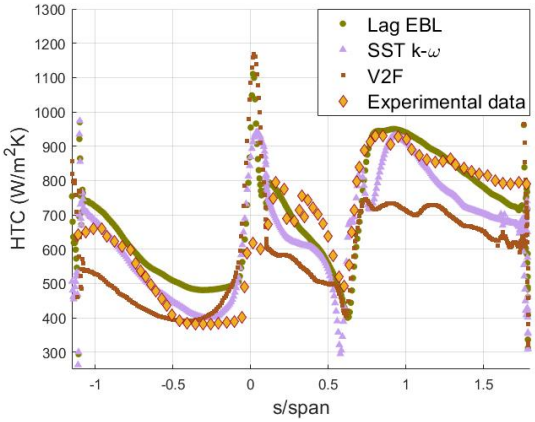

(d) Case F 10% span, $Tu = 8\%$

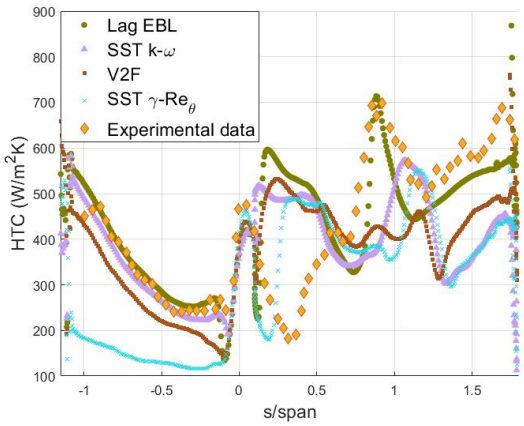

(e) Case H 25% span, $Tu = 0.50\%$

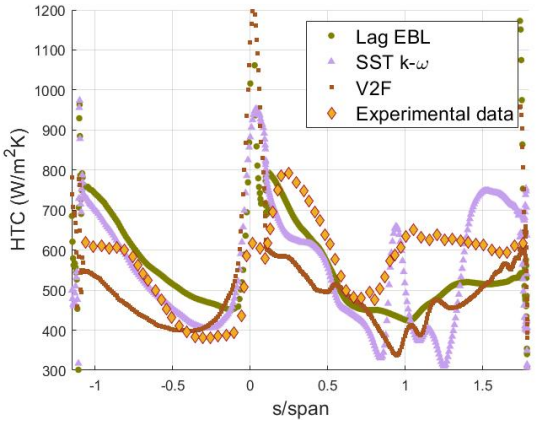

(f) Case F 25% span, $Tu = 8\%$

Figure 5.2: $Re = 1.0 \cdot 10^6$, $Ma_{out} = 0.98$. HTC along the curvilinear distance on the airfoil surface at various span locations. Results show the lag EB model being superior in estimating secondary flow HTC enhancement on the suction side, especially in the low turbulence intensity case. A transition model is required to capture transition location on the low turbulence intensity case H, Kelterer correlation is implemented for the $\gamma - Re_\theta$ model. Overprediction of HTC at the leading edge for case F by all models.

The HTC values on the complete airfoil surface are shown in Figure 5.1 for the case with 8% turbulence intensity. The predicted HTC values at different locations along the airfoil span are displayed in Figure 5.2 for two subsonic flow cases. Evidently, the pressure side HTC predictions The curvilinear distance along the airfoil surface s is normalised over a length of the blade span and placed on the horizontal axis. For the suction side $s/span > 0$, and for the pressure side $s/span < 0$.

Only the cases with low turbulence intensity $Tu < 0.5\%$ experience a considerable portion of the suction side boundary layer in a laminar state. Therefore, the transition model is not implemented in high turbulence intensity flow cases. A simulation without transition model improves the underpredictions by the $\gamma - Re_\theta$ in the regions where the transition model wrongly predicts a completely laminar boundary layer, e.g. on the pressure side. The Kelterer correlation for transition parameters is implemented since the Suluksna-Juntasaro correlation predicted a transition onset too far downstream. However, it should be noted that the reported dots of paint interfered with the transition prediction in low turbulence case H.

The HTC enhancement on the suction at 10% and 25% of the span is associated with the secondary flows impinging on the wall. In this region, the lag EB model provides the best agreement with the experimental data as shown in Figure 5.2d, Figure 5.2c and Figure 5.2e. However, all of the models correctly captured the location where the HTC starts to increase on the suction side. The SST model provides a closer agreement to the experiment as compared to the $\overline{v^2} - f$ model which underpredicts the HTC enhancement due to secondary flows. However, the SST model predicts an additional streak of high HTC in the high turbulence intensity case F, as observed in Figure 5.1. This streak is associated with the trace of the suction side leg of the horseshoe vortex which was observed in the low turbulence intensity cases in the experiment. All three RANS models overpredicted the stagnation point HTC for the high turbulence intensity case F, the SST model overprediction is the smallest.

5.1.2. $Re_x = 0.5 \cdot 10^6$ cases

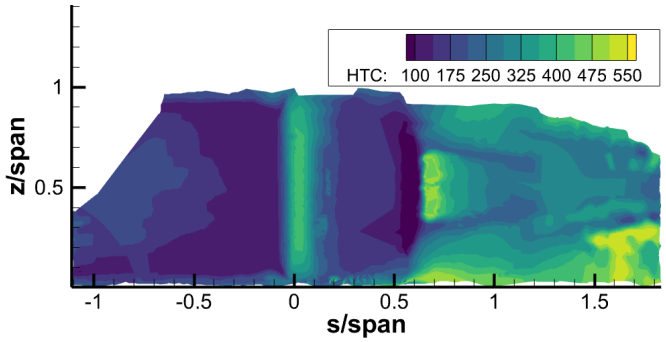

(a) Case D. Experimental data of HTC on airfoil surface.

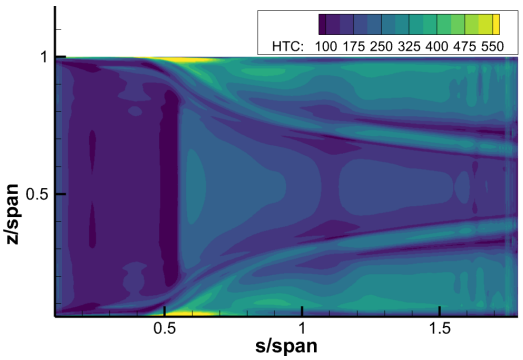

(b) Case D. Suction side HTC as predicted by the SST $\gamma - Re_\theta$ model

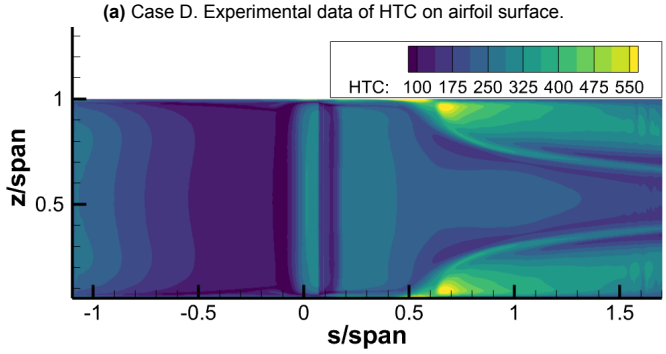

(c) Case D. HTC distribution on airfoil surface as predicted by the lag EB model.

Figure 5.3: Case D (Tu=0.25%), HTC distribution on the airfoil surface. SST $\gamma - Re_\theta$ model accurately predicts the transition onset at $s/span = 0.6$ whilst the lag EB model prediction misses it. Both models predict the suction side leg of the horseshoe vortex impinging on the wall, the second streak of enhanced HTC can be distinguished only vaguely in experimental data. The lag EB model prediction agrees slightly better with the experimental data in the region $s/span > 0.5$ close to endwalls due to a stronger HTC enhancement.

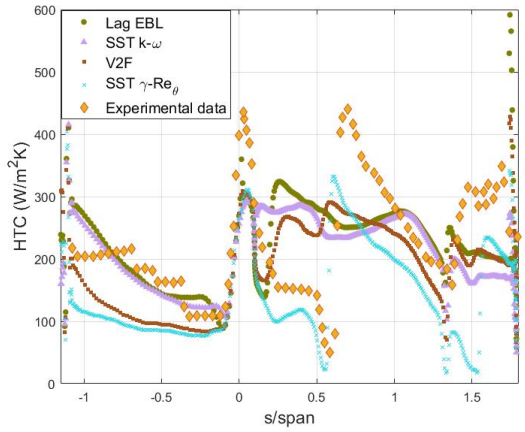

(a) Case C midspan, $Tu = 0.25\%$

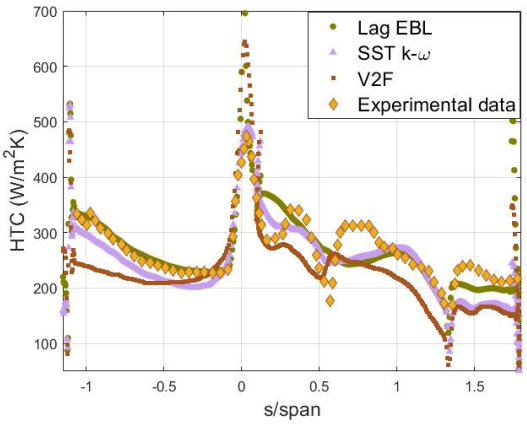

(b) Case A midspan, $Tu = 8\%$

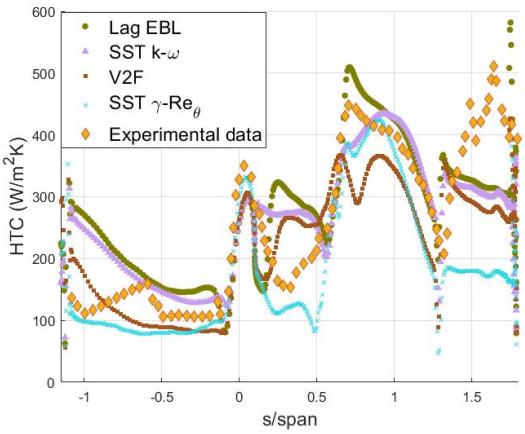

(c) Case C 10% span, $Tu = 0.25\%$

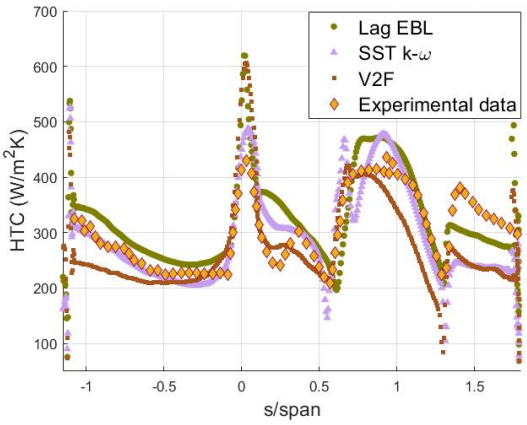

(d) Case A 10% span, $Tu = 8\%$

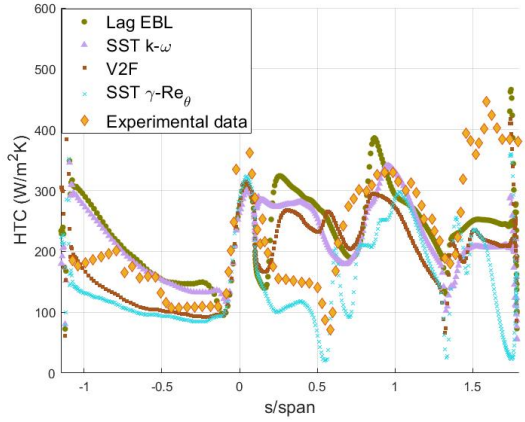

(e) Case C 25% span, $Tu = 0.25\%$

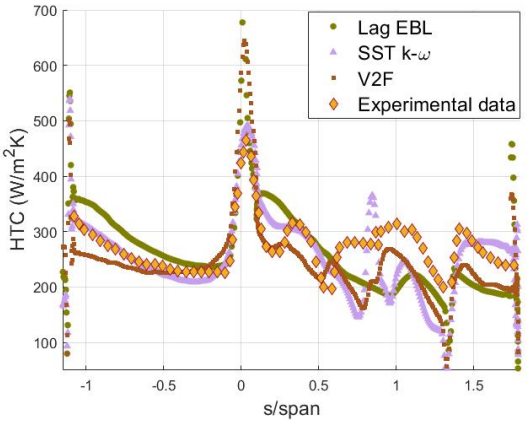

(f) Case A 25% span, $Tu = 8\%$

Figure 5.4: $Re = 0.5 \cdot 10^6$, $Ma_{out} = 1.30$. HTC along the curvilinear distance on the airfoil surface at various span locations. Suluksna-Juntasaro correlation (default in *Star-CCM+*) is implemented for $\gamma - Re_\theta$ model. The transition model accurately predicts transition onset, also the high turbulence case has an early transition onset which is predicted by the $\gamma - Re_\theta$ model.

For low Reynolds number cases, it is observed that the transition onset is further downstream as compared to the $Re_x = 1.0 \cdot 10^6$ flow cases as observed in Figure 5.3c. This agrees with the theory and experimental data from Giel. The supersonic flow cases A and C are displayed in Figure 5.3 where the HTC enhancement at around $s/span = 1.4$ is associated with the shock wave location. The transition onset predicted by the SST $\gamma - Re_\theta$ model with Suluksna-Juntasaro correlation has moved negligibly

further downstream by 0.01c_x, as compared to the case H where the model predicted significantly too late transition. It is noted that case C ($Re_x = 0.5 \cdot 10^6$) in the experiment was not affected by the reported dots of paint, as opposed to the case H ($Re_x = 1.0 \cdot 10^6$). The difference between transition onset locations in case H and case C is evident in experimental data, similarly as predicted with Kelterer correlation. In $Re_x = 0.5 \cdot 10^6$ cases, the $\gamma - Re_\theta$ model transition predictions match with both Kelterer and Suluksna-Juntasaro correlations. Notably, in $Re_x = 0.5 \cdot 10^6$ cases (Figure 5.4) there is a clear transition predicted by $\overline{v^2} - f$ and lag EB models slightly downstream of the trailing edge as well, however, it is considerably differing from the actual transition onset recorded in the experiment at around $s/span = 0.5$ as shown in Figure 5.4a.

Transition location seemingly forms the biggest difference when comparing $Re_x = 0.5 \cdot 10^6$ to $Re_x = 1.0 \cdot 10^6$ cases. Apart from that, the HTC on midspan and other regions is simply reduced or scaled down, as is expected for a lower Reynolds number flow. Notably, the stagnation HTC is not overpredicted by the SST model in the $Re_x = 0.5 \cdot 10^6$ and high turbulence cases, as opposed to $Re_x = 1.0 \cdot 10^6$ cases. Similar to the $Re_x = 1.0 \cdot 10^6$ cases, all RANS models capture the enhancement of HTC due to secondary flows impinging on the suction side wall. Furthermore, an additional streak of high HTC close to midspan in Figure 5.3c is observed in experimental data, and it is predicted by both SST and lag EB models. The lag EB prediction provides the closest agreement to experimental data in low turbulence case C (Figure 5.4c) at $0.5 < s/span < 1$ where secondary flow impinges on the wall at 10% of spanwise location. The HTC values downstream of the shock are underpredicted by all three RANS models.

5.1.3. Difference in horseshoe vortex modelling between lag EB and SST models

As shown in Figure 5.1 and Figure 5.3, the HTC pattern on the vane suction side is largely influenced by secondary flows. The vortices impinge on the vane surface, increasing the HTC locally. However, the predicted HTC pattern slightly differs between the SST $\gamma - Re_\theta$ and lag EB models. The additional streak of enhanced HTC is often visible for SST model (Figure 5.1b) between midspan and the location where the passage vortex impinges on the surface. The additional enhancement, which is also present in the experimental data, is associated with the suction side leg of the horseshoe vortex, therefore, the horseshoe vortex system is explored in more detail. The modelling differences stem from horseshoe vortex calculations. Case F is used to compare the modelled horseshoe vortex system between SST $\gamma - Re_\theta$ and lag EB models. As shown in Figure 5.5a, the SST model predicts the system consisting of four separate vortices, as visualised by Q-criterion isosurfaces. Meanwhile, the lag EB model predicts one distinguished vortex (Figure 5.5b) or, at most, two when an additional corner vortex appears in low-turbulence case. This is also the reason why the SST suction side HTC pattern has the extra streak of enhanced HTC, which is not recorded by the lag EB model in either low or high turbulence cases. It corresponds to one of the horseshoe vortex structures impinging on the suction side of the vane.

There is high eddy viscosity at the core of a vortex, responsible for enhancing HTC when the vortex impinges on the wall. A modelling difference between lag EB and SST is also apparent when analysing the region on the suction side where the secondary flows start to affect the HTC distribution. As shown in Figure 5.6b with streamlines seeded from the endwall, a spot of large turbulence kinetic energy is present where a vortex impinges on the suction side of the airfoil for SST $k - \omega$ simulations. The peak turbulent kinetic energy is larger as compared to the lag EB model (Figure 5.6a). However, downstream of that peak location on the suction side, the turbulent kinetic energy value quickly reduces and the lag EB model predicted flow field has a higher turbulent kinetic energy. In general, the turbulence kinetic energy pattern on the vane surface is similar to the HTC pattern since the heat transfer calculations incorporate turbulence kinetic energy term, as explained in Section 3.5. It is noted that the lag EB model includes the transport equation for anisotropy measure or 'reduced stress function' ϕ, and, according to Equation 3.23, it is also included in the equation for eddy viscosity. Therefore, the anisotropy can play a role in HTC calculations, especially in this location where the secondary flow field is estimated. Turbulence prediction is likely overestimated by the SST model at a location where a vortex impinges on a wall since the Reynolds stress and strain components can be misaligned there. As found by investigating lag EB model flow field, the reduced stress function ϕ is low at the impingement location, suggesting

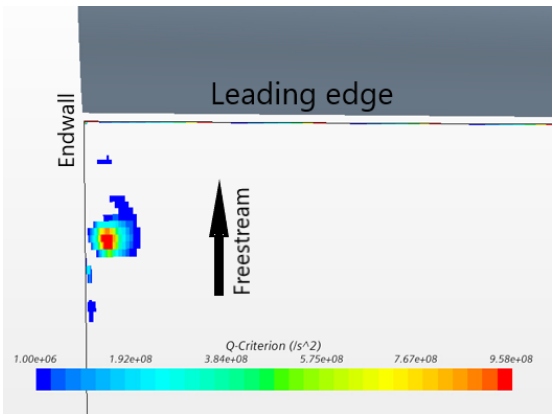

(a) Positive Q-criterion values upstream of the leading edge. Modelling of horseshoe vortex structure. SST $k-\omega$ model

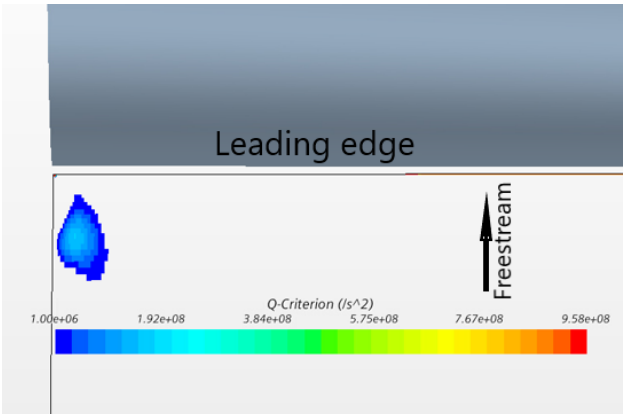

(b) Positive Q-criterion values upstream of the leading edge. Modelling of horseshoe vortex structure. Lag EB model.

Figure 5.5: Q-criterion upstream of the vane leading edge.

a high anisotropy. In such locations, SST model is prone to overestimate turbulence kinetic energy [64].

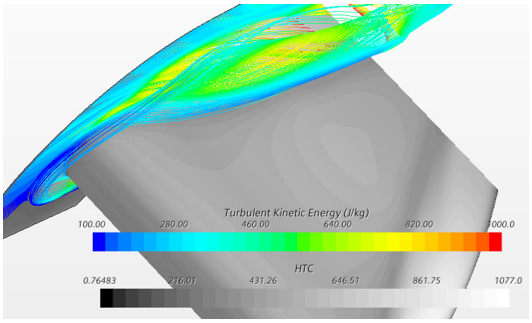

(a) HS vortex bending around passage vortex. Case F, lag EB model

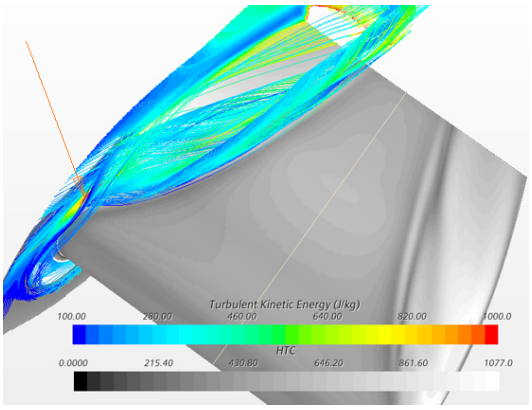

(b) HS vortex bending around passage vortex. Case F, SST model. An arrow indicates a region of high turbulent kinetic energy where the vortex impinges on the vane surface.

Figure 5.6: Streamlines seeded from the endwall show the suction side leg of the horseshoe vortex bending around the passage vortex.

5.1.4. SST $\gamma - Re_\theta$ with constitutive relations and crossflow transition term

Applying constitutive relations for the SST model is deemed to improve accounting for turbulence anisotropy, as described in Section 3.5.1. High turbulence Case F and Case E were simulated with quadratic and cubic relations applied and without a transition model. The quadratic relation provided results without considerable discrepancies from the linear constitutive relation when applied to the SST model. The cubic relation incorporates a slightly modified equation for the eddy viscosity but the predicted HTC distribution is only slightly affected. In general, the similarities in the predicted HTC distribution were apparent when compared to SST simulations without non-linear constitutive relations applied. The cubic relation leads to a slightly larger HTC enhancement due to secondary flows at 10% of the span, the maximum HTC value 4%-6% higher at that location. The simulation with the cubic relation was more robust, and the unsteady horseshoe vortex and its impingement on the suction side were resolved more consistently. The residuals progressed orderly with fewer oscillations. Provided that anisotropic turbulence is of importance and convergence is reached, it is recommended to implement the cubic relation for SST simulations. Regarding the curvature correction, no significant differences were observed when implementing this parameter. The stagnation point HTC was increased by 4%, resulting in an even larger overprediction

Crossflow transition

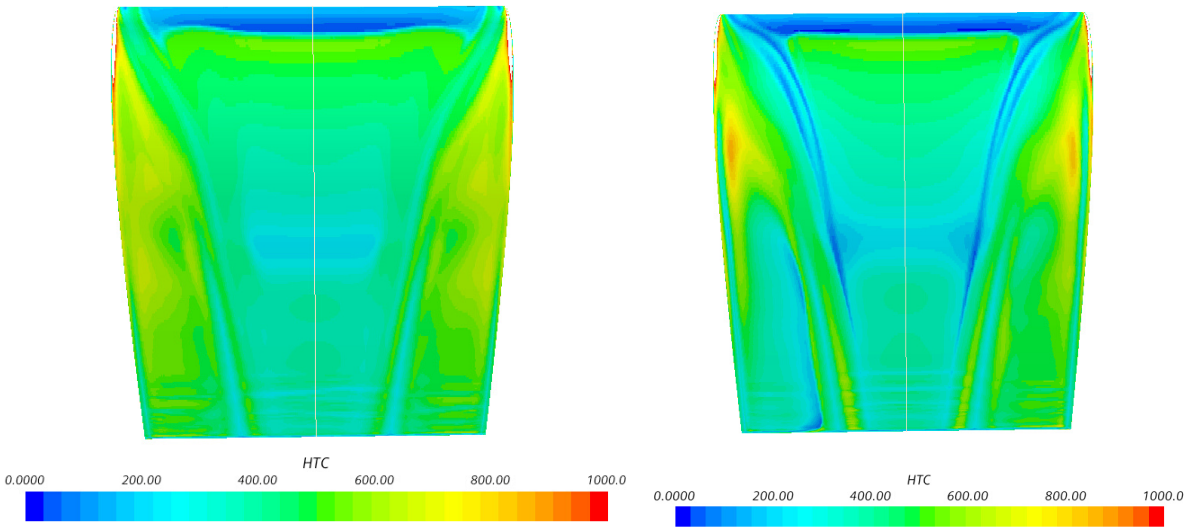

(a) Crossflow transition term enabled

(b) The original $\gamma - Re_\theta$ without crossflow term

Figure 5.7: Case H. HTC distribution on the suction side of the airfoil with and without the inclusion of crossflow term in the $\gamma - Re_\theta$ transition model ($Tu = 0.5\%$). The differences are obtained in the areas where the secondary flow field interferes with the transition location. Crossflow term inclusion achieves a closer agreement with the data, by ensuring a slightly smoother transition and avoiding the streaks of extremely low HTC rates.

Considering that the secondary flow field is affecting the HTC distribution on the suction side close to the endwalls, the $\gamma - Re_\theta$ transition model incorporating the crossflow transition term is tested. Firstly, no noticeable effect is observed in the high turbulence ($Tu_{in} = 8\%$) cases. This is expected in the cases with $Tu_{in} = 8\%$ where either no transition or very early transition was observed on the suction side of the vane. The boundary layer is already in a turbulent state, and the transitional model does not play a significant role in flow field calculations. An effect of the crossflow term is observed in case H where $Tu_{in} = 0.5\%$, and the boundary layer is laminar for a considerable portion of the vane suction side surface. The HTC distributions on the pressure side along the whole span and the suction side at midspan are predicted similarly with negligible discrepancies when compared to the original SST $\gamma - Re_\theta$ model. In these regions, there is no crossflow either. However, the flow field is affected due to secondary flows close to endwalls. The simulation results are displayed in Figure 5.7 for case H ($Tu_{in} = 0.5\%$, $Ma_{out} = 0.98$). The low HTC lines in a streamwise direction close to midspan represent the locations where the vortices are separating from the surface. By enabling the crossflow transition term, the extremely low HTC values at those separation locations are avoided. Hence, the agreement with the experimental data shown in Figure 5.2c is improved as well. The benefit of the crossflow term is observed only when the transition occurs sufficiently downstream in the region where secondary flows attach tn the vane surface.

5.1.5. Different correlations for $\gamma - Re_\theta$ transition model

The performance of $\gamma - Re_\theta$ model correlations is investigated in low inlet turbulence intensity flow cases with high Reynolds number (Case H), and the low Reynolds number flow case D. In high turbulence intensity flow cases, the transition model was not required and all implemented correlations resulted in similar HTC distributions. Transition parameter correlations by Suluksna-Juntasaro (default option in *Star-CCM+*), Kelterer et al. [130] and Sorensen [128] are compared in low turbulence case H. The correlations are applied for $Re_{\theta,c}$ and F_{length}. The following simulations are performed with the crossflow term enabled. A more detailed description of different correlations is in Section 3.5.2.

Case H

Different correlations greatly affect the transition onset in low turbulence Case H as shown in Figure 5.8a. It is observed that the Suluksna-Juntasaro predicts the transition onset too far downstream as compared to the experimental data. Furthermore, the transition is too sharp, meaning that the production of intermittency is strong with a large value of F_{length}. Kelterer et al. correlation achieves an accurate transition onset. The transition length is still too short, however, it is slightly longer as compared to Suluksna-Juntasaro and Sorensen correlations. The pressure side HTC is underpredicted when coupling the transition model to the SST turbulence model, irrespective of the applied correlation. The secondary flow pattern and HTC enhancement towards the trailing edge are calculated more accurately with the Kelterer et al. correlation once again. However, it must be noted that in the experiment transition was affected by the dots of paint on the suction side surface at $s/span = 0.33$ [8]. The transition onset is moved forward, and the dots were painted at 50%, 33% and 67% spanwise locations. Further away from the dots at a 10% span, the transition onset is still predicted too far downstream by Suluksna-Juntasaro correlation as shown in Figure 5.8b. Although, the dots are still likely to have affected the flow field.

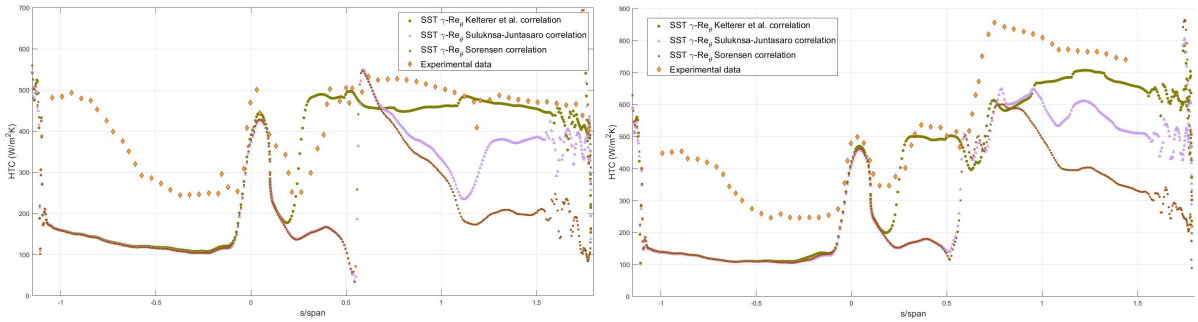

(a) HTC at midspan **(b)** HTC at 10% span

Figure 5.8: HTC results for Case H. Kelterer correlation improves transition onset prediction.

Case D

The Suluksna-Juntasaro correlation was created based on a flow over a flat plate with Re at inlet varying between $1.8 \cdot 10^5$ to $5.6 \cdot 10^5$ which is below the Reynolds number for Case H. Flow case D has an inlet $Re = 5 \cdot 10^5$ and the dots of paint on suction side surface did not interfere with the experimental results. As shown in Figure 5.9a, the performance of Suluksna-Juntasaro correlation has improved. The transition onset is predicted accurately. Kelterer et al. correlation provides a similar transition onset prediction as well. The transition length is again predicted to be very short, in low Re flow cases it corresponds to the transition length in experimental data.

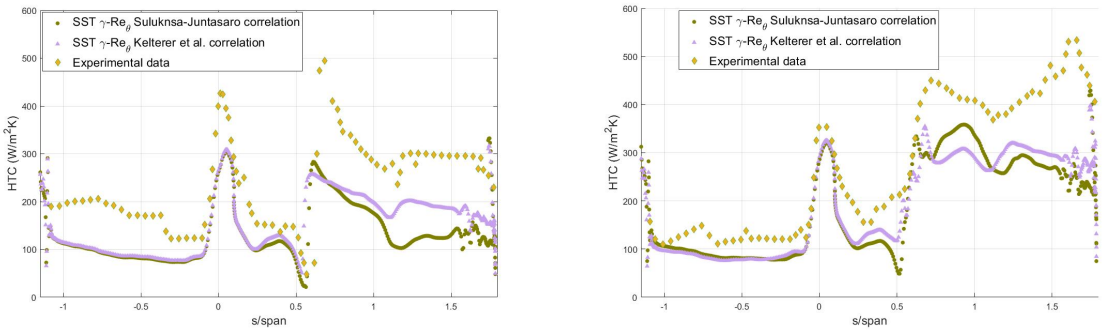

(a) HTC at midspan **(b)** HTC at 10% span

Figure 5.9: Case D, $Re = 0.5 \cdot 10^6$, $Tu = 0.25\%$. Low Reynolds number flow case results in Suluksna-Juntasaro and Kelterer correlations predicting a similar transition onset that matches the transition location in the experiment. The HTC values in the turbulent boundary layer are underestimated

5.1.6. Scale resolving hybrid model results

A transient simulation with the SRH model is performed to capture the unsteadiness of the horseshoe vortex. Considering the current mesh spatial resolution and time resolution, the SRH simulation is treating regions close to the walls with RANS formulation and the bulk flow predominantly with LES.

The suction side HTC close to endwalls is largely varying as shown in Figure 5.10, signifying the unsteadiness of secondary flow. The HTC results at the vane midspan are invariant in time. However, the general trend of results is similar to RANS simulation results. The HTC enhancement is apparent close to endwalls on the suction side of the vane. The largest HTC enhancement is at the location where vortices attach to the wall. Closer to the trailing edge, the vortices start to dissipate and a lift-off from the surface can occur as well. In those regions, the HTC values are reduced. However, the unsteadiness leads to time-dependant HTC distributions. Notably, the turbulence conditions at the inlet for the scale resolving simulation were not matched to the Giel experimental case. Therefore, a direct comparison to the steady-state experimental data is not performed since the HTC results are strongly tied to the freestream turbulence levels.

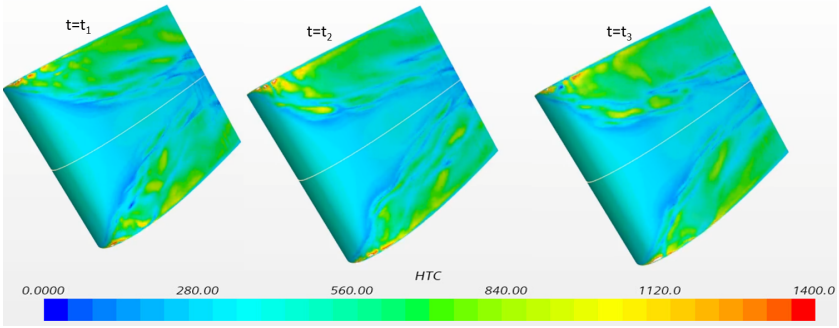

Figure 5.10: A momentary HTC distribution on the suction side of the vane at different timesteps.

Subsequently, the anisotropic linear forcing was implemented to better replicate turbulence conditions of the high turbulence intensity Case F, as explained in Section 4.1. Time-averaged values of HTC are shown in Figure 5.11 and Figure 5.12 at various locations on the vane, together with RANS predictions and the experimental data. The turbulence level was increased due to the implementation of ALF in the hybrid simulations, however, it was still lower than in the experiment. The calculated turbulence intensity, Tu, in front of the leading edge has decayed to 6%-7%, instead of $Tu = 8\%$ as in RANS simulations. The turbulence intensity is calculated with Equation 3.19 using the sum of modelled and resolved energy. Nonetheless, the obtained results allow drawing comparisons with RANS simulations. Since the wall treatment depends on RANS formulation, the hybrid model was also equipped with the lag EBL model but results showed only minor discrepancies when compared to the SRH results with the SST $k-\omega$ formulation, and results of the latter are displayed in Figure 5.12. An additional RANS simulation with $Tu_{in} = 5\%$ is performed for comparison in Figure 5.12.

Firstly, the ratio between HTC at the stagnation point and the HTC at $s/span$ = 1, where the secondary flows attach to the wall, is predicted accurately by the SRH model at 10% of span cross-section in Figure 5.11b. The overprediction of the stagnation HTC has seemingly disappeared but also the incoming turbulence level is lower. However, the strong HTC enhancement due to secondary flows still persists in SRH results. Secondly, as reported in Figure 5.1, the RANS SST simulation predicted a strong additional streak of high HTC, associated with the suction side leg of the horseshoe vortex. In the SRH time-averaged HTC distribution, this streak of large HTC is still observed but it is less pronounced as shown in Figure 5.11a. This is also supported by Figure 5.11b, where at $s/span$ = 0.7 the HTC enhancement is more gradual for the SRH time-averaged results. Similarly, the HTC results pattern at 25% span shows better agreement with the experimental data on the suction side in Figure 5.12b. Notably, higher HTC values are reported on the suction side close to endwalls with the SST model and $Tu_{in} = 5\%$ due to a larger endwall boundary layer. It was observed that higher turbulence suppresses the endwall boundary layer. The SRH model results in Figure 5.12b signify that the time-averaged solution of HTC on the suction side does not include largely varying HTC values at $s/span >$0.8.

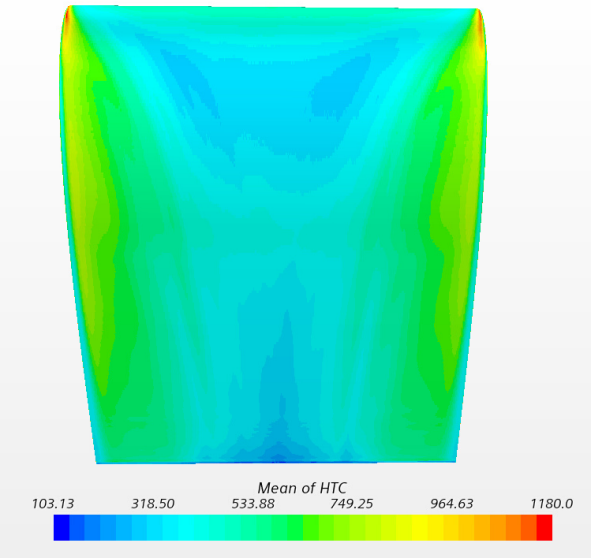

(a) Time-averaged HTC distribution on the suction side of the vane as predicted by a transient SRH simulation. A comparison in terms of experimental data and RANS results is in Figure 5.1.

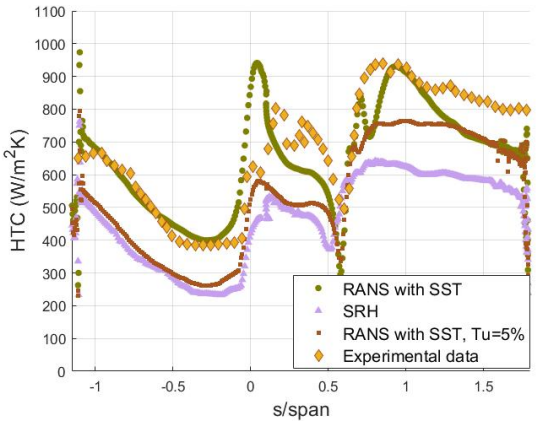

(b) Time-averaged value of HTC at location 10% of span for SRH simulation, compared with experimental data and RANS prediction with the SST model.

Figure 5.11: HTC results on vane surface by SRH simulation with applied anisotropic linear forcing. Case F

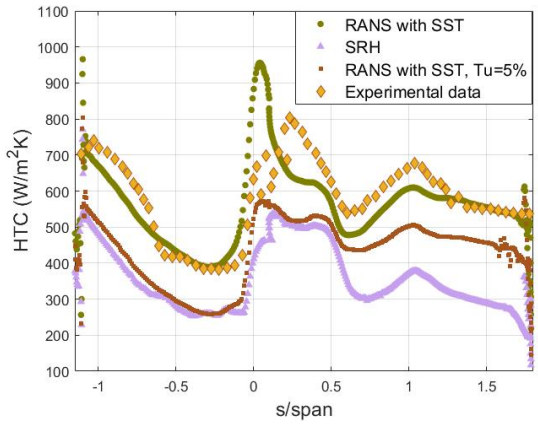

(a) HTC at midspan

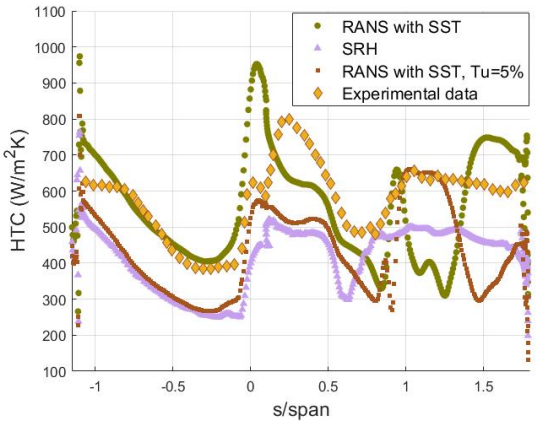

(b) HTC at 25% span

Figure 5.12: HTC results of SRH simulation compared to experimental data at midspan and at 25% of span. Case F

5.1.7. Summary of CFD results for Giel experiment

- The RANS models are capable to predict the HTC enhancement due to secondary flows impinging on the suction side of the airfoil. The estimated trends of HTC development on the vane surface are observed in the experiment, validating the implemented CFD methodology.
- The predicted HTC results are largely susceptible to the turbulent conditions at the inlet. The turbulence intensity affects transition location, the HTC magnitude, and the horseshoe vortex development
- The lag EB model, which aims to account for near-wall turbulence anisotropy, provided the closest agreement to the experimental data in terms of estimating the HTC enhancement due to secondary flows. However, for high turbulence intensity cases it overestimated the stagnation HTC, and it could not predict transition in low turbulence intensity cases. The SST $k-\omega$ model limited the stagnation line overpredictions.
- An implementation of the transition model is imperative to capture transition. The boundary layer on the suction side was in a laminar state for a significant portion of the vane surface only in

low turbulence intensity cases, for which the transition $\gamma - Re_\theta$ model successfully captured the transition onset. In the case of a high inlet turbulence intensity (8%), the transition model is not needed due to a turbulent boundary layer.

- Enabling the crossflow term in the $\gamma - Re_\theta$ transition model was found to improve HTC predictions when compared to the experimental data. However, that was observed only in low turbulence cases when the transition onset was sufficiently downstream where the secondary flows attach to the suction side surface.
- A high turbulence intensity weakened the suction side leg of the horseshoe vortex due to suppressing the endwall boundary layer. The detailed horseshoe vortex structure modelled by the SST and lag EB models differed. The horseshoe vortex unsteadiness was highlighted in the SRH transient simulations.
- The scale-resolving hybrid model with an additional computational cost can capture horseshoe vortex unsteadiness and avoid RANS deficiencies, such as stagnation HTC overprediction. However, it can be challenging to ensure realistic turbulence conditions at the inflow.

5.2. Film cooled vane

The results are first provided for RANS simulations with both uniform and swirling inflow, and then the scale resolving hybrid model results are presented.

5.2.1. RANS predicted results

Investigation of adiabatic cooling effectiveness is performed with both RKE and lag EB turbulence models. The cooling effectiveness distribution on the vane leading edge is shown in Figure 5.13 with a blowing ratio of 1.40. Around 500-1000 iterations were needed to reach convergence.

As shown in Figure 5.13, the overall pattern and distribution of coolant are predicted similarly with both lag EB and RKE turbulence models. The predicted cooling effectiveness is higher on the suction side of the vane as compared to the pressure side, and no coolant lift-off is observed on any of the cooling hole rows. The effective suction side cooling is associated with a lower pressure on the suction side as compared to the pressure side, contributing to an extensive coolant coverage. The coolant streams travel downstream without fully mixing out with the mainstream until close to the trailing edge. This is likely a deficiency of RANS when predicting mixing between two streams whilst assuming isotropic turbulence. The absolute values of cooling effectiveness predicted by RKE and lag EB turbulence models slightly differ when analysing the surface-averaged cooling effectiveness. Adiabatic cooling effectiveness is increased on the suction side but reduced on the pressure side with the lag EB model as compared to the RKE model, as shown in Table 5.1 for cases with $Tu_{in} = 8\%$. This is despite recording lower maximum effectiveness in Figure 5.13 immediately downstream of the cooling hole by the lag EB model. The total surface-averaged cooling effectiveness over the entire leading edge differs only by 0.02 between both turbulence models, suggesting that the predicted stagnation line location slightly differs. The surface-averaged quantities are obtained on the areas ”PS” and ”SS” as shown in Figure 4.24.

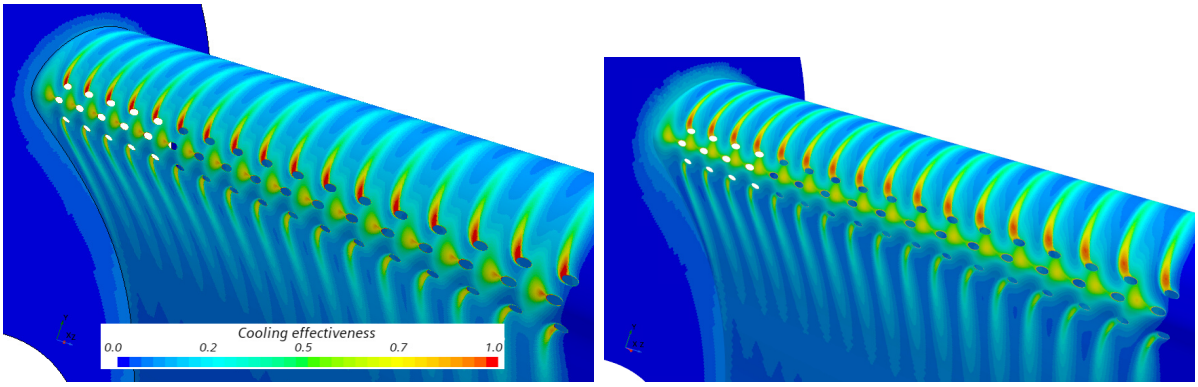

(a) RKE model computation. **(b)** Lag EB model computation.

Figure 5.13: Adiabatic cooling effectiveness on vane leading edge, Tu_{in} =8%

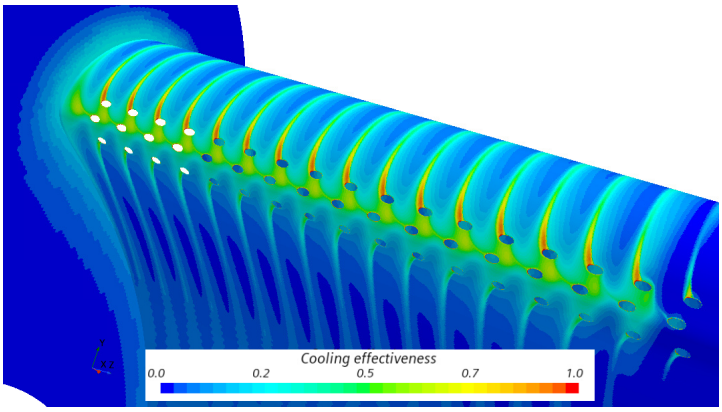

Figure 5.14: Adiabatic cooling effectiveness on vane leading edge with the RKE turbulence model, Tu_{in} =1%

Table 5.1: Various RANS simulation results of area-averaged cooling effectiveness values on the vane leading edge regions (regions visualised in Figure 4.24).

Turbulence model	Realizable $k-\varepsilon$	Realizable $k-\varepsilon$	Lag EB	Realizable $k-\varepsilon$	Lag EB
Tu_{in}	1%	8%	8%	8%	8%
Swirl intensity, S_n	-	-	-	17%	17%
η_{avg} on "PS"	0.180	0.238	0.213	0.216	0.184
η_{avg} on "SS"	0.290	0.305	0.329	0.249	0.250
η_{avg} total	0.242	0.275	0.277	0.234	0.221

The adiabatic cooling effectiveness on the leading edge is shown in Figure 5.14 for a simulation with a reduced turbulence intensity of Tu_{in} =1%. The lower turbulence at the inlet reduces the area-averaged cooling effectiveness. It is argued that the higher turbulence intensity leads to a stronger dispersion of coolant back to the wall, hence increasing the coolant contact with the surface and, thus, the cooling effectiveness. As compared to the high turbulence inflow case, the cooling effectiveness is lowered, and the coolant traces are more narrow in Figure 5.14 for Tu_{in} =1%.

Swirling inflow

The swirling inflow is implemented to study its effect on showerhead cooling. The first inflow profile is obtained by simulating a straight channel flow with a perfect circular swirl profile provided at the inlet. The swirling flow is developing downstream and shaped by the influence of the endwalls. The swirl core is leading-edge aligned, and the RKE turbulence model is implemented. The swirl intensity, defined as a ratio between average tangential and axial velocity, is 17%. The film cooling effectiveness

distribution on the vane leading edge is shown in Figure 5.15

Swirling inflow considerably affects the showerhead cooling and adiabatic cooling effectiveness. Notably, the stagnation line is shifted which is expected. The clockwise swirl alters the pressure field of the bulk flow in the vicinity of the leading edge. The cooling effectiveness is increased in the regions where the radial velocity component of the swirl aligns with the mainstream flow direction. These are the suction side on the left part of the leading edge, and the pressure side on the right side in Figure 5.15. There is a positive incidence angle close to the endwall on the left in Figure 5.15, but negative on the right. The swirl profile is shown in Figure 4.20

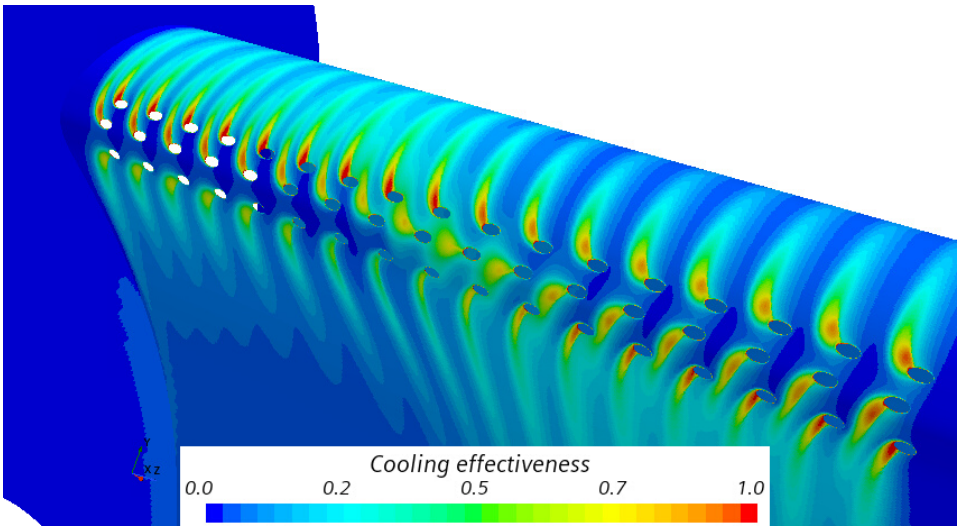

Figure 5.15: Adiabatic cooling effectiveness with a swirling inflow (clockwise swirl), Tu_{in} =8%.

Overall, the leading edge area-averaged adiabatic cooling effectiveness is reduced with the swirling inflow by 0.04, about 15%, as compared to results without swirl in Table 5.1. Additional attention is put towards the regions where there is the highest cooling effectiveness, as shown in Figure 5.16. These are the regions where the swirling velocity components aligns with the mainstream flow direction. On the suction side region, the area-averaged cooling effectiveness η_{avg} = 0.313, which is similar to the total area-averaged value reported without swirl on the suction side for simulations with the RKE model. However, it is noted that the area in Figure 5.16 excludes the narrow region close to endwall that does not have coolant coverage in the swirling inflow case. Regarding the region on the pressure side, however, the cooling effectiveness is considerably increased to η_{avg} = 0.295 which is an increase by approximately 0.06, or 25%, as compared to the average pressure side value in the uniform inflow simulation, reported in Table 5.1. This increase is associated with enhanced coolant coverage on the pressure side due to swirl affecting the pressure field in front of the leading edge.

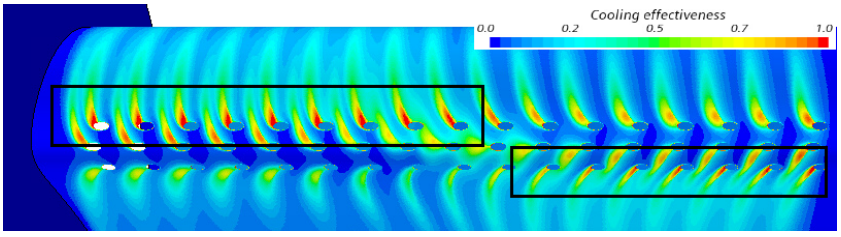

Figure 5.16: Areas of enhanced cooling effectiveness due to a swirling inflow (clockwise swirl).

If low turbulence (Tu < 1%) is imposed at the inlet, there is a complete lift-off for the cooling jets in the regions where the swirl velocity component misaligns with the mainstream flow direction, as shown in Figure 5.17. Thus, the cooling effectiveness is significantly reduced to area-averaged η_{avg} = 0.083 on

the suction side region. The coolant jets tend to reattach downstream. Similar to the uniform inflow case, the high turbulence contributes to higher cooling effectiveness by aiding coolant dispersion back towards the wall.

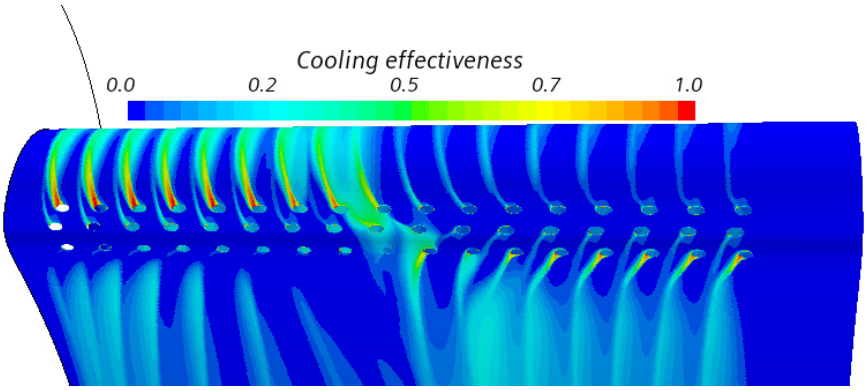

Figure 5.17: Adiabatic cooling effectiveness with a swirling inflow (clockwise swirl), Tu_{in} =1%.

The pressure field alteration is shown in Figure 5.18b. The incidence angle is positive at cross-section at 25% of the span, and negative at 75% of the span, as defined in (Figure 5.18a). Notably, for the swirl intensity of 17%, the pressure ratio at the front part of the airfoil is altered only by 0.01 - 0.02, however, it is enough to considerably affect the coolant distribution and shape the stagnation line.

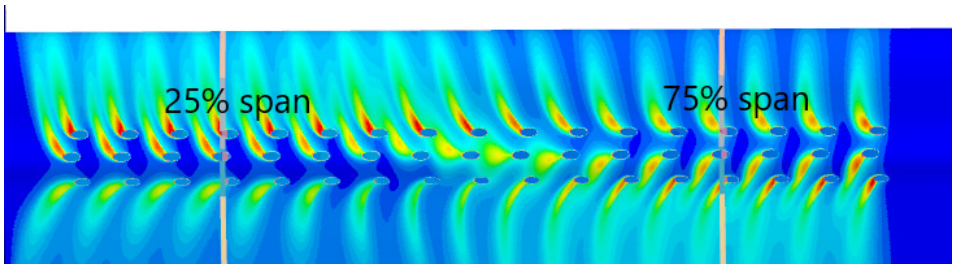

(a) Locations of 25% and 75% span cross-sections.

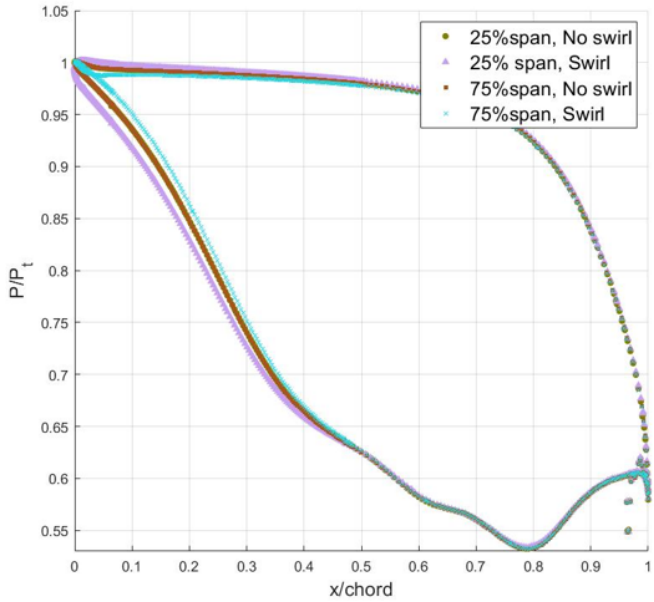

(b) Pressure ratio on the airfoil surface at cross-sections of 25% and 75% of airfoil span. The altered pressure field due to swirl is observed at the front part of the airfoil. Note, the pressure ratio for inflow without swirl has data overlapping between 25% and 75% span because of the symmetry.

Figure 5.18: Pressure ratio over the airfoil surface at various span locations

The aerodynamic row efficiency, defined in Equation 4.7 is reduced from 0.938 in the uniform inflow case to 0.935 in the swirling inflow case, signifying a slightly increased aerodynamic loss. Notably, the difference is minimal, however, the observed trend is in line with results from [18], considering that the currently implemented swirl intensity is 17%.

Swirl with a radial temperature profile

Simple swirl profiles allow investigating of the theoretical effect of the swirl on flow physics. However, such an inflow is circular and almost symmetrical, and it is not coupled with a hot-streak or radial temperature distribution. An extracted profile from the FACTOR simulation is implemented, as described in Section 4.2. A much stronger swirl with an intensity of 75% is observed as compared to the previous case, and it causes a severe stagnation line alteration. Therefore, the coolant distribution is greatly influenced. A slightly higher blowing ratio of 1.90 is implemented to ensure that the hot gas ingestion is avoided in the high pressure regions.

The temperature distribution on the leading edge surface is shown in Figure 5.19 with the lag EB model. Notably, the temperature distribution is influenced by the incoming hot-streak. The hot-streak migration is visualised in Figure 5.20. The swirl intensity is rather large in this case, and the stagnation line has moved downstream of the suction side cooling row. Such a situation should be avoided in showerhead cooling design in real gas turbines. The placement of the cooling rows should account for the expected unsteadiness of the stagnation line.

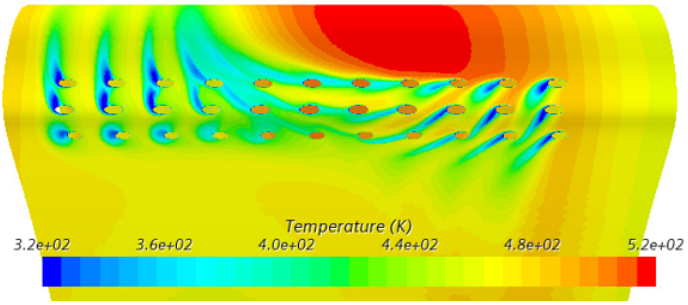

Figure 5.19: Temperature distribution on the vane leading edge with a swirling inflow and a radial temperature distribution.

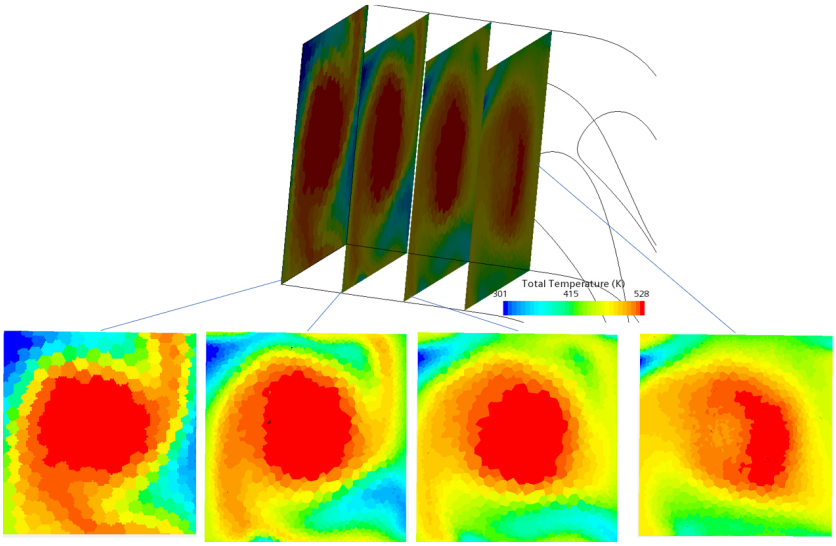

Figure 5.20: Hot-streak migration

The pressure field alteration is visualised in Figure 5.21. A considerably higher influence on the leading edge pressure ratio is observed when compared to swirl intensity of 17% in Figure 5.28. The pressure

ratio varies up to 0.05 between midspan and regions closer to endwalls at a specific chordwise location. The row efficiency, defined in Equation 4.7, is reduced from 0.935 to 0.888, signifying a much larger aerodynamic loss, as compared to the simple swirl with an intensity of 17%.

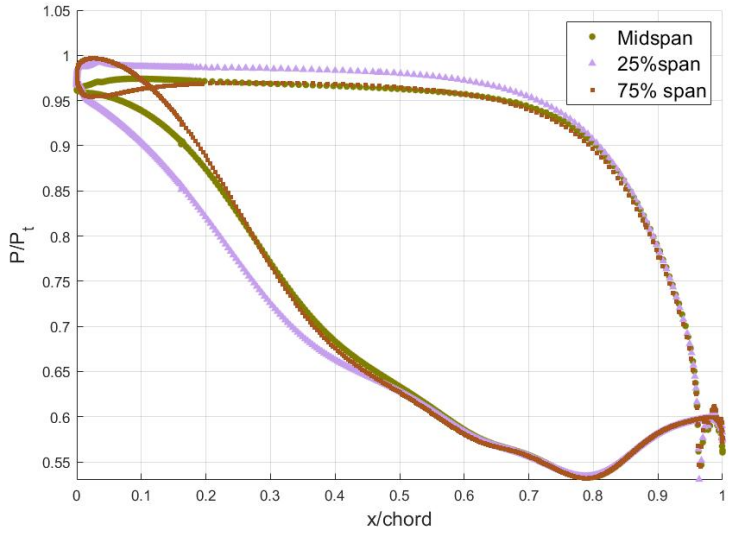

Figure 5.21: Pressure ratio at various span locations with a swirling inflow with an intensity of 75%.

There is a critical hot-streak observed on the suction side in Figure 5.19. The high pressure region is not letting the suction side cooling row channels distribute the coolant onto the suction side surface as the stagnation line is strongly altered. On the pressure side at this location of the span, the coolant coverage and cooling effectiveness are high, therefore, reducing the impact of the hot streak. Hence, a combination of strong swirl and hot streak can lead to local regions of high temperature despite the film cooling. It also signifies the importance of cooling design details. The placement of cooling rows should account for an unsteady stagnation line.

5.2.2. Scale resolving hybrid simulation results

Results from a transient SRH simulation with a uniform inflow were obtained starting from a steady-state RANS initial solution with a uniform inflow. Since no synthetic turbulence production, such as ALF, was applied, the turbulence level at the inflow was low. Time-averaged cooling effectiveness on the leading edge is shown in Figure 5.22, and a momentary solution at t =0.002 s in Figure 5.23. The predicted cooling effectiveness is considerably lower as compared to RANS simulations. The suction side ("SS") area-averaged cooling effectiveness is reduced from 0.29 to $\eta_{avg} = 0.185$. Similarly, a reduction on the pressure side section is observed with $\eta_{avg} = 0.07$. A strong mixing between coolant and mainstream is predicted with the hybrid model. Furthermore, the mainstream flow penetrates beneath the coolant jet on the pressure side, causing a coolant lift-off. Subsequently, the cooling effectiveness on the pressure side is lower as compared to the RANS solution provided in Figure 5.14.

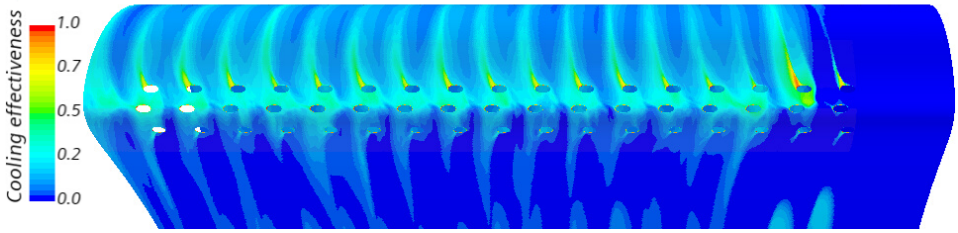

Figure 5.22: Time-averaged cooling effectiveness on the leading edge of the vane. Results of SRH simulation with a uniform inflow.

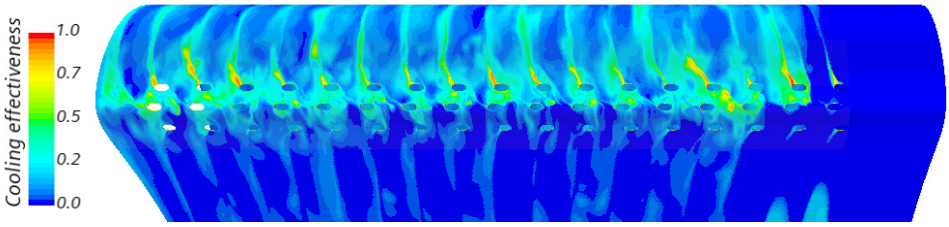

Figure 5.23: Momentary cooling effectiveness distribution on the leading edge of the vane at time $t = 0.002\,\mathrm{s}$. Results of SRH simulation with a uniform inflow.

Q-criterion isosurface, shown in Figure 5.24, allows investigating the flow structures at the leading edge region. A lot of flow structures are resolved in detail at the leading edge region with LES formulation. Further downstream, RANS formulation is applied where the coolant jets are undisturbed. In general, there is a tendency for the mainstream flow vortical structures to bend around the coolant jets. A complete lift-off is characterised by the mainstream flow bending completely around the cooling jets, a similar pattern was observed in work by Ravelli et al. [5] with the DDES model. On the pressure side of the leading edge, the mainstream penetrates beneath the coolant jet. On the suction side, the coolant stays attached to the surface and the mainstream flow structures remain above the coolant jets.

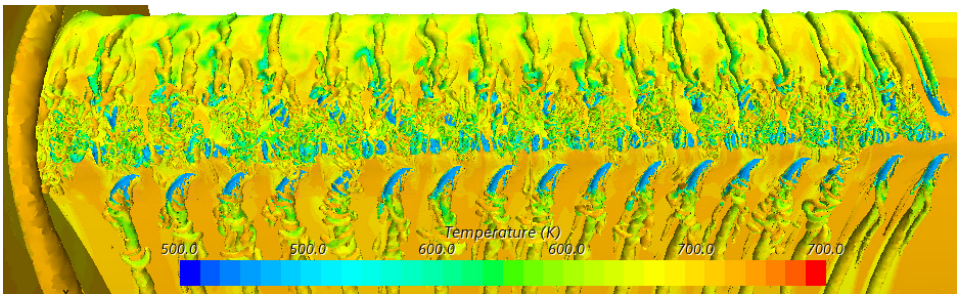

Figure 5.24: Q-criterion isosurface where $Q = 5 \times 10^7\,\mathrm{s}^{-2}$. Results of an SRH simulation with a uniform inflow.

The flow structure is quite chaotic with a lot of turbulence generated in the leading edge region, as shown in Figure 5.25. The cooling jets stay intact due to possessing a large momentum. Vortical structures are forming around the coolant jets. The mainstream flow structures have a complete rotation around the coolant jets if the jets have separated from the vane surface as it is on the pressure side. Furthermore, an interaction between cooling rows is shown in Figure 5.25. The perturbed flow structures seemingly tend to extend to the pressure side cooling holes, and these structures form around and over the middle row cooling jets.

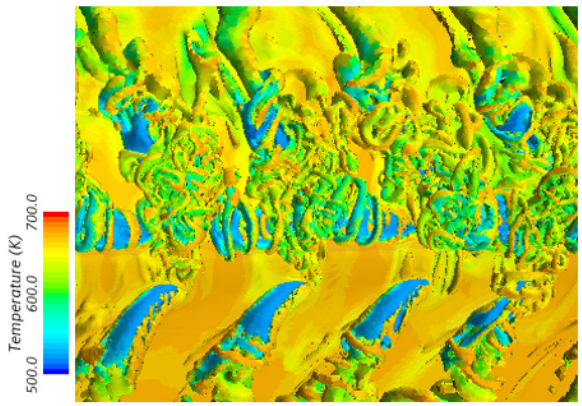

Figure 5.25: Q-criterion isosurface where $Q = 5 \times 10^7\,\mathrm{s}^{-2}$, a closer visualisation of the leading edge flow structures for a simulation with a uniform inflow.

Coolant flow development inside the channels is visualised in Figure 5.26. Velocity and Q-criterion values suggest that a pair of vortices is present on the left side of the cooling hole cross-section, i.e. the side closest to the coolant plenum. In that region, the absolute velocity of the coolant is lower.

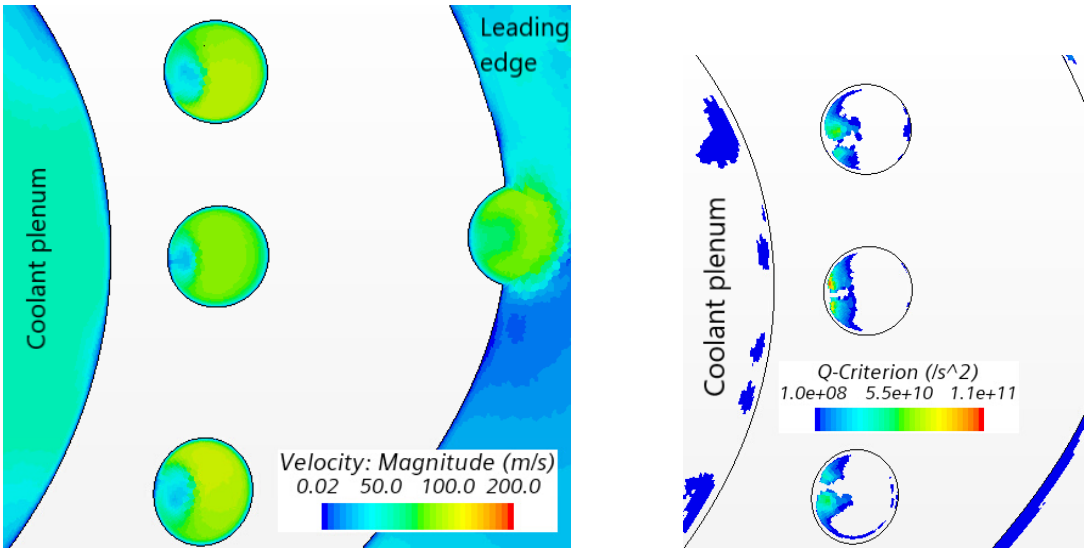

(a) Velocity magnitude at the cross-section of coolant channels, coolant flowing in the direction out of the page.

(b) A positive Q-criterion at the cross-section of coolant channels.

Figure 5.26: Velocity and Q-criterion at the cross-section of coolant channels. A pair of vortices is developing inside the channel.

Swirling inflow

Swirl influences the coolant distribution and cooling effectiveness, as already shown in RANS simulations. In the regions where there is a swirling flow component aligned to the mainstream direction, the coolant jets are less susceptible to liftoff. In hybrid simulations, the same trend persists, as shown in Figure 5.27. Furthermore, when investigating the surface temperature, a shear layer unsteadiness is observed in Figure 5.28a downstream of the pressure side cooling holes. In the middle row, much lower cooling effectiveness is observed due to an early coolant lift-off. Q-criterion isosurface, shown in Figure 5.28b, helps to visualize the flow structures in more detail. The high-temperature mainstream air tends to bend around the coolant jets in the middle row, penetrating also between the coolant jet and the vane surface. On the pressure side jet, however, the flow field is different and the mainstream does not penetrate between the coolant jet and surface in the immediate vicinity downstream of the holes. The mainstream flow still tends to bend around the jet from a location approximately 2-3D downstream of the hole. Eventually, the coolant mixes out with the mainstream. Notably, even though the largest part of the leading edge was resolved with the LES, the suction side cooling holes on the left side in Figure 5.27 had considerably less than 80% of turbulence kinetic energy resolved. This is due to a higher flow velocity locally that imposed larger requirements for flow resolution.

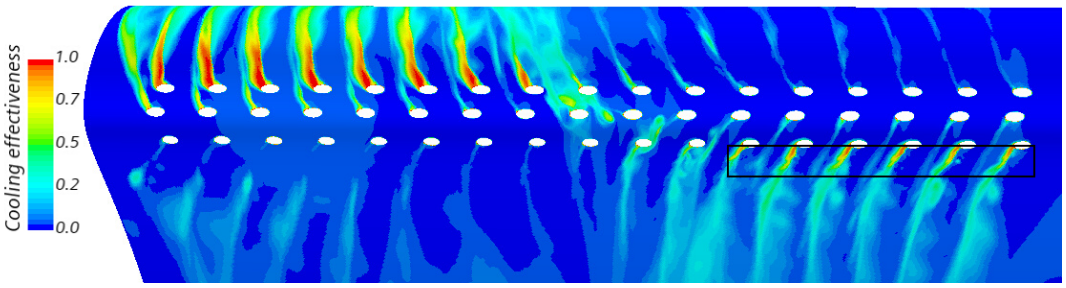

Figure 5.27: Cooling effectiveness distribution on the leading edge. Results of an SRH simulation at t =0.004 s

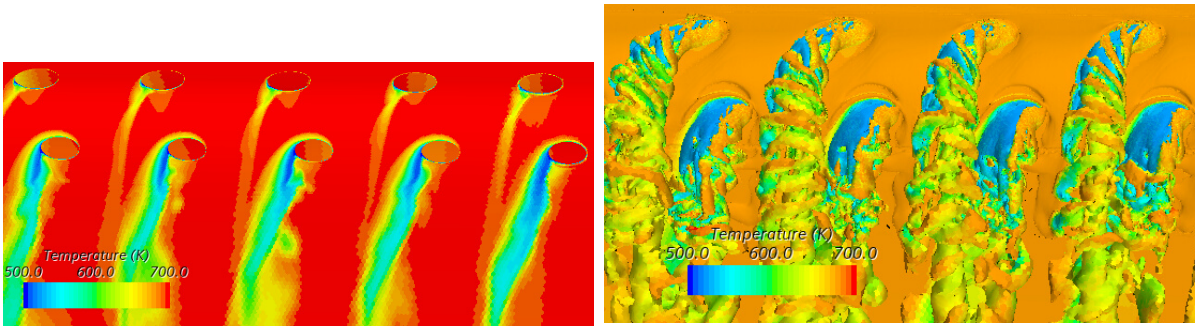

(a) Temperature distribution on the vane surface.

(b) Isosurface of Q =5 $\times$ 10^7 s^{-2}

Figure 5.28: Temperature and Q-criterion isosurface on the pressure side of the vane leading edge where the swirl velocity component aligns with the mainstream flow direction resulting in increased cooling effectiveness.

Area-averaged cooling effectiveness in the region on the pressure side where the coolant is attached to the surface (circled in Figure 5.27) is η_{avg} =0.113. This value is increased from η_{avg} =0.088 recorded in the RANS simulation with Tu_{in} =1% in Figure 5.17. Thus, for the coolant jets that are well-attached to the surface due to swirl, the cooling effectiveness is predicted higher by the SRH model as compared to RANS in the immediate vicinity downstream of the holes. Closer to the opposite endwall on the pressure side cooling row, the swirl velocity component does not align with the mainstream flow direction. In this region, the coolant jet separates from the surface as shown in Figure 5.29, and the pattern of mainstream flow bending around the coolant jet is observed immediately downstream of the hole.

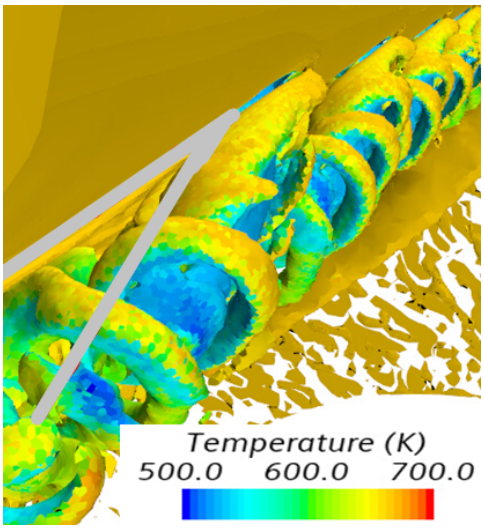

Figure 5.29: Coolant lift-off on the pressure side. Visualised in terms of Q-criterion=5 $\times$ 10^7 isosurface.

The second swirl profile with an intensity of $S_n = 75\%$ is simulated by the SRH model. The momentary and time-averaged temperature distribution on the leading edge is shown in Figure 5.30. A strong interaction between adjacent coolant jets is observed, especially on the suction side of the vane, as opposed to RANS results for the simulation with the second swirl profile in Figure 5.19. The coolant jets do not travel downstream parallel to each other, instead a strong mixing is observed on both sides of the vane surface. The strong stagnation line alteration is predicted similarly as with RANS. The flow field in front of the leading edge is largely chaotic due to the strong swirl. Notably, the coolant coverage on the leading edge and cooling effectiveness immediately downstream of the holes is relatively high as compared to the weaker swirl in Figure 5.27, since a complete coolant lift-off is mostly avoided due to high mainstream momentum locally. The unsteadiness of the shear mixing layers can be observed from the temperature distribution in Figure 5.30a.

Large coolant coverage on the pressure side with negative incidence angle due to swirl is observed in Figure 5.30a on the right side. Time-averaged temperature is compared to RANS simulation. The average temperature on the pressure side region ("PS" in Figure 4.24) is predicted 5 K lower, hence, resulting in higher cooling effectiveness. The suction side region area-averaged temperature is increased by 15 K, as compared to RANS results. However, this is largely attributed to a higher portion of the vane surface being exposed to the high-temperature hot-streak on the suction side in SRH results. Nonetheless, the average temperature in the region where there is coolant coverage on the suction side (left side in Figure 5.30) is increased by 7 K as compared to RANS results. This corresponds to the strong interaction observed between adjacent cooling jets and the mainstream in SRH results in Figure 5.30, leading to a higher temperature that is also more uniform.

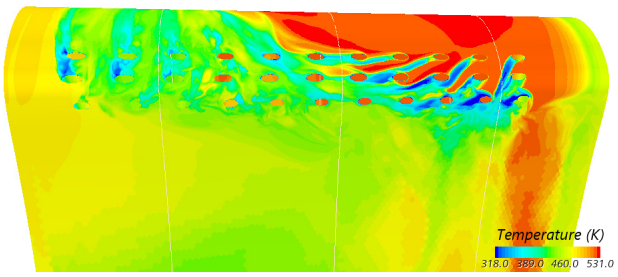

(a) Momentary temperature distribution on the vane surface at time $t = 2.2 \times 10^{-3}$ s

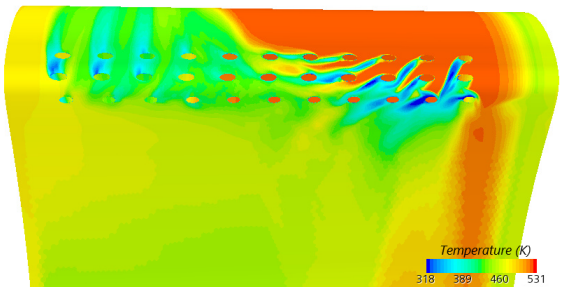

(b) Time-averaged temperature distribution

Figure 5.30: Temperature distribution around vane leading edge with the strong swirl and hot-streak profile applied at the inlet. Results of the SRH simulation.

The momentary temperature distribution on the leading edge is shown in Figure 5.31a at four different time steps. The focus is put on the area where the coolant is discharged onto the suction side of the vane. The flow field is shown to be unsteady, and there is a strong interaction between coolant jets and the mainstream. The resolved flow structures in Figure 5.31b suggest that coolant jets are pushed onto the vane surface, and the jets do not preserve their shape as was observed in the previous RANS simulations. Moreover, traces of high-temperature gas from the hot-streak are observed in Figure 5.31b, but the coolant effectively covers the vane surface beneath them.

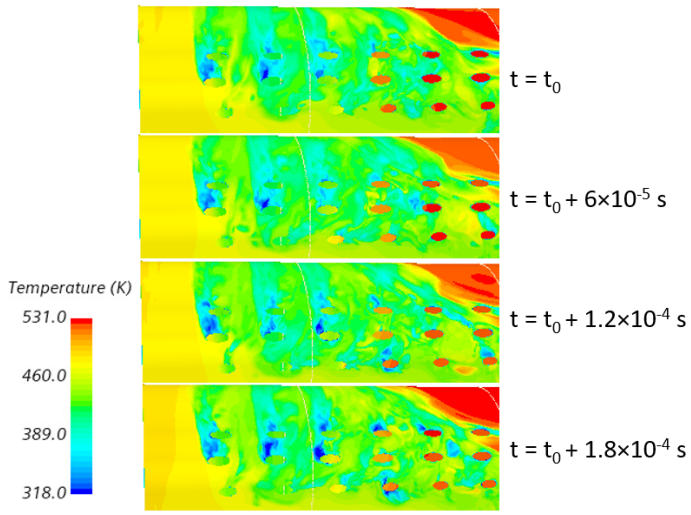

(a) Temperature distribution on the vane surface, visualising time scale of the unsteady behaviour.

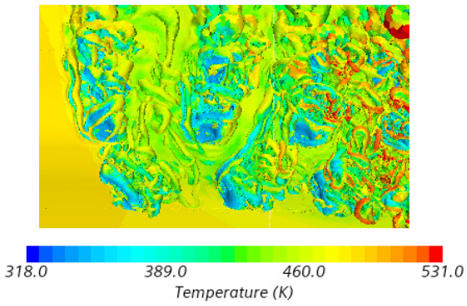

(b) Isosurface of $Q = 6 \times 10^7$ s^{-2}. Top view of the cooling holes on the leading edge. Traces of high temperature gas are observed entering the region above the coolant jets.

Figure 5.31: Temperature distribution and Q-criterion isosurface on the vane leading edge where the swirl leads to coolant distribution on the suction side. SRH simulation with the swirling inflow of intensity S_n =75%.

6

Discussion

A numerical study is performed to study showerhead film cooling and heat transfer on a transonic nozzle guide vane. Various turbulence models were validated to experimental data with the focus to capture the horseshoe vortex influence on the HTC. Subsequently, adiabatic film cooling effectiveness on the showerhead film cooling arrangement was analysed by applying a swirling inflow. RANS and hybrid RANS-LES methodology was adopted, and a discussion of the main findings is presented in this section.

6.1. HTC evaluation

Amongst the steady-state RANS models, the simulations with SST $k-\omega$ and lag EB turbulence models provided the closest agreement to the experimental data, regarding HTC enhancement due to secondary flows on an uncooled vane. The three most influential parameters affecting the HTC distribution were found to be turbulence conditions, transition and secondary flow development. The turbulence conditions of the flow upstream also affect both, transition and secondary flows.

6.1.1. Laminar-to-turbulent transition

A use of the transition model was imperative to accurately capture transition on the suction side of the vane. SST $k-\omega$ was coupled with the $\gamma - Re_\theta$ transition model, and it was the only model accurately capturing transition in low turbulence intensity (Tu < 1%) cases as shown in Figure 5.4a. Furthermore, enabling the crossflow-induced transition term improved the HTC predictions on the suction side region where the vortices impinge on the wall, as reported in Figure 5.7. Hence, the lack of accurate transition predictions proved to be the biggest limitation of the lag EB and $\overline{v^2}-f$ models that do not support coupling with a transition model. Two different $\gamma - Re_\theta$ transition model correlations were compared in both Re =0.5 $\times$ 10^6 and Re =1.0 $\times$ 10^6 flow cases. Both, Suluksna-Juntasaro (the default in $Star-CCM+$ software package) and Kelterer correlation, predicted similar transition onset on the suction side in the low Reynolds number flow case. Kelterer correlation provided accurate transition location in the high Reynolds number flow case, as opposed to the Suluksna-Juntasaro correlation that predicted transition too far downstream on the suction side. Nonetheless, it remains inconclusive whether the considerably too late transition is due to the model deficiency or due to the reported dots of paint in the experiment that affected the HTC results in the Re =1.0 $\times$ 10^6 flow case.

It should be noted that, in high pressure gas turbines, the inflow is typically highly turbulent which would cause a very early transition, similar to the reported flow cases of 8% turbulence intensity. An argument can be made that often in such applications there is no need to implement the transition model. Especially if there is showerhead cooling applied that would trip the flow at the leading edge. On the other hand, if the transition model is avoided for an uncooled vane, a CFD practitioner must investigate if the incoming turbulence level is high enough to ensure a turbulent boundary layer immediately downstream of the leading edge. Furthermore, underpredictions of HTC on the pressure side are reported with SST $k-\omega$ $\gamma - Re_\theta$ (e.g. in Figure 5.9) if the incoming turbulence level is substantial. This is

due to the transition model assuming a fully laminar boundary layer on the pressure side that was not observed in the experimental data.

6.1.2. Secondary flow influence on the HTC

Secondary flows strongly affect heat transfer on the suction side where the horseshoe and passage vortices impinge on the wall. Notably, the airfoil shape and large boundary layer size on the endwalls contributed to the strength of the secondary flows. The horseshoe vortex develops close to the endwalls in front of the leading edge. A major challenge for RANS CFD methods is to obtain a steady-state solution of the horseshoe vortex. It is a largely unsteady flow phenomenon, hence, only a representative solution can be obtained. Furthermore, the SST $k-\omega$ and lag EB model predictions differed. Compared to steady-state experimental measurements, the lag EB model provided a closer agreement to the data in the region where secondary flows attach on the suction side. This is also the model that can replicate near-wall anisotropic turbulence.

Results in Figure 5.6 show that steady-state RANS with SST $k-\omega$ and lag EB turbulence models predict slightly different development of the horseshoe vortex. The SST $k-\omega$ model results suggest that there is strong vorticity at the core of the vortex and multiple separate vortical structures in the steady-state flow field (reported in Figure 5.5). These results agree with a study by Levchenya & Smirnov [103] summarised in Section 2.4, where the authors reported that the multiple vortical structures were observed in experimental results. However, these structures in the study were observed only momentarily and not in a time-averaged flow field. Hence, the simplified horseshoe vortex predicted by the lag EB model simulation can give a good estimate of a time-averaged flow field. Furthermore, the lag EB model provided a low value of reduced stress function, ϕ, at the location where the passage vortex attach to the suction side. A low value of ϕ suggests that there is a high anisotropy of turbulence in a particular location, leading to the SST $k-\omega$ model overpredicting the turbulence kinetic energy production at the location where the vortices attach to the surface.

A scale-resolving hybrid RANS-LES model (SRH) implementation provided an insight into the unsteady behaviour of the horseshoe vortex. A time-averaged solution indeed replicated the pattern of experimental data accurately, as reported in Figure 5.11b. However, the magnitude of HTC was underpredicted due to lower levels of turbulence intensity achieved at the inlet. Overall, the SRH model is promising for HTC predictions if the turbulence level at the inlet is accurately replicated. When analysing steady-state RANS predictions of horseshoe vortex, a CFD practitioner should address the limitations, such as not capturing unsteadiness and anisotropic turbulence, even though the general trend of HTC enhancement is well predicted. Furthermore, it is noted that the hybrid model implements RANS formulation for the wall heat transfer. Hence, a choice of the desired turbulence model is important as well.

6.2. Showerhead film cooling performance

Showerhead cooling performance was investigated in terms of adiabatic cooling effectiveness with different inflow conditions. A common trend is that cooling effectiveness is higher on the suction side from the stagnation line, as compared to the pressure side. This is expected, due to lower pressure on the suction side. Furthermore, the high momentum of the mainstream flow mostly does not allow for the coolant jet to separate from the vane surface on the suction side. In general, the cooling jets are susceptible to lift-off in the leading edge region, and it highly influences the film cooling effectiveness. This phenomenon would be less prominent further downstream at pressure or suction side cooling rows, where the coolant channels would be aligned to the mainstream flow direction, instead of being placed perpendicularly to the mainstream. The blowing ratio was kept between BR =1.4 - 1.9. In previous work by Ravelli et al. [5], the authors reported coolant lifting off the leading edge surface with $BR = 3.0$, resulting in a relatively low cooling effectiveness in certain regions where the coolant was completely unattached to the surface.

Notably, despite enhancing the flow mixing, a higher turbulence intensity actually improved the cooling effectiveness due to the dispersion of coolant as it was ”pushed” back towards the wall. This

phenomenon signifies that ensuring avoidance of coolant liftoff is the most critical aspect of the showerhead cooling design. On a flat plate film cooling, it is expected that higher turbulence would simply reduce the cooling effectiveness due to enhanced mixing [121]. On the other hand, a designer must always take into account the risk of hot gas ingestion. This extreme case would occur if the pressure in the coolant plenum is lower than the mainstream flow pressure. A sub-optimal cooling effectiveness at the expense of a higher blowing ratio to avoid hot gas ingestion is preferred, as the latter can impose structural damage. Hence, it is likely that if higher blowing ratios $BR > 2$ are used in practical designs the cooling effectiveness can be further reduced.

The unsteady stagnation line, especially with a swirling inflow, can pose a challenge in the design process. As results show, a swirling inflow can significantly alter the stagnation line, therefore, the cooling rows should be placed such that both, the suction and pressure sides, have coolant coverage in various flow conditions. A bad example is shown in Figure 5.19 where a hot-streak and high pressure region coincide on the suction side of the vane, leading to no coolant coverage locally on the suction side. A weaker swirl in Figure 5.15 also affected the cooling effectiveness locally, causing a complete lift-off in case of low turbulence intensity in Figure 5.17 in regions where the swirling component misaligned with the mainstream flow direction. For the leading edge aligned swirl core, the coolant coverage at the leading edge is largely asymmetric. The swirlers are commonly used in lean-burn aeroengine combustors to stabilise the flame. Often the swirling flow persists until the inlet of a high pressure turbine, hence, it is relevant to study its effect on showerhead cooling. However, the implemented inflow profiles were not matched to the flow angles of the nozzle guide vane. Hence, the strongly swirled FACTOR inflow results in an extreme case that is not likely in a realistic design. Nonetheless, the effects of a disturbed stagnation line and altered coolant coverage are clearly detectable and can be studied.

A scale resolving hybrid model allowed the investigation of the flow pattern in more detail. Steady-state RANS models assume isotropic turbulence, and some of the models, like the lag EB model, introduce transport equations to estimate the anisotropy measure. However, even in the latter case, the results in terms of flow mixing are not reliable. Nonetheless, the general pattern of coolant coverage and stagnation line location are predicted similarly as in the SRH simulations. In addition, the steady-state RANS results with the lag EB and RKE turbulence models predicted a largely similar coolant distribution and effectiveness, as shown in Figure 5.13. As opposed to RANS results, the hybrid model simulation predicted a considerably stronger interaction between adjacent coolant jets and the mainstream in case of a highly swirling inflow, which lead to an increased surface temperature locally on the suction side in the region in Figure 5.31a. The flow structures are visualised by means of Q-criterion isosurfaces. In the case of a coolant lift-off, the mainstream hot gas penetrated beneath the coolant jet and the vortical structures formed around the jet, as reported in Figure 5.29. A similar pattern was predicted with the DDES model for the $BR = 3.0$ [5]. In cases when coolant jets were well-attached to the surface, a different and more chaotic flow pattern was observed, especially in cases of a strong swirl (Figure 5.31b). A highly turbulent and chaotic flow is observed at the leading edge that imposes a turbulent boundary layer on the suction side of the vane.

Finally, it is noted that the conclusions from the current study apply only to the flow conditions that were analysed. In heat transfer problems, a general conclusion can rarely be drawn, since turbulence conditions, the momentum of the flow, and other factors greatly influence the flow physics, as was also found in the current study. For example, the inflow at high pressure gas turbine nozzle guide vane is highly turbulent, and it is unlikely to observe turbulence intensities as low as 1%. Similarly, blowing ratios larger than two were not tested in the study. The flow physics is highly complex in the stagnation region, contributing to the uncertainty of different flow conditions. Furthermore, the adiabatic cooling effectiveness largely depends also on the implemented cooling design which was kept constant during the study.

6.3. Hybrid RANS-LES modelling

RANS vs a hybrid RANS-LES model implementation is a trade-off between fidelity of the solution and computational cost. The advantages of the hybrid model are the ability to investigate unsteady flow behaviour and to resolve some of the turbulent scales by imposing LES formulation in specific regions.

The implementation of the SRH model should be addressed. It is important to ensure a CFL number below unity and to resolve at least around 80% of the turbulence kinetic energy in the regions where LES must be imposed. Since the model automatically uses either RANS or LES formulation based on the temporal and spatial resolution of the domain, the parameters such as resolved energy ratio and RANS/LES shielding function should be investigated during simulation. Subsequently, an adaptation of time scale and/or mesh resolution might be required. During simulations, it was often challenging to achieve the criterion of resolving 80% of the turbulent energy around all of the cooling holes across the span, especially if the swirl altered the flow field. If a finer spatial resolution is required in specific regions, then also a smaller timestep is required in order to limit the CFL number. Thus, increasingly driving the computational cost.

The validation case showed that implementation of a hybrid model allows capturing unsteadiness of the horseshoe vortex, which is a limitation for RANS. A more accurate prediction of time-averaged HTC enhancement on the suction side close to endwalls was obtained. Apart from these factors, the prediction of HTC development along the vane surface largely matched RANS predictions. This is expected, since wall treatment and heat transfer calculation is carried out with RANS formulation. Thus, choosing a turbulence model that is able to accurately estimate HTC is of importance also for hybrid models. The scale resolving simulation also requires special attention to ensure representative turbulence conditions at the inflow. The turbulence parameters in the freestream outside of the walls are used in HTC calculation in the RANS formulation that is applied for the wall treatment. Since a flow around an uncooled vane does not involve mixing between multiple streams and is mostly steady, it can be argued that the increase in computational cost is not outweighing the benefits of the SRH model. However, if a focus is on investigating a non-uniform inflow, and accurately capturing the secondary flow field, including the horseshoe vortex, then the hybrid model would be strongly preferred.

The implementation of the hybrid model was essential to model the mixing between mainstream and coolant jets for a film cooled vane. The implemented hybrid model allows to study the detailed physics of the flow field at the leading edge as shown in Figure 5.24, whilst the RANS models merely provide a representative solution with the isotropic turbulence assumption. The coolant jets in the RANS simulation remain attached to the vane surface (reported in Figure 5.13) without mixing out with the mainstream for a prolonged distance over the vane surface up to two-thirds of the chord distance. The complex interactions between coolant jets and the mainstream flow can be studied with the hybrid model. However, an accurate calculation of HTC magnitude would still require capturing representative turbulence conditions at the inflow. The turbulence not only influences the heat transfer calculations directly, but it can also affect the coolant distribution, as shown in Figure 5.14.

Implementation of a hybrid RANS-LES model introduces an additional computational cost when compared to RANS. The hybrid SRH model, however, can be a good alternative to LES. Due to large mesh requirements in film cooling problems, it is highly challenging to implement a full-scale LES formulation for a complete film-cooled NGV. Thus, a hybrid RANS-LES formulation can provide a good alternative by considerably reducing the computational cost. A trade-off between desired fidelity of results and computational cost should be considered when performing RANS, LES, or hybrid simulations of a film-cooled vane. The specific hybrid model implemented in $Star - CCM+$, the scale resolving hybrid model, has not been widely tested in the open literature on such turbomachinery flows involving cooling. The advantage of the SRH model is its adaptability to RANS or LES formulations based on given spatial and temporal resolution. However, a full-scale CHT model implementation of an NGV with internal coolant channels and film cooling would still be extremely costly with a hybrid model for the current industry standards.

6.4. Uncertainty and limitations

Due to its severe influence on heat transfer and cooling effectiveness, turbulence conditions at inflow are argued to be the most prominent uncertainty that should be managed. In the validation case, the statistical turbulence intensity for RANS simulations was carefully matched to the experimental conditions. Nonetheless, the physical measurements of turbulence intensity and length scale are often limited in accuracy [32]. Furthermore, the size of the endwall boundary layer was measured in the ex-

periment. A replication of the boundary layer size in the CFD model is likely an additional error source that can affect the strength of the horseshoe vortex. Applying a representative turbulence level for scale-resolving simulations proved to be a challenge. Synthetic turbulence production can be implemented in this case in order to match the statistical turbulence level predicted by RANS or specified in the experiment. The most of scale-resolving simulations of film-cooled vane were not equipped with synthetic turbulence production. Thus, the results presented for uniform inflow and simple swirl cases have a relatively low turbulence intensity at the inflow. Only the second swirl inflow with 75% swirl intensity provides a higher turbulence level. An increase in incoming turbulence intensity for the case of a uniform inflow would promote coolant jet dispersion back towards the wall and increase the mixing downstream of the holes.

As already discussed, the swirling inflow does not necessarily represent a realistic profile, however, it allows for investigating the influence of this variable on the showerhead cooling performance. A joint combustor-vane simulation with swirl generators would be a more authentic way to approach this problem. Furthermore, the swirl number based on a swirler geometry is a more accurate and universal measure to quantify the swirling flow, as compared to the swirl intensity, or the tangential-to-axial velocity ratio. The simplified model implemented flat endwalls, instead of one convex and another concave, as they are in gas turbines. This shape can slightly influence the development of the horseshoe vortex, although an alteration of film cooling performance is not expected. Finally, in order to fully establish the benefits of hybrid modelling, it would be beneficial to validate the film cooled vane solution with experimental data by measuring the surface temperature of an adiabatic vane, or by performing optical measurements of the flowfield.

7

Conclusion

Film cooling effectiveness was investigated numerically for a nozzle guide vane equipped with showerhead film cooling with CFD RANS and hybrid RANS-LES models. The swirling inflow profile altered the stagnation line and affected coolant distribution and cooling effectiveness locally. The introduction of the scale resolving hybrid model allowed for studying the complex interactions between coolant jets and the mainstream flow. The work was performed within efforts to introduce more advanced numerical methods for gas turbine vane heat transfer and cooling effectiveness estimations at a limited increase in computational cost.

The turbulence models and implemented CFD methodology were validated by recreating the experimental case of a linear cascade of blades from an experiment by Giel et al. [8]. The HTC results obtained from RANS simulation with SST $k-\omega$ and the lag EB $k-\varepsilon$ models largely captured the main flow phenomena and achieved a representative solution. An implementation of the scale-resolving hybrid simulation allowed to capture the unsteadiness of the horseshoe vortex and to obtain a more accurate time-averaged solution. The lag EB model, which includes a transport equation for turbulence anisotropy measure, provided the closest agreement to experimental data of HTC in the region where secondary flows impinge on the suction side surface. Turbulence intensity and length scale were shown to severely influence the heat transfer on the vane surface. In low turbulence intensity (Tu <1%) cases, a clear transition was observed on the suction side, and only the simulations implementing the $\gamma - Re_\theta$ transition model were able to predict it accurately. In high turbulence intensity cases (Tu = 8%), a transition model was not required due to a turbulent boundary layer on the suction side. The resulting time-averaged HTC pattern from the SRH simulation presented a close resemblance to the experimental data, however, it was challenging to replicate the statistical high turbulence conditions at the inlet for the scale resolving model. That resulted in an underprediction of HTC magnitude.

Larger benefits of scale resolving simulation were observed on a film cooled vane. The implementation of the hybrid model was essential for capturing unsteadiness in the shear mixing layers, and for modelling coolant lift-off and mixing between multiple coolant streams and the mainstream flow. Implementation of swirl imposed a radial pressure gradient and shaped the stagnation line, deflecting the coolant jets. In the regions where the swirl velocity component misaligned with the mainstream flow direction, a coolant lift-off was often observed, resulting in a severely reduced film cooling effectiveness. The opposite trend of increased cooling effectiveness was observed in the regions where swirl contributed to the coolant jet staying close to the vane surface due to locally increasing the mainstream flow momentum. Despite high turbulence leading to enhanced mixing of the flow, increased freestream turbulence leads to a slightly higher average cooling effectiveness by dispersing the coolant jets closer to the surface, helping to avoid coolant lift-off. The coolant lift-off turned out to be the most important variable affecting showerhead cooling performance.

Following the results of swirling inflow cases, it is emphasised that a design of a showerhead cooling scheme should account for an unsteady stagnation line. The scale resolving hybrid model allows for designers to analyse complex flow interactions and coolant jet behaviour, which is not possible with

steady-state RANS simulations. However, the importance of replicating the incoming flow turbulence characteristics cannot be underestimated for accurate predictions of the heat transfer magnitude. The conjugate heat transfer method, as discussed in Section 2.2, is of great interest in research for cooled vanes, however, its convective heat transfer calculations are often limited to steady-state RANS formulations due to large computational resource demands. Future work can involve a full-scale film cooled vane external heat transfer analysis with a hybrid RANS-LES model. An application of more advanced and accurate numerical CFD methods in the industry often goes hand-in-hand with the development of computational capabilities.

8

Recommendations for future work

Accurate blade metal temperature and heat transfer predictions can allow to better predict blade lifetime. Eventually, that leads to a better and more economical design. Due to their availability and lower cost, RANS tools are still of high interest in the industry, therefore, it is important to develop them. Meanwhile, it is of essence to predict the heat transfer coefficient as accurately as possible. Hence, a trade-off between the desired fidelity of solution and computational cost should always be performed before deciding on which approach to take in the scale of 2D boundary layer codes to DNS.

Conjugate heat transfer analysis is an approach that has gained interest in research. Such a model can allow the integration of both convection and conduction within the vane to predict the temperature distribution during the design process. Furthermore, such model would remove the uncertainty of specifying a temperature boundary condition on a vane. Alternatively, a logical continuation of the current study would be to aim at implementing the scale resolving hybrid model for a full-scale film cooled vane and evaluate if the computational resource requirements are feasible.

It is often observed that different RANS turbulence models perform with varied success at various locations on the vane surface. For example, the lag EB model provided accurate HTC results on the suction side but not at the leading edge. Hence, a proposal is to investigate the possibility of performing a simulation with an application of different turbulence models or different model coefficients at various regions of the computational domain. However, currently such an application is not supported by the $Star - CCM+$ software package.

The current study can be extended by implementing a joint combustor - NGV model. The heat transfer values are susceptible to inlet conditions and turbulence characteristics, as it was shown. Inflow condition calculated with scale resolving simulation is beneficial as compared to RANS input at the NGV inlet. However, the unsteady effects of the combustor can be fully predicted only by implementing a domain combining both the combustor and the vane [6]. Furthermore, defining freestream turbulence characteristics proved to be a challenge for the scale resolving simulations. It is recommended to couple the NGV model with a model of swirl generator that would directly guide the generated swirling flow towards the vane. In addition, such a model would allow quantifying the swirl strength in terms of the non-simplified swirl number that is based on a swirler geometry.

In terms of RANS model development, the lag EB model has recently been formulated also in the $k - \omega$ framework by Biswas & Durbin [67], and it could be of interest to test this model on turbine NGV heat transfer. Furthermore, the main deficiency of the lag EB model was transition prediction in low turbulence intensity cases, suggesting that it could be of interest to investigate the potential of coupling it with a transition model.

References

[1] H. Moustapha et al. *Axial and Radial Turbines. Concepts*. Vol. 2. NREC White River Junction, VT, 2003, pp. 41–53.

[2] G. Schmid et al. “The Impact of Realistic Inlet Swirl in a 1 ½ Stage Axial Turbine”. In: vol. 2C: Turbomachinery. Turbo Expo: Power for Land, Sea, and Air. June 2014. DOI: 10.1115/GT2014-26716.

[3] J. Slotnick et al. *CFD Vision 2030 Study: A Path to Revolutionary Computational Aerosciences*. National Aeronautics and Space Administration,Washington, DC, Report No.NASA/CR–2014-218178. 2014.

[4] Danesh K. Tafti, Long He, and K. Nagendra. “Large eddy simulation for predicting turbulent heat transfer in gas turbines”. In: *Philosophical Transactions of the Royal Society A: Mathematical, Physical and Engineering Sciences* 372.2022 (2014). DOI: 10.1098/rsta.2013.0322.

[5] S. Ravelli, L. Casarsa, and G. Barigozzi. “Numerical evaluation of showerhead film cooling aerothermal performance on a first-stage vane”. In: *International Journal of Thermal Sciences* 141 (July 2019), pp. 171–186. DOI: 10.1016/j.ijthermalsci.2019.03.038.

[6] S. Cubeda et al. “Impact of Predicted Combustor Outlet Conditions on the Aerothermal Performance of Film-Cooled HPT Vanes”. In: vol. 5C: Heat Transfer. Turbo Expo: Power for Land, Sea, and Air. June 2018. DOI: 10.1115/GT2018-75921.

[7] Zhuang Wu et al. “Showerhead film cooling injection orientation design on the turbine vane leading edge considering representative lean burn combustor outflow”. In: *Proceedings of the Institution of Mechanical Engineers, Part G: Journal of Aerospace Engineering* 235.15 (2021), pp. 2342–2356. DOI: 10.1177/0954410021996566.

[8] P.W. Giel et al. “Blade Heat Transfer Measurements and Predictions in a Transonic Turbine Cascade”. In: *Turbo Expo: Power for Land, Sea, and Air*. Vol. 3. ASME paper 99-GT-125. June 1999. DOI: 10.1115/99-GT-125.

[9] F. Fontaneto. “Aero-Thermal Performance of a Film-Cooled High Pressure Turbine Blade/Vane: a Test Case for Numerical Codes Validation”. PhD thesis. University of Bergamo, 2014.

[10] B. Lakshminarayana. *Turbine Cooling and Heat Transfer*. John Wiley Sons, Ltd, 1995, pp. 597–721.

[11] L.S. Langston. “Secondary Flows in Axial Turbines—A Review”. In: *Annals of the New York Academy of Sciences* 934.1 (2001), pp. 11–26. DOI: 10.1111/j.1749-6632.2001.tb05839.x.

[12] J. Luo, E.H. Razinsky, and H. Koo Moon. “Three-Dimensional RANS Prediction of Gas-Side Heat Transfer Coefficients on Turbine Blade and Endwall”. In: *Journal of Turbomachinery* 135 (Nov. 2012). DOI: 10.1115/1.4006642.

[13] H.P. Wang et al. “Flow visualization in a linear turbine cascade of high performance turbine blades”. In: *J. Turbomach.* 119.1 (1997), pp. 1–8.

[14] F. Papa, U. Madanan, and R. J. Goldstein. “Modeling and measurements of heat/mass transfer in a linear turbine cascade”. In: *Journal of Turbomachinery* 139 (Sept. 2017). DOI: 10.1115/1.4036106.

[15] J. Cui, V. Nagabhushana Rao, and P. G. Tucker. “Numerical investigation of secondary flows in a high-lift low pressure turbine”. In: *International Journal of Heat and Fluid Flow* 63 (Feb. 2017), pp. 149–157. DOI: 10.1016/j.ijheatfluidflow.2016.05.018.

[16] R. J. Goldstein and R. A. Spores. “Turbulent Transport on the Endwall in the Region Between Adjacent Turbine Blades”. In: *Journal of Heat Transfer* 110.4a (Nov. 1988), pp. 862–869. DOI: 10.1115/1.3250586.

[17] A. Andreini et al. “Hybrid RANS-LES Modeling of the Aero-Thermal Field in an Annular Hot Streak Generator for the Study of Combustor-Turbine Interaction”. In: vol. 5B: Heat Transfer. Turbo Expo: Power for Land, Sea, and Air. June 2016. DOI: 10.1115/GT2016-56583.

[18] Z. Mansouri and R. Belamadi. “The influence of inlet swirl intensity and hot-streak on aerodynamics and thermal characteristics of a high pressure turbine vane”. In: *Chinese Journal of Aeronautics* 34.11 (2021), pp. 66–78. DOI: 10.1016/j.cja.2020.12.036.

[19] L. Giller and H. Schiffer. “Interactions Between the Combustor Swirl and the High Pressure Stator of a Turbine”. In: vol. 8: Turbomachinery, Parts A, B, and C. Turbo Expo: Power for Land, Sea, and Air. June 2012, pp. 1401–1415. DOI: 10.1115/GT2012-69157.

[20] J. D. Denton. “Loss Mechanisms in Turbomachines”. In: Turbo Expo: Power for Land, Sea, and Air. May 1993. DOI: 10.1115/93-GT-435.

[21] A. Shapiro. *The Dynamics and Thermodynamics of Compressible Fluid Flow*. McGraw-Hill, 1953.

[22] N. V. Nirmalan and L. D. Hylton. “An Experimental Study of Turbine Vane Heat Transfer With Leading Edge and Downstream Film Cooling”. In: *Journal of Turbomachinery* 112.3 (July 1990), pp. 477–487. DOI: 10.1115/1.2927683.

[23] F. G. Rubensdörffer. “Numerical and Experimental Investigations of Design Parameters Defining Gas Turbine Nozzle Guide Vane Endwall Heat Transfer”. PhD thesis. KTH Royal Institute of Technology, Stockholm, 2006.

[24] K. Zhang, Z. Li, and J. Li. “Turbine endwall cooling and heat transfer characteristics under slash-face leakage interacted with nearby discrete-hole injections”. In: *International Journal of Thermal Sciences* 170 (Dec. 2021). DOI: 10.1016/j.ijthermalsci.2021.107167.

[25] Zhi Tao et al. “Effects of non-axisymmetric endwall contouring on aerothermal performance of a gas turbine blade endwall with a purge flow”. In: *International Journal of Thermal Sciences* 164 (2021). DOI: https://doi.org/10.1016/j.ijthermalsci.2021.106921.

[26] C. H. Sieverding. “Recent Progress in the Understanding of Basic Aspects of Secondary Flows in Turbine Blade Passages”. In: *Journal of Engineering for Gas Turbines and Power* 107.2 (Apr. 1985), pp. 248–257. DOI: 10.1115/1.3239704.

[27] M. Thomas et al. “Experimental and CFD studies of NGV endwall cooling”. In: vol. 3. 2013. DOI: 10.1115/GT2013-95639.

[28] X.Yang et al. “Film Cooling Patterns over an Aircraft Engine Turbine Endwall with Slot Leakage and Discrete Hole Injection”. In: *International Journal of Heat and Mass Transfer* 165 (Feb. 2021). DOI: 10.1016/j.ijheatmasstransfer.2020.120565.

[29] R. J. Simoneau and F. F. Simon. “Progress towards understanding and predicting heat transfer in the turbine gas path”. In: *International Journal of Heat and Fluid Flow* 14.2 (1993), pp. 106–128.

[30] M. E. Crawford and W. M. Kays. *A Program for Numerical Computation of Two-Dimensional Internal and External Boundary Layer Flows*. NASA CR-2742. 1976.

[31] M. E. Crawford. *TEXSTAN. Overview [Online]*. Updated Sept 2010; cited 2021 Sept 16. URL: http://www.texstan.com/index.php.

[32] J. D. Denton. “Some Limitations of Turbomachinery CFD”. In: *Turbo Expo: Power for Land, Sea, and Air*. Vol. 7: Turbomachinery, Parts A, B, and C. June 2010, pp. 735–745. DOI: 10.1115/GT2010-22540.

[33] H. M. Phan, P. H. Duan, and C. T. Dinh. “Numerical aero-thermal study of high-pressure turbine nozzle guide vane: Effects of inflow conditions”. In: *Physics of Fluids* 32 (Mar. 2020). DOI: 10.1063/1.5144418.

[34] J. Tyacke et al. “Turbomachinery simulation challenges and the future”. In: *Progress in Aerospace Sciences* 110 (Oct. 2019). DOI: 10.1016/j.paerosci.2019.100554.

[35] W. Seok, S. B. Lee, and S. H. Rhee. “An improved partially-averaged Navier-Stokes model for secondary flows”. In: *International Journal of Heat and Mass Transfer* 180 (Dec. 2021). DOI: 10.1016/j.ijheatmasstransfer.2021.121780.

[36] F. Menter. “Stress-Blended Eddy Simulation (SBES) — A New Paradigm in Hybrid RANS-LES Modeling”. In: *Progress in Hybrid RANS-LES Modelling*. Springer International Publishing, 2018, pp. 27–37.

[37] J.L. Wu, H. Xiao, and E. Paterson. “Physics-informed machine learning approach for augmenting turbulence models: A comprehensive framework”. In: *Physical Review Fluids* 7 (July 2018). DOI: 10.1103/PhysRevFluids.3.074602.

[38] A. Rezaeiha, H. Montazeri, and B. Blocken. “CFD analysis of dynamic stall on vertical axis wind turbines using Scale-Adaptive Simulation (SAS): Comparison against URANS and hybrid RANS/LES”. In: *Energy Conversion and Management* 196 (2019), pp. 1282–1298. DOI: doi.org/10.1016/j.enconman.2019.06.081.

[39] S.S. Girimaji. “Partially-Averaged Navier-Stokes Model for Turbulence: A Reynolds-Averaged Navier-Stokes to Direct Numerical Simulation Bridging Method”. In: *Journal of Applied Mechanics* 73.3 (Nov. 2005), pp. 413–421. DOI: 10.1115/1.2151207.

[40] Bin Ji et al. “Partially-Averaged Navier–Stokes method with modified k–ε model for cavitating flow around a marine propeller in a non-uniform wake”. In: *International Journal of Heat and Mass Transfer* 55.23 (2012), pp. 6582–6588. DOI: 10.1016/j.ijheatmasstransfer.2012.06.065.

[41] Yaping Ju, Yi Feng, and Chuhua Zhang. “Conjugate Heat Transfer Simulation and Entropy Generation Analysis of Gas Turbine Blades”. In: *Journal of Engineering for Gas Turbines and Power* 143 (Aug. 2021). DOI: 10.1115/1.4049989.

[42] M. Lorini et al. “Discontinuous Galerkin solution of the RANS and k_L-k-$log(\omega)$ equations for natural and bypass transition”. In: *Computers and Fluids* 214 (Jan. 2021). DOI: 10.1016/j.compfluid.2020.104767.

[43] R. E. Mayle. “The Role of Laminar-Turbulent Transition in Gas Turbine Engines”. In: *Turbo Expo: Power for Land, Sea, and Air*. Vol. 5. June 1991. DOI: 10.1115/91-GT-261.

[44] R. Pecnik, P. Pieringer, and W. Sanz. “Numerical Investigation of The Secondary Flow of a Transonic Turbine Stage Using Various Turbulence Closures”. In: *Power for Land*. 2005.

[45] V.K. Garg and A.A. Ameri. “Two-equation turbulence models for prediction of heat transfer on a transonic turbine blade”. In: *Int. Journal of Heat and Fluid Flow* 22 (2001), pp. 593–602.

[46] M. Morini et al. “Numerical analysis of the effects of nonuniform surface roughness on compressor stage performance”. In: *Journal of Engineering for Gas Turbines and Power* 133 (2011). DOI: 10.1115/1.4002350.

[47] H.K. Versteeg and W. Malalasekera. *An Introduction to Computational Fluid Dynamics. The Finite Volume Method*. 4th international ed. Pearson Education, 2007, pp. 66–97.

[48] F. Menter. “Influence of freestream values on $k-\omega$ turbulence model predictions”. In: *AIAA Journal* 30 (2012). DOI: 10.2514/3.11115.

[49] M. Kato and B. E. Launder. “The Modeling of Turbulent Flow Around Stationary and Vibrating Square Cylinders”. In: *9th Symposium on Turbulent Shear Flows*. Aug. 1993.

[50] F. Menter. “Two-Equation Eddy-Viscosity Turbulence Models for Engineering Applications”. In: *AIAA Journal* 32.8 (1994), pp. 1598–1605.

[51] Chang Hwan Park and Seung O. Park. “On the limiters of two-equation turbulence models”. In: *International Journal of Computational Fluid Dynamics*. Vol. 19. Jan. 2005, pp. 79–86. DOI: 10.1080/10618560412331286292.

[52] P. A. Durbin. “On the stagnation point anomaly”. In: *Int. J. Heat Fluid Flow* 17.1 (1996), pp. 89–90.

[53] P. A. Durbin. “Some Recent Developments in Turbulence Closure Modeling”. In: *Annual Review of Fluid Mechanics* 50 (2018), pp. 77–103.

[54] V. Yakhot et al. “Development of turbulence models for shear flows by a double expansion technique”. In: *Physics of Fluids A* 4 (1992), pp. 1510–1520. DOI: 10.1063/1.858424.

[55] Zhigang Li et al. “Effects of Freestream Turbulence Intensity, Turbulence Length Scale, and Exit Reynolds Number on Vane Endwall Secondary Flow and Heat Transfer in a Transonic Turbine Cascade”. In: *Turbo Expo: Power for Land, Sea, and Air*. Vol. 7C: Heat Transfer. Sept. 2020. DOI: 10.1115/GT2020-14639.

[56] K. Hermanson et al. “Predictions of external heat transfer for turbine vanes and blades with secondary flowfields”. In: *Journal of Turbomachinery* 125 (Jan. 2003), pp. 107–113. DOI: 10.1115/1.1529201.

[57] A.A. Ameri and K. Ajmani. “Evaluation of Predicted Heat Transfer on a Transonic Blade Using $v^2 - f$ Models”. In: *Turbo Expo: Power for Land, Sea, and Air*. Vol. 3: Turbo Expo 2004. June 2004, pp. 547–554. DOI: 10.1115/GT2004-53572.

[58] D. Enico. “External Heat Transfer Coefficient Predictions on a Transonic Turbine Nozzle Guide Vane Using Computational Fluid Dynamics”. MA thesis. Linköping University, 2021.

[59] D.R. Laurence, J.C. Uribe, and S.V. Utyuzhnikov. “A Robust Formulation of the v2-f Model”. In: *Flow, Turbulence and Combustion* 73 (2004), pp. 169–185.

[60] Siemens STAR-CCM+ Documentation. *Version 13.06*. 2020, pp. 6989–7081.

[61] W. Rodi. “Experience with Two-Layer Models Combining the $k - \epsilon$ Model with a One-Equation Model Near the Wall”. In: *29th Aerospace Sciences Meeting*. American Physical Society, Jan. 2018. DOI: 10.1103/PhysRevFluids.3.074602.

[62] A. Andreini et al. “Flowfield and Heat Transfer Numerical Analysis of a Stator Vane Endwall With High Freestream Turbulence”. In: *Turbo Expo: Power for Land, Sea, and Air*. Vol. 5B: Heat Transfer. June 2015. DOI: 10.1115/GT2015-42489.

[63] R. Manceau and K. Hanjalic. “Elliptic blending model: A new near-wall Reynolds-stress turbulence closure”. In: *Physics of Fluids* 14 (2002), pp. 744–754.

[64] S. Lardeau and F. Billard. “Development of an elliptic-blending lag model for industrial applications”. In: *54th AIAA Aerospace Sciences Meeting*. American Institute of Aeronautics and Astronautics Inc, AIAA, 2016. DOI: 10.2514/6.2016-1600.

[65] L. Xu, E. Baglietto, and S. Brizzolara. “Extending the applicability of RANS turbulence closures to the simulation of transitional flow around hydrofoils at low Reynolds number”. In: *Ocean Engineering* 164 (Sept. 2018), pp. 1–12. DOI: 10.1016/j.oceaneng.2018.06.031.

[66] R. Biswas and P.A. Durbin. “Assessment of viscosity models that incorporate lag parameter scaling”. In: *International Journal of Heat and Fluid Flow* 78 (Aug. 2019). DOI: 10.1016/j.ijheatfluidflow.2019.108427.

[67] R. Biswas, P. A. Durbin, and G. Medic. “Development of an elliptic blending lag $k - \omega$ model”. In: *International Journal of Heat and Fluid Flow* 76 (2019), pp. 26–39. DOI: 10.1016/j.ijheatfluidflow.2019.01.011.

[68] H. Xiao and P. Cinnella. “Quantification of model uncertainty in RANS simulations: A review”. In: *Progress in Aerospace Sciences* 108 (2019), pp. 1–31. DOI: https://doi.org/10.1016/j.paerosci.2018.10.001.

[69] E. Casartelli et al. “Application of Advanced RANS Turbulence Models for the Prediction of Turbomachinery Flows”. In: *Journal of Turbomachinery* 144.1 (Sept. 2021). DOI: 10.1115/1.4051938.

[70] S. Wallin and A. V. Johansson. “An Explicit Algebraic Reynolds Stress Model for Incompressible and Compressible Turbulent Flows”. In: *J. Fluid Mechanics* 403 (2000), pp. 89–132.

[71] P.R. Spalart. “Strategies for turbulence modelling and simulations”. In: *Int. J. of Heat and Fluid* 21.3 (2000), pp. 252–263.

[72] T. E. Dyson, D. G. Bogard, and S. D. Bradshaw. “Evaluation of CFD simulations of film cooling performance on a turbine vane including conjugate heat transfer effects”. In: *International Journal of Heat and Fluid Flow* 50 (2014), pp. 279–286. DOI: 10.1016/j.ijheatfluidflow.2014.08.010.

[73] Hong Wu et al. “Showerhead Film Cooling Performance of a Transonic Turbine Vane at High Freestream Turbulence (Tu = 16%): 3-D CFD and Comparison With Experiment”. In: vol. 10: Heat Transfer, Fluid Flows, and Thermal Systems, Parts A, B, and C. ASME International Mechanical Engineering Congress and Exposition. Oct. 2008, pp. 1151–1161. DOI: 10.1115/IMECE2008-67782.

[74] Xueying Li, Jing Ren, and Hongde Jiang. “Film Cooling Modeling of Turbine Blades Using Algebraic Anisotropic Turbulence Models”. In: *Journal of Turbomachinery* 136.11 (Aug. 2014). DOI: 10.1115/1.4028174.

[75] M. Silieti, A.J. Kassab, and D. Eduardo. “Film Cooling Effectiveness From a Single Scaled-Up Fan-Shaped Hole: A CFD Simulation of Adiabatic and Conjugate Heat Transfer Models”. In: vol. 3: Turbo Expo 2005, Parts A and B. Turbo Expo: Power for Land, Sea, and Air. June 2005, pp. 431–441. DOI: 10.1115/GT2005-68431.

[76] Y. C. Zhao et al. “Film cooling of showerhead holes from the twisted leading edge of a gas turbine blade: Complex mainstream characteristics and reasonable angle arrangement”. In: *Aerospace Science and Technology* 119 (Dec. 2021). DOI: 10.1016/j.ast.2021.107208.

[77] F. R. Menter et al. “A correlation-based transition model using local variables - Part I: Model formulation”. In: *Journal of Turbomachinery* 128 (2006), pp. 413–422. DOI: 10.1115/1.2184352.

[78] T. Bacci et al. “Experimental and CFD analyses of a highly-loaded gas turbine blade”. In: *Energy Procedia*. Vol. 126. Elsevier Ltd, Sept. 2017, pp. 770–777. DOI: 10.1016/j.egypro.2017.08.253.

[79] E. Dick and S. Kubacki. “Transition models for turbomachinery boundary layer flows: A review”. In: *International Journal of Turbomachinery, Propulsion and Power* 2 (Apr. 2017). DOI: 10.3390/ijtpp2020004.

[80] I. Jonsson et al. “Experimental and Numerical Study of Laminar-Turbulent Transition on a Low-Pressure Turbine Outlet Guide Vane”. In: *Journal of Turbomachinery* 143 (Oct. 2021). DOI: 10.1115/1.4050629.

[81] A. Smirnovsky and E. M. Smirnov. “Turbine Vane Cascade Heat Transfer Predictions Using a Modified Version of the $\gamma - Re_\theta$ Laminar-Turbulent Transition Model”. In: *Int. Symp. on Heat Transfer in Gas Turbine Systems*. Aug. 2009, pp. 1–11. DOI: 10.1615/ichmt.2009.heattransfgasturbsyst.370.

[82] C. Bode et al. “Application of cross flow transition criteria to local correlation-based transition model”. In: *52nd AIAA/SAE/ASEE Joint Propulsion Conference, 2016*. American Institute of Aeronautics and Astronautics Inc, AIAA, 2016. DOI: 10.2514/6.2016-5054.

[83] C. Müller and F. Herbst. “Modelling of Crossflow-Induced Transition Based on Local Variables”. In: *6th European Conference on Computational Fluid Dynamics (ECFD)*. 2014.

[84] C. Bode et al. “Improved turbulence prediction in turbomachinery flows and the effect on three-dimensional boundary layer transition”. In: *International Journal of Turbomachinery, Propulsion and Power* 3 (July 2018). DOI: 10.3390/ijtpp3030018.

[85] K. Suluksna, P. Dechaumphai, and E. Juntasaro. “Correlations for Modeling Transitional Boundary Layers Under Influences of Freestream Turbulence and Pressure Gradient”. In: *International Journal of Heat and Fluid Flow* 30 (Feb. 2009), pp. 66–75. DOI: 10.1016/j.ijheatfluidflow.2008.09.004.

[86] Menter F. R. et al. “A One-Equation Local Correlation-Based Transition Model”. In: *Flow, Turbulence and Combustion* (July 2015). DOI: 0.1007/s10494-015-9622-4.

[87] D. K. Walters and D. Cokljat. “A Three-Equation Eddy-Viscosity Model for Reynolds-Averaged Navier-Stokes Simulations of Transitional Flow”. In: *Journal of Fluids Engineering, Transactions of the ASME* 130 (12 Dec. 2008). DOI: 10.1115/1.2979230.

[88] R. E. Mayle and A. Schulz. “The Path to Predicting Bypass Transition”. In: *Turbo Expo: Power for Land, Sea, and Air*. Vol. 1: Turbomachinery. June 1996. DOI: 10.1115/96-GT-199.

[89] H. Medina et al. “A novel laminar kinetic energy model for the prediction of pretransitional velocity fluctuations and boundary layer transition”. In: *International Journal of Heat and Fluid Flow* 69 (Feb. 2018), pp. 150–163. DOI: 10.1016/j.ijheatfluidflow.2017.12.008.

[90] D. Lengani et al. “Analysis and modelling of the relation between the shear rate and Reynolds stress tensors in transitional boundary layers”. In: *International Journal of Heat and Fluid Flow* 84 (Aug. 2020). DOI: 10.1016/j.ijheatfluidflow.2020.108615.

[91] F. Bassi et al. “Discontinuous Galerkin solution of the Reynolds-averaged Navier–Stokes and k–ω turbulence model equations”. In: *Computers & Fluids* 34 (2005), pp. 507–540.

[92] E. Salimipour. “A modification of the $k - k_L - \omega$ turbulence model for simulation of short and long separation bubbles”. In: *Computers and Fluids* 181 (Mar. 2019), pp. 67–76. DOI: 10.1016/j.compfluid.2019.01.003.

[93] S.M. Aftab et al. “Turbulence Model Selection for Low Reynolds Number Flows”. In: *PLoS One* 11.4 (Apr. 2016). DOI: 10.1371/journal.pone.0153755.

[94] F. Bassi et al. “Turbine vane film cooling: Heat transfer evaluation using high-order discontinuous Galerkin RANS computations”. In: *International Journal of Heat and Fluid Flow* 61 (Oct. 2016), pp. 610–625. DOI: 10.1016/j.ijheatfluidflow.2016.07.007.

[95] Y. Liu, P. Li, and K. Jiang. “Comparative assessment of transitional turbulence models for airfoil aerodynamics in the low Reynolds number range”. In: *Journal of Wind Engineering and Industrial Aerodynamics* 217 (Oct. 2021). DOI: 10.1016/j.jweia.2021.104726.

[96] M. Marconcini, R. Pacciani, and A. Arnone. “Transition modelling implications in the CFD analysis of a turbine nozzle vane cascade tested over a range of Mach and Reynolds numbers”. In: *Journal of Thermal Science* 24 (Nov. 2015), pp. 526–534. DOI: 10.1007/s11630-015-0818-7.

[97] R. Pacciani et al. “An Assessment of the Laminar Kinetic Energy Concept for the Prediction of High-Lift, Low-Reynolds Number Cascade Flows”. In: *J. Power and Energy* 225.7 (2011), pp. 995–1003.

[98] ANSYS. *Fluent Theory Guide, Release 18.0*. January 2018.

[99] E. M. Greitzer, C. S. Tan, and M. B. Graf. *Internal Flow: Concepts and Applications*. Cambridge Engine Technology Series. Cambridge University Press, 2004. DOI: 10.1017/CBO9780511616709.

[100] F. Cheng et al. “Turbine vane endwall partition film cooling based on the passage vortex core line”. In: *International Journal of Heat and Mass Transfer* 162 (Dec. 2020). DOI: 10.1016/j.ijheatmasstransfer.2020.120354.

[101] A. Sveningsson. *Transition Modelling– A Review*. Department of Thermo and Fluid Dynamics, Chalmers University of Technology. 2006.

[102] C. Wang et al. “Experimental and numerical investigation of outlet guide vane and endwall heat transfer with various inlet flow angles”. In: *International Journal of Heat and Mass Transfer* 95 (Apr. 2016), pp. 355–367. DOI: 10.1016/j.ijheatmasstransfer.2015.11.029.

[103] A.M. Levchenya, E.M. Smirnov, and V.D. Goryachev. “RANS-based numerical simulation and visualization of the horseshoe vortex system in the leading edge endwall region of a symmetric body”. In: *International Journal of Heat and Fluid Flow* 31.6 (2010), pp. 1107–1112. DOI: 10.1016/j.ijheatfluidflow.2010.06.014.

[104] T. J. Praisner and C. R. Smith. “The Dynamics of the Horseshoe Vortex and Associated Endwall Heat Transfer—Part I: Temporal Behavior”. In: *Journal of Turbomachinery* 128.4 (Feb. 2005), pp. 747–754. DOI: 10.1115/1.2185676.

[105] T. J. Praisner and C. R. Smith. “The Dynamics of the Horseshoe Vortex and Associated Endwall Heat Transfer: Part 2 — Time-Mean Results”. In: vol. 3: Turbo Expo 2005, Parts A and B. Turbo Expo: Power for Land, Sea, and Air. June 2005, pp. 909–917. DOI: 10.1115/GT2005-69091.

[106] G. Medic et al. “Prediction of heat transfer in a turbine cascade with high levels of free-stream turbulence”. In: *Center for Turbulence Research. Proceedings of the Summer Program 2012*. 2012.

[107] S. Dutta, Je-Chin Han, and S.V. Ekkad. *Gas Turbine Heat Transfer and Cooling Technology*. Taylor & Francis, 2000, pp. 179–228.

[108] J. Steelant and E. Dick. “Prediction of by-pass transition by means of a turbulence weighting factor - Part I: Theory and Validation.” In: ASME International Gas Turbine Congress, Indianapolis, 1999, paper 99-GT-29. 1999.

[109] J. Luo and E.H Razinsky. “Prediction of Heat Transfer and Flow Transition on Transonic Turbine Airfoils Under High Freestream Turbulence”. In: *Turbo Expo: Power for Land, Sea, and Air*. June 2008.

[110] R. Pecnik et al. “Transition Modeling Using Two Different Intermittency Transport Equations”. In: *Flow, Turbulence and Combustion* 70 (2003), pp. 299–323. DOI: 10.1023/B:APPL.0000004983.49982.69.

[111] Y.A. Cengel and A.J. Ghajar. *Heat and Mass Transfer: Fundamentals and Applications Fifth Edition in SI Units*. McGraw-Hill Education, 2015, pp. 377–441.

[112] M.H. Brunner. “In-Situ Measurement of Blade Heat Transfer Coefficients and Gas Recovery Temperature”. PhD thesis. ETH Zurich, 2007.

[113] T. Arts and M. Lambert de Rouvroit. “Aero-Thermal Performance of a Two-Dimensional Highly Loaded Transonic Turbine Nozzle Guide Vane: A Test Case for Inviscid and Viscous Flow Computations”. In: *Journal of Turbomachinery* 114.1 (Jan. 1992), pp. 147–154. DOI: 10.1115/1.2927978.

[114] R. Maffulli and L. He. “Dependence of External Heat Transfer Coefficient and Aerodynamics on Wall Temperature for 3-D Turbine Blade Passage”. In: vol. 2C: Turbomachinery. Turbo Expo: Power for Land, Sea, and Air. June 2014. DOI: 10.1115/GT2014-26763.

[115] R. Maffulli and L. He. “Wall Temperature Effects on Heat Transfer Coefficient”. In: vol. 3C: Heat Transfer. Turbo Expo: Power for Land, Sea, and Air. June 2013. DOI: 10.1115/GT2013-94291.

[116] K.L. Harrison and D.G. Bogard. “Use of the Adiabatic Wall Temperature in Film Cooling to Predict Wall Heat Flux and Temperature”. In: vol. 4: Heat Transfer, Parts A and B. Turbo Expo: Power for Land, Sea, and Air. June 2008, pp. 1197–1207. DOI: 10.1115/GT2008-51424.

[117] W. M. Kays. “Turbulent Prandtl Number—Where Are We?” In: *Journal of Heat Transfer* 116.2 (May 1994), pp. 284–295. DOI: 10.1115/1.2911398.

[118] E.L. Houghton et al. “Chapter 3 - Viscous Flow and Boundary Layers”. In: *Aerodynamics for Engineering Students*. Seventh Edition. Butterworth-Heinemann, 2017, pp. 151–254. DOI: 10.1016/B978-0-08-100194-3.00003-1.

[119] R. Narasimha. “The dynamics of the transition zone and its modeling”. In: *VKI, Boundary Layers in Turbomachines*. 1991.

[120] D. G. Bogard and K. A. Thole. “Gas Turbine Film Cooling”. In: *Journal of Propulsion and Power* 22.2 (2006), pp. 249–270. DOI: 10.2514/1.18034.

[121] A.F. Chen, S.J. Li, and J.C. Han. “Film cooling for cylindrical and fan-shaped holes using pressure-sensitive paint measurement technique”. In: *Journal of Thermophysics and Heat Transfer* 29 (2015), pp. 775–784. DOI: 10.2514/1.T4518.

[122] H. Abdeh et al. “A Parametric Investigation of Vane Showerhead Film Cooling by Pressure-Sensitive Paint Technique”. In: *Journal of Turbomachinery* 142.3 (Feb. 2020). DOI: 10.1115/1.4045875.

[123] R. J. Goldstein and J. R. Taylor. “Mass Transfer in the Neighborhood of Jets Entering a Crossflow”. In: *Journal of Heat Transfer* 104.4 (Nov. 1982), pp. 715–721. DOI: 10.1115/1.3245190.

[124] R. J. Goldstein and P. Jin. “Film Cooling Downstream of a Row of Discrete Holes With Compound Angle”. In: vol. 3: Heat Transfer; Electric Power; Industrial and Cogeneration. Turbo Expo: Power for Land, Sea, and Air. May 2000. DOI: 10.1115/2000-GT-0248.

[125] S. Hickel. *Lecture slides in CFD for Aerospace Engineers*. Delft University of Technology. 2021.

[126] A.M. Levchenya and E.M. Smirnov. “Numerical Analysis of the Multiple-Horseshoe-Vortex Effects on the Endwall Heat Transfer in the Leading-Edge Region of a Symmetric Bluff Body”. In: vol. 5. Jan. 2010. DOI: 10.1115/IHTC14-22655.

[127] R. Langtry. “A Correlation-Based Transition Model Using Local Variables for Unstructured Parallelized CFD Codes”. PhD thesis. University of Stuttgart, 2006.

[128] N. Sorensen. “CFD modelling of laminar-turbulent transition for airfoils and rotors using the $\gamma - Re_\theta$ model”. In: *Wind Energy* 12.8 (2009), pp. 715–733. DOI: 10.1002/we.325.

[129] W. Elsner et al. “Transition Prediction on Turbine Blade Profile With Intermittency Transport Equation”. In: *Journal of Turbomachinery* 132.1 (Sept. 2009). DOI: 10.1115/1.3072716.

[130] M.E. Kelterer et al. “Computation of Laminar-Turbulent Transition in Turbomachinery Using the Correlation Based $\gamma - Re_\theta$ Transition Model”. In: *ASME Turbo Expo 2009: Power for Land, Sea and Air GT2010 June 14-18, 2010, Glasgow, Scotland, GT2010-22207*. 2010.

[131] P. W. Giel et al. “Endwall Heat Transfer Measurements in a Transonic Turbine Cascade”. In: *Journal of Turbomachinery* 120.2 (Apr. 1998), pp. 305–313. DOI: 10.1115/1.2841407.

[132] A.M. Levchenya and E.M. Smirnov. “CFD-Analysis of 3D flow structure and endwall heat transfer in a transonic turbine blade cascade: effects of grid refinement”. In: *West-East High Speed Flow Field Conference*. Nov. 2007.

[133] J. M. Cutbirth and D. G. Bogard. “Thermal Field and Flow Visualization Within the Stagnation Region of a Film-Cooled Turbine Vane”. In: *Journal of Turbomachinery* 124.2 (Apr. 2002), pp. 200–206. DOI: 10.1115/1.1451086.

[134] L. Mangani et al. “Conjugate Heat Transfer Analysis of NASA C3X Film Cooled Vane With an Object-Oriented CFD Code”. In: vol. 4: Heat Transfer, Parts A and B. Turbo Expo: Power for Land, Sea, and Air. June 2010, pp. 1805–1814. DOI: 10.1115/GT2010-23458.

[135] S. Zhang, D. G. MacManus, and J. Luo. “Parametric study of turbine NGV blade lean and vortex design”. In: *Chinese Journal of Aeronautics* 29.1 (2016), pp. 104–116. DOI: https://doi.org/10.1016/j.cja.2015.12.005.

[136] Z. Musavi et al. “Experimental and Numerical Investigation of Flow Field and Soot Particle Size Distribution of Methane-Containing Gas Mixtures in a Swirling Burner”. In: *ACS Omega* 7.1 (Dec. 2021), pp. 469–479. DOI: 10.1021/acsomega.1c04895.

[137] L.F. Wahlgren. “Evaluation of CFD Methods for Prediction of Total Temperature and Total Pressure Distribution in Gas Turbines”. MA thesis. KTH School of Industrial Engineering and Management, 2019.

A

Results of validation cases B, D, E, G

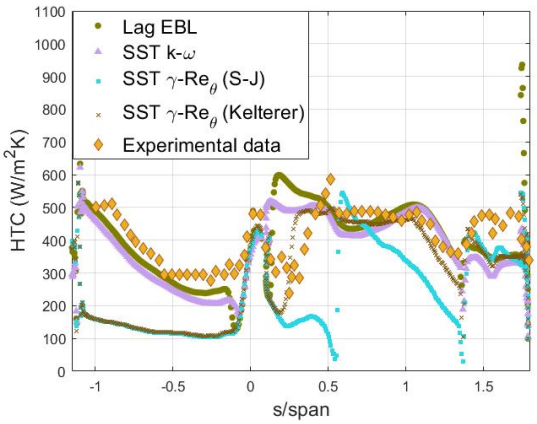

(a) Case G midspan, $Tu = 0.5\%$

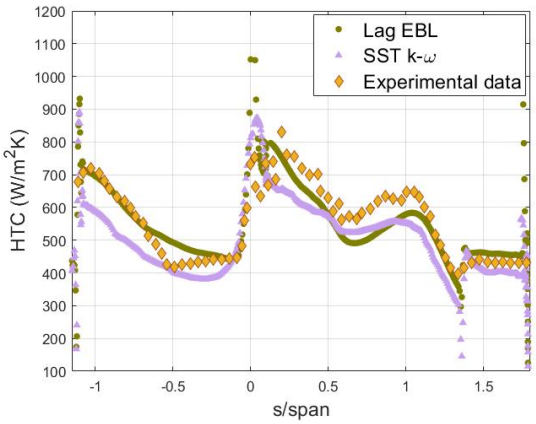

(b) Case E midspan, $Tu = 8\%$

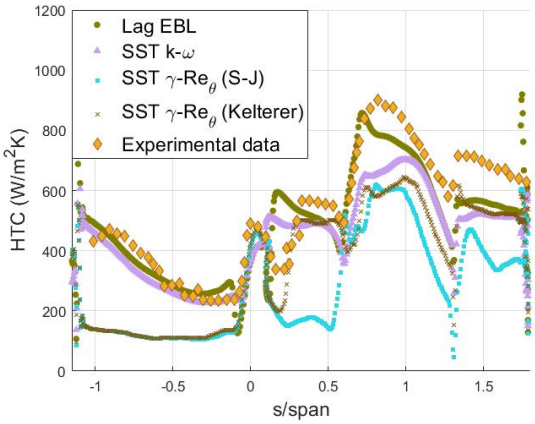

(c) Case G 10% span, $Tu = 0.5\%$

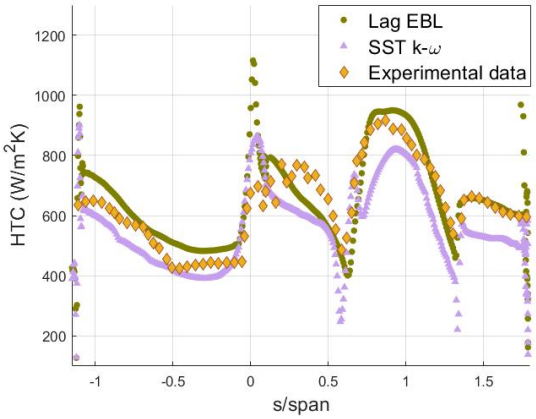

(d) Case E 10% span, $Tu = 8\%$

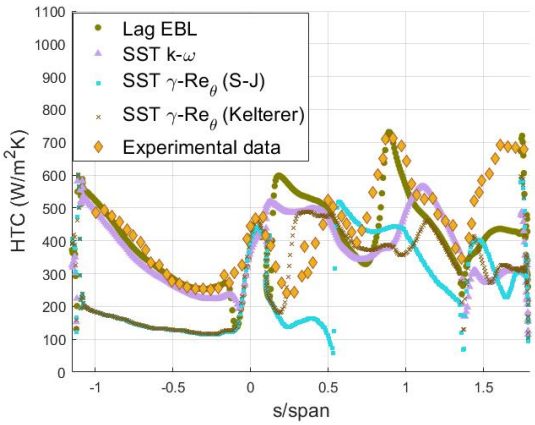

(e) Case G 25% span, $Tu = 0.5\%$

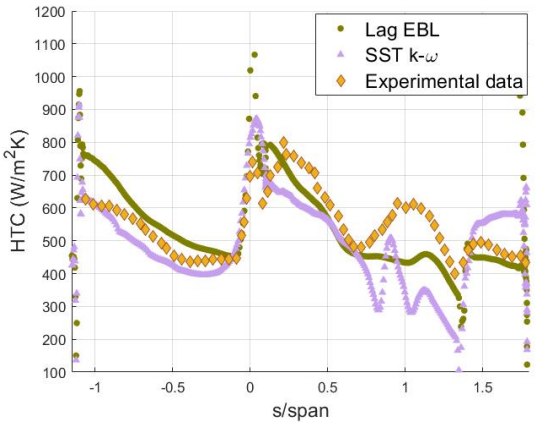

(f) Case E 25% span, $Tu = 8\%$

Figure A.1: $Re = 1.0 \cdot 10^6$, $Ma_{out} = 1.30$. HTC along the curvilinear distance on the airfoil surface at various span locations. Both, Suluksna-Juntasaro (S-J) correlation (default in *Star-CCM+*) and Kelterer et al. correlation, are implemented for $\gamma - Re_\theta$ model in the $Tu = 0.5\%$ case.

Results of the remaining four test cases from the Giel experiment are presented. The $Re = 1.0 \cdot 10^6$ cases E and G are shown in Figure A.1, and the $Re = 0.5 \cdot 10^6$ cases in Figure A.2.

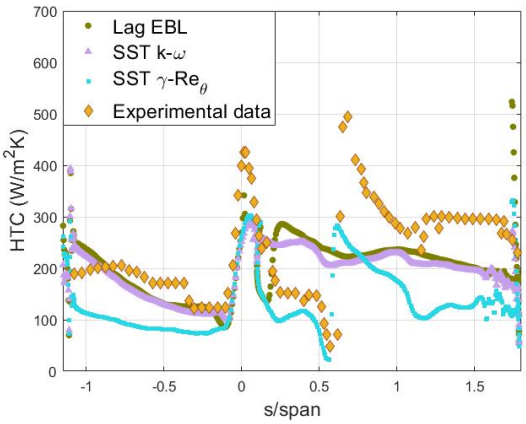

(a) Case D midspan, $Tu = 0.25\%$

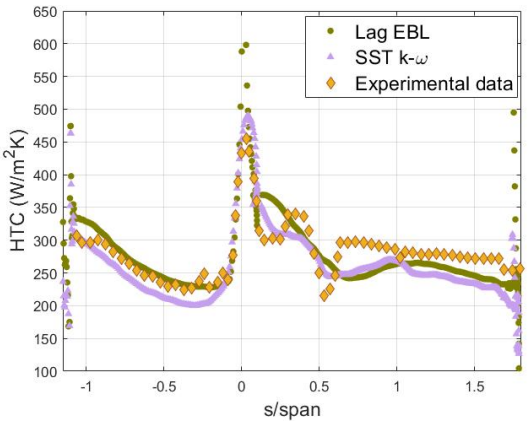

(b) Case B midspan, $Tu = 8\%$

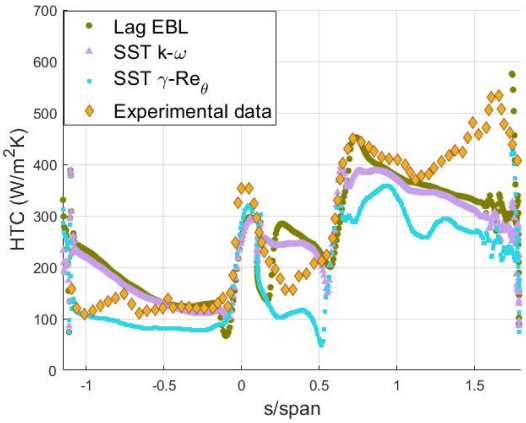

(c) Case D 10% span, $Tu = 0.25\%$

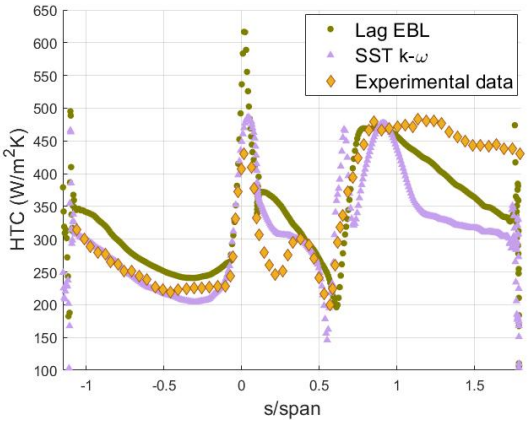

(d) Case B 10% span, $Tu = 8\%$

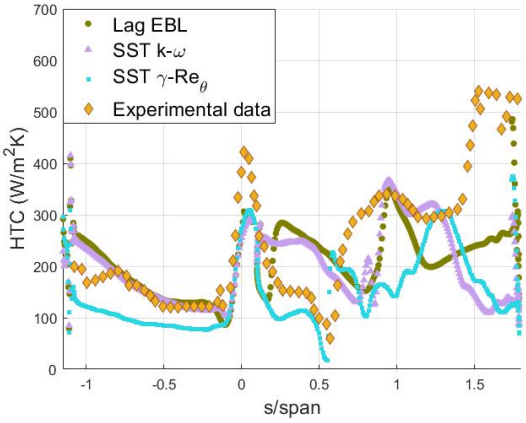

(e) Case D 25% span, $Tu = 0.25\%$

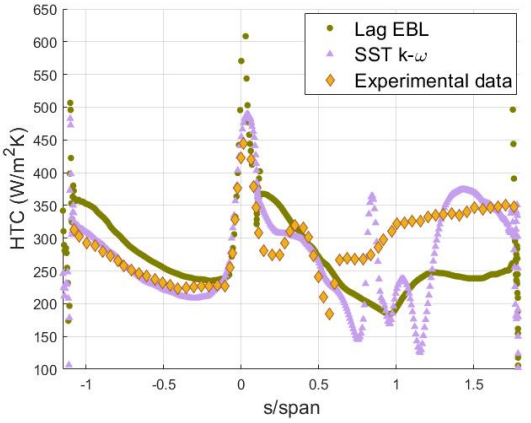

(f) Case B 25% span, $Tu = 8\%$

Figure A.2: $Re = 0.5 \cdot 10^6$, $Ma_{out} = 0.98$. HTC along the curvilinear distance on the airfoil surface at various span locations. Suluksna-Juntasaro correlation (default in *Star-CCM+*) is implemented for $\gamma - Re_\theta$ model in the $Tu = 0.25\%$ case.